THEORETICAL PREDICTIONS ON THE ELECTRICAL AND MAGNETIC PROPERTIES OF NOVEL TWO-DIMENSIONAL MATERIALS

JIANG SHUJUAN

PhD

The Hong Kong Polytechnic University

2024

The Hong Kong Polytechnic University

Department of Mechanical Engineering

Theoretical Predictions on the Electrical and Magnetic Properties of Novel Two-dimensional Materials

Jiang Shujuan

A thesis submitted in partial fulfillment of the
requirements for the degree of Doctor of Philosophy

July 2024

CERTIFICATE OF ORIGINALITY

I hereby declare that this thesis is my own work and that, to the best of my knowledge and belief, it reproduces no material previously published or written, nor material that has been accepted for the award of any other degree or diploma, except where due acknowledgement has been made in the text.

__________________________ (Signed)

JIANG Shujuan (Name of student)

Abstract

In 2004, the discovery of graphene has opened creative opportunities in two-dimensional (2D) materials science and other research fields, which developed rapidly in recent years. Compared to their bulk counterparts, 2D materials have ultrathin structure and perfect boundaries, endowing them with extraordinary mechanical, electrical, magnetic, and optical properties. In addition to the most prevalent 2D materials including graphene, hexagonal boron nitride, transition metal dichalcogenides, and black phosphorene, many other outstanding 2D materials have been studied in the past five years. However, there are some challenges, such as limited types of experimentally synthesized 2D materials, poor material stability, and low Curie temperatures of the 2D magnetic materials. First-principles calculations based on density functional theory can effectively discover and predict 2D materials, and study their electrical and magnetic properties, which are much related to their electron density and atomic structure. In this thesis work, a series of novel 2D materials with excellent electronic, mechanical, and magnetic performances are predicted. The underlying mechanisms are also explained.

1) A novel GaOCl monolayer with excellent thermal and dynamical stability at room temperature is predicted and studied systematically, and its wide direct bandgap (4.46 eV) can be further modulated under applied strains. The 2D semiconductor exhibits high mechanical flexibility, and anisotropy in Poisson's ratio and carrier mobilities, endowing it with a broad spectrum of electronic and optoelectronic applications. More

importantly, the GaOCl monolayer has spontaneous magnetization induced by hole doping and shows outstanding multidirectional piezoelectricity, which are comparable with those of either magnetic or piezoelectric 2D materials. Our calculations indicate that the GaOCl monolayer with wide bandgaps and tunable piezoelectricity and ferromagnetism could be promising for applications in multifunctional integrated nano-devices with high performance.

2) Novel 2D Janus GaOClX (X = F, Br, and I) monolayers with superior dielectric energy storage properties are predicted. They are indirect-bandgap semiconductors with bandgaps of 2.18 ~ 4.36 eV, and possess anisotropic carrier mobility, strong mechanical flexibility, as well as excellent out-of-plane piezoelectricity. More importantly, it is found that the GaOCl monolayer and Janus GaOClX monolayers could exhibit ultrahigh energy storage density (as high as 893.32 J/cm^3) compatible to those of electrochemical supercapacitors and batteries, unparallel by other dielectric materials reported to date. This work opens a new window in searching for novel dielectric materials, which could be used in dielectric capacitors with superior energy storage density and power density, excellent efficiency and thermal stability.

3) The effects of carrier doping on magnetic and electronic properties of 2D Janus TiXO (X = S, Se) systems are investigated. It is found the electronic instability of systems is related with the flat conduction-band edge and high density of states near Fermi energy. At a concentration of electron doping n ranging from ~10^{13} to ~10^{14} cm^{-2}, the system maintains in a fully spin-polarized state and the Curie temperature (T_C) is estimated to be above room temperature; while the nonmagnetic semiconductor TiXO monolayer

could become a magnetic half-metal when n is varied. The doping-induced magnetisms and T_C could be modulated substantially by applying strains and alternating the number of monolayers in Janus TiXO multilayers. The results indicate that the Janus TiXO possesses tunable magnetic properties, providing promising 2D materials for electronics and spintronics applications. Moreover, a series of novel Janus XYP_2 (X/Y = Si, Ge, Sn and Pb; $X \neq Y$) monolayers with good stability, electronic, mechanical, piezoelectric properties as well as ferromagnetic properties are predicted. They are all indirect-bandgap semiconductors with bandgaps varying from 0.56 to 2.18 eV. The monolayers exhibit in-plane and out-of-plane piezoelectricity with large piezoelectric coefficients, suggesting that they are promising piezoelectric materials for nano-electromechanical systems. In the $SiGeP_2$, $GeSnP_2$, and $SnPbP_2$ monolayers, hole doping is found to be an effective approach in inducing or tuning different ferromagnetic states resulting from the electronic instability as reflected by the van Hove singularity in the 2D systems. The results suggest that Janus XYP_2 monolayers could be promising 2D materials for applications in nano-electronic, spintronic and nano-electromechanical devices.

4) With transition- metal (TM) and rare-earth (RE) elements, $(MoWFeCoX)S_2$ (X=Gd, Sm, and Nd) high-entropy (HE) disulfide monolayers are designed and studied. Through local distortion, the 2D HE TM-RE disulfides with disordered structures can be stable at elevated temperatures. It is feasible to synthesize these disulfides at moderate temperatures similar to those of previously reported layered HE compounds. More importantly, they could be promising 2D materials with high absorption

coefficients (10^5 cm^{-1}) in a broad range of frequency domain and anisotropic mechanical properties that are used in multifunctional integrated devices.

List of publications

Journal papers

1. **Shujuan Jiang**, Huabing Yin and Guang-Ping Zheng. "GaOCl monolayer: a novel wide-bandgap 2D material with hole-doping-induced ferromagnetism and multidirectional piezoelectricity." ***Nanoscale***, 14, 11369-11377 (2022)
2. **Shujuan Jiang**, Guang-Ping Zheng. "Janus GaOClX (X = F, Br, and I) monolayers as predicted by first-principles calculations: A novel type of nano-dielectrics with superior energy storage properties. " ***Phys. Chem. Chem. Phys.***, 25, 20854-20862 (2023)
3. **Shujuan Jiang**, Siyuan Liu, Yi Wang, Weizhen Chen, Huabing Yin, Bing Wang, Chang Liu, Zhenzhen Feng and Guang-Ping Zheng. "Ferroelectricity in novel one-dimensional $P4_2$-InSeI nanowires. " ***Results Phys.***, 31(3):104960 (2021)
4. **Shujuan Jiang**, Chang Liu, Pengyu Liu, Huabing Yin and Guang-Ping Zheng. "Electron-doping induced tunable magnetisms in 2D Janus TiXO (X=S, Se). " ***Physica E***, 145, 115518 (2023)
5. **Shujuan Jiang** and Guang-Ping Zheng. "The piezoelectricity and doping-induced ferromagnetism of Janus XYP_2 (X/Y=Si, Ge, Sn, and Pb; X≠Y) monolayers." ***Phys. Status Solidi B***, 2200269 (2022)

Acknowledgements

As I conclude my three-year Ph.D. research journey, I am overwhelmed with gratitude. Firstly, I express deepest appreciation to my supervisor, Professor Zheng Guangping. His guidance, encouragement, and insightful feedback have been pivotal in shaping this thesis. When confronted with scientific research problems, he gave me scientific and reasonable suggestions. He was very rigorous in revising articles and taught me a serious and responsible attitude towards academic research.

I would like to thank the colleagues of the research group for their assistance. They helped me solve many technical problems and added a lot of fun to my life. Heartfelt gratitude goes to my family and friends for their steadfast love and encouragement. They support me to carry on bravely in difficult situations.

This thesis is dedicated to all those who have helped me, whether it is academic ability or personal growth. Thank you all for being part of my journey.

Table of contents

CERTIFICATE OF ORIGINALITY I

Abstract II

List of publications VI

Acknowledgements VII

Table of contents VIII

List of figures XII

List of tables XIX

Chapter 1 Introduction 1

1.1 Background of two-dimensional materials 1

1.1.1 Graphene 3

1.1.2 Boron nitride (BN) 6

1.1.3 Transition metal dichalcogenides (TMDs) 8

1.1.4 Black phosphorene (BP) 10

1.2 Electrical property 13

1.2.1 Dielectricity 13

1.2.2 Piezoelectricity 19

1.3 Magnetic property 26

1.4 Janus structure 37

1.5 Motivation and objectives 39

Chapter 2 Research methodologies 44

2.1 Introduction of the first-principles calculation 44

2.2 Multiparticle system schrodinger equation and its solving 45
2.2.1 The Born-Oppenheier approximation 46
2.2.2 The Hartree-Fock approximation 48
2.3 Density functional theory 49
2.3.1 Hohenberg-Kohn theory 50
2.3.2 Kohn-Sham equation 51
2.4 Exchange correlation functional 52
2.4.1 Local-density approximation 53
2.4.2 Generalized Gradient Approximation 53
2.4.3 Hybrid density functional 54
2.5 The First Principles simulation packages 55
2.5.1 Vienna Ab-initio Simulation Package (VASP) 55
2.5.2 Phonopy 56
Chapter 3 2D Gallium oxychloride (GaOCl) 57
3.1 Introduction 57
3.2 Computational details 59
3.3 Results and discussions 60
3.3.1 Structure of bulk 60
3.3.2 Structure and stability of monolayer 62
3.3.3 Tunable electronic properties of monolayer 64
3.3.4 Carrier mobility of monolayer 67
3.3.5 Mechanical properties of monolayer 69

3.3.6 Hole-doping induced magnetism 72

3.3.7 Piezoelectricity of monolayer 75

3.4 Conclusions 77

Chapter 4 2D Janus Gallium oxychloride (GaOClX, X=F, Br, I) 79

4.1 Introduction 79

4.2 Computational methods 82

4.3 Results and discussion 83

4.3.1 Atomic structure and stability of monolayers 83

4.3.2 Electronic properties of monolayers 86

4.3.3 Carrier mobility of monolayers 88

4.3.4 Mechanical properties of monolayers 90

4.3.5 Piezoelectric properties of monolayers 93

4.3.6 Dielectric and energy-storage properties of monolayers 94

4.4 Conclusions 98

Chapter 5 Doping-induced magnetism in 2D monolayers 100

5.1 Doping-induced magnetism in 2D Janus TiXO (X = S, Se) monolayer 100

5.1.1 Introduction 100

5.1.2 Computational details 103

5.1.3 Results and discussion 104

5.1.4 Conclusions 117

5.2 Doping-induced magnetism in 2D Janus XYP$_2$ (X/Y= Si, Ge, Sn, and Pb; X≠Y) monolayer 119

5.2.1 Introduction 119

5.2.2 Computational details 121

5.2.3 Results and details 122

5.2.4 Conclusions 132

Chapter 6 High-entropy (MoWFeCoX)S_2 (X=Gd, Sm, and Nd) monolayers....... 134

6.1. Introduction 134

6.2. Computational details 136

6.3. Results and discussion 137

6.3.1 Structures and stability 137

6.3.2 Electronic properties 142

6.3.3 Optical properties 143

6.3.4 Mechanical properties 145

6.4. Conclusions 147

Chapter 7 Conclusions and outlooks 148

References 153

List of figures

Figure 1.1 Common types of two-dimensional materials [1]. 2

Figure 1.2 (a) The top view of structure of graphene [8]. (b) Energy band (left) in the Brillouin zone for graphene and Dirac-cone energy bands (right) at K point [9]. 4

Figure 1.3 Ambipolar electric field effect in single-layer graphene [11]...............5

Figure 1.4 (a) Crystallographic structure of BN. (b) Layered van der Waals structure of bulk h-BN and (c) planar view of an atomically thin sheet. (d) Thermodynamic P-T phase diagram for BN [16]. 6

Figure 1.5 (a) The configuration of 2H monolayer MoS_2. (b) The band structure of bulk, 4 layers, 2 layers, and monolayer MoS_2, respectively. (c) Band structure at K and -K showing the properties of spin splitting. (d) Absorption spectrum of monolayer MoS_2 [25]. 9

Figure 1.6 (a) Atomic structure of BP [31]. (b) Bandgap tuned with number of layers [32]. 10

Figure 1.7 Spectral response range of bandgap of typical 2D materials. 11

Figure 1.8 The diagram of charge separation in parallel-plate capacitor under the function of electric field. 14

Figure 1.9 Diagram of charging and discharging of a capacitor. 16

Figure 1.10 Diagram of hysteresis and energy storage density: (a) linear dielectrics, (b) ferroelectrics, (c) relaxor ferroelectrics, and (d) antiferroelectrics 17

Figure 1.11 (a) Atomic model of the wurtzite-structured ZnO [44]. (b) Schematic diagram of the piezoelectric effect.[45] 20

Figure 1.12 (a) The direction of applied stretch strain and (b) polarization on engineered graphene. (c) Graphene with different absorbed atoms.............22

Figure 1.13 (a) Comparison of the piezoelectric coefficient $d11$ between known piezoelectric materials and group IV monochalcogenides [54]. (b) Piezoelectric coefficients of Group-V binary monolayers [55]...................23

Figure 1.14 (a) Atomic structures of perfect and Janus group-III chalcogenide monolayers [57]. (b) Atomic structure of H and F modified Graphene. [58] 24

Figure 1.15 Illustration of the atomic arrangement for (a) AA′, (b) AB, and (c) BA stacking. (d) Small-angle twisted bilayer BN after the atomic reconstruction. (e) Vertical PFM phase and (f) amplitude images of twisted bilayer BN.....25

Figure 1.16 Basic magnetic structures of various magnetic materials.................27

Figure 1.17 Magnetization curves for a thin film of hafnium dioxide [42].........29

Figure 1.18 The side view and top view of five magnetic 2D materials: CrI_3, $Cr_2Ge_2Te_6$, Fe_3GeTe_2, $FePS_3$ and VSe_2 [68]. 30

Figure 1.19 (a) Micrograph of a representative CrI_3 flake. (b) Hysteresis loop of CrI_3 monolayer...31

Figure 1.20 (a) Hysteresis loop and of 2D Fe_3GeTe_2 at 78K. (b) The relationship between Curie temperature and hysteresis loop [79]..................................33

Figure 1.21 (a) VSe_2 monolayer grown on graphite and MoS_2. (b) M–H hysteresis loops of VSe_2 taken at 10 and 330 K [85]..35

Figure 1.22 Schematic illustration of (a) Mexican-hat band edge model and (b) density of states of Van Hove singularities. 36

Figure 1.23 Synthesis process and optical microscopy and atomic force microscopy images for each structure [100]..38

Figure 3.1 (a) The crystal structure of bulk GaOCl. The unit cell used is outlined by dash lines. (b) Electronic band structure (PBE and HSE06 levels) of bulk GaOCl. The Fermi level is set to zero..61

Figure 3.2 (a) Cleavage energy ($\mathrm{E}cl$) as a function of the cleavage distance (d_e) between the top layer and bottom layer of GaOCl and BP. The inset is the schematic diagram of the cleavage process in generating the GaOCl monolayer from its bulk counterpart. (b) Top view and side view of GaOCl monolayer. (c) Phonon spectrum of GaOCl monolayer. (d) The variation of temperature and total energy during AIMD simulations at 300 K. The inset is the snapshots of monolayer taken at the end of the simulation. 63

Figure 3.3 (a) Electronic band structure (at PBE and HSE06 levels) and partial density of states (PDOS) of GaOCl monolayer. The Fermi level is set to zero. (b) Electron density distribution at CBM and VBM. (c) The bandgap of GaOCl monolayer as a function of the in-plane uniaxial and biaxial strains ranging from − 6 % to + 6 %. 65

Figure 3.4 HSE06 band structures of GaOCl monolayer under the in-plane uniaxial strains varying from −6% to +6% along (a) x-, (b) y- and (c) xy-direction. 67

Figure 3.5 The total energy of GaOCl monolayer as a function of the uniaxial strain applied along (a) x-direction, and (b) y-direction, respectively. 69

Figure 3.6 The orientation dependent (a) in-plane Young’s modulus and (b) Poisson’s ratio of GaOCl monolayer. (c) The stress-strain relations under biaxial and uniaxial (x and y directions) tensions for GaOCl monolayer. 71

Figure 3.7 (a) Magnetic moment and spin-polarization energy as a function of hole concentration. (b) Spin-polarized partial density of states and the corresponding spin-density distribution under different hole doping densities. The yellow isosurfaces denote the spin charge density. (c) Doping-induced magnetic moment versus temperature at three different doping levels. 73

Figure 4.1 (a) Top view and (b) side view of atomic structure of GaOClX (X = F, Br, and I) monolayers. 84

Figure 4.2 The variation of temperature and total energy during AIMD simulations at 300 K of (a) GaOClF, (b) GaOClBr, and (c) GaOClI monolayers. The inset shows the snapshots of systems taken at the end of the simulations. The phonon spectra of (d) GaOClF, (e) GaOClBr, and (f) GaOClI monolayers along with the high-symmetric points in the Brillouin zone. 86

Figure 4.3 Electronic band structures (at the PBE and HSE06 levels), total density of states (TDOS) and partial density of states (PDOS) of (a) GaOClF, (b) GaOClBr, and (c) GaOClI monolayers. The Fermi level is set to be zero. .. 87

Figure 4.4 The orientation dependent (a) in-plane Young’s modulus, and (b) Poisson’s ratio of the Janus GaOClX (X = F, Cl, and Br) (solid lines) and GaOCl (dotted line) monolayers. 92

Figure 4.5 (a) The $Pmax$, Pr, and $Emax$ of systems studied. (b) The changes of bandgap values of systems studied under applied electric fields. The P-E loop of (c) GaOCl, (d) GaOClF, (e) GaOClBr, and (f) GaOClI monolayers. The orange and brown areas represent $Jreco$ and $Jloss$, respectively. 95

Figure 5.1 (a) Top view and (b) side view of TiXO (X = S, Se) monolayers. Hexagonal unit cell is indicated by a dotted gray line. The band structures and PDOS calculated using HSE06 functional for (c) TiSO and (d) TiSeO monolayers. The Fermi energy is set as zero. 104

Figure 5.2 The magnetic moment and spin polarization energy per electron as a function of doping density for (a) TiSO and (b) TiSeO monolayer. (c) Band structure and (d) PDOS of TiSO monolayer at a doping density n = $1.08\times10^{14}/\text{cm}^2$; the inset is the spin density at the same condition. The spin magnetic moment as a function of temperature for (e) TiSO and (f) TiSeO monolayer at different doping density. 107

Figure 5.3 Effects of strains on magnetic moments for (a) TiSO and (b) TiSeO monolayers. Effects of strains on spin polarization energy and TC for (c) TiSO and (d) TiSeO monolayers. 111

Figure 5.4 Five different possible stacking configurations for TiXO (X = S, Se) bilayers: (a) AA; (b) AB; (c) r-AA; (d) r-AB; (e)A'A................................ 113

Figure 5.5 The band structures of (a) TiSO and (b) TiSeO bilayer calculated on HSE06 level. The magnetic moment and spin polarization energy as a function of doping density for (c) TiSO and (d) TiSeO bilayers. The inset is the spin density at n = $1.08\times10^{14}/cm^2$ for TiSO bilayer.. 116

Figure 5.6 Top (a) and side (b) view of Janus XYP_2 monolayers. (c) The first Brillouin zone with high-symmetry points in the reciprocal space. 122

Figure 5.7 The phonon spectra of Janus XYP_2 monolayers. 124

Figure 5.8 The evolution of temperature and free energy during the AIMD simulation at 300 K for Janus XYP_2 monolayers (a) $SiGeP_2$, (b) $SiSnP_2$, (c) $SiPbP_2$, (d) $GeSnP_2$, (e) $GePbP_2$, and (f) $SnPbP_2$. The insets are the structures after 6 ps.. 125

Figure 5.9 Band structures and projected density of states (PDOS) of Janus XYP_2 monolayers (a) $SiGeP_2$, (b) $SiSnP_2$, (c) $SiPbP_2$, (d) $GeSnP_2$, (e) $GePbP_2$, and (f) $SnPbP_2$, as calculated by PBE (blue dotted line) and HSE06 (red solid line) methods, respectively. 126

Figure 5.10 The magnetic moment per doping carrier and the spin polarization energy at different hole-doping density for (a) $SiGeP_2$, (b) $GeSnP_2$, and (c) $SnPbP_2$ monolayers. 130

Figure 6.1 Top view (a-c) and side view (d-f) of 5 × 5 ×1 supercell of HE $(MoWFeCoX)S_2$ (X=Nd, Sm, and Gd) monolayers, respectively. (g) Corresponding metal-nonmetal bond length distribution and (h) average atomic displacement. 137

Figure 6.2 The PDOS of HE $(MoWFeCoNd)S_2$, $(MoWFeCoSm)S_2$, and $(MoWFeCoGd)S_2$ monolayers, respectively. The Fermi level is set to zero. 143

Figure 6.3 Calculated absorption coefficients of HE (MoWFeCoNd)S_2, (MoWFeCoSm)S_2, and (MoWFeCoGd)S_2 monolayers, respectively, with the incident light along x-, y-, and z-direction. 143

Figure 6.4 The polar diagrams representing (a) Young's modulus and (b) Poisson's ratio for all HE (MoWFeCoX)S_2 monolayers studied. 147

List of tables

Table 3.1 The electronic transport parameters of GaOCl monolayer: effective mass (m^*), elastic moduli (C), deformation potentials (E_d), and carrier mobility (μ). 67

Table 3.2 Calculated piezoelectric coefficients eij (pC/m) and dij (pm/V) for GaOCl monolayer. 76

Table 4.1 Calculated lattice constants a and b, interlayer thickness d, bond length of Ga-O, Ga-Cl, and Ga-X bonds, cohesive energy E_{coh}, and bandgaps E_g obtained with PBE and HSE06 for GaOClX (X = F, Br, and I) monolayers. 85

Table 4.2 Calculated effective mass (m^*), 2D elastic modulus (C), deformation potential constant (E_d), and mobility (μ) of electrons and holes along x- and y-directions at 300 K for the Janus GaOClX (X = F, Cl, and Br) monolayer. 88

Table 4.3 Calculated elastic modulus Cij (N/m) and piezoelectric coefficient eij (pC/m) and dij (pm/V) for Janus GaOClX monolayers. 90

Table 4.4 The maximum applied field $Emax$ (V/Å), polarization $Pmax$ (μC/cm^2) at $Emax$, remnant polarization Pr (μC/cm^2), recovery energy density $Jreco$ (J/cm^3), energy storage density $Jstor$ (J/cm^3), and energy storage efficiency η (%) of GaOCl and Janus GaOClX monolayers. 96

Table 5.1 Optimized lattice constant, thickness, bond length, and calculated HSE06 bandgap of TiSO and TiSeO monolayers. 105

Table 5.2 Lattice constant a, interlayer distance d, and binding energy E_b of optimized structures with five possible stacking orders for TiXO (X = S, Se) bilayer..114

Table 5.3 The calculated structural parameters (lattice constants a, bond length, and ΔZ), values and type of bandgap of Janus XYP_2 monolayers. 123

Table 5.4 The calculated elastic constants Cij (N/m), Young's modulus $Y2D$ (N/m), layer modulus $\gamma 2D$ (N/m), and Poisson's ratio v.........................127

Table 5.5 The calculated piezoelectric coefficients eij (pC/m) and dij (pm/V). 128

Table 6.1 The lattice constants a and b (Å), layer thickness (Å), MSD ($Å^2$), formation energy $Eform$ (eV/atom), formation enthalpy ΔHf(eV/f.u.), and estimated temperature T (K) at which the five-cation HE systems are more stable than the parent sulfides for HE $(MoWFeCoX)S_2$ monolayers, respectively. 139

Table 6.2 Independent elastic constants C_{ij} (N/m) of HE $(MoWFeCoX)S_2$ monolayers...145

Chapter 1 Introduction

1.1 Background of two-dimensional materials

The dimensionality of materials plays a crucial role in their fundamental physical, chemical, and other properties. Two-dimensional (2D) materials, characterized by their single-layer or few-atom-thick structure, typically have thickness dimensions ranging from atomic monolayers to the nanometer scales. Due to electron confinement to two dimensions, 2D systems reveal unique physical and chemical properties distinct from bulk materials. Common 2D materials include graphene, hexagonal boron nitride (h-BN), transition metal dichalcogenides (such as molybdenum disulfide and tungsten disulfide), among others. 2D materials can be prepared through synthesis routes such as mechanical exfoliation from bulk phases, chemical vapor deposition (CVD), and molecular beam epitaxy. 2D materials possess larger specific surface areas, higher carrier mobility, and richer electronic performance in comparison to their bulk counterparts. Consequently, 2D materials hold potential developments in fields such as energy storage, photovoltaics, biosensing, catalysis, and beyond.

Compared to bulk materials, 2D materials demonstrate distinct advantages and high-performance characteristics. Firstly, 2D materials possess excellent flexibility and transparency due to their thin and controllable thickness, meeting the demands of next-generation optoelectronic devices. Secondly, electronic motion is confined to the 2D level, resulting in novel electronic and optical properties different from bulk counterparts, namely, quantum confinement effects. The dielectric screening effect can be weakened, resulting in significantly enhanced electron-electron interactions and strong excitonic effects. Absorption efficiency is enhanced as well. Thirdly, strong intralayer covalent bonding combine with weak interlayer van der Waals interactions endow 2D materials with strong mechanical strength. Fourthly, large surface area as well as natural passivation provide abundant possibilities for constructing vertically stacked heterostructures and avoiding lattice mismatch issues present in traditional heterostructures.

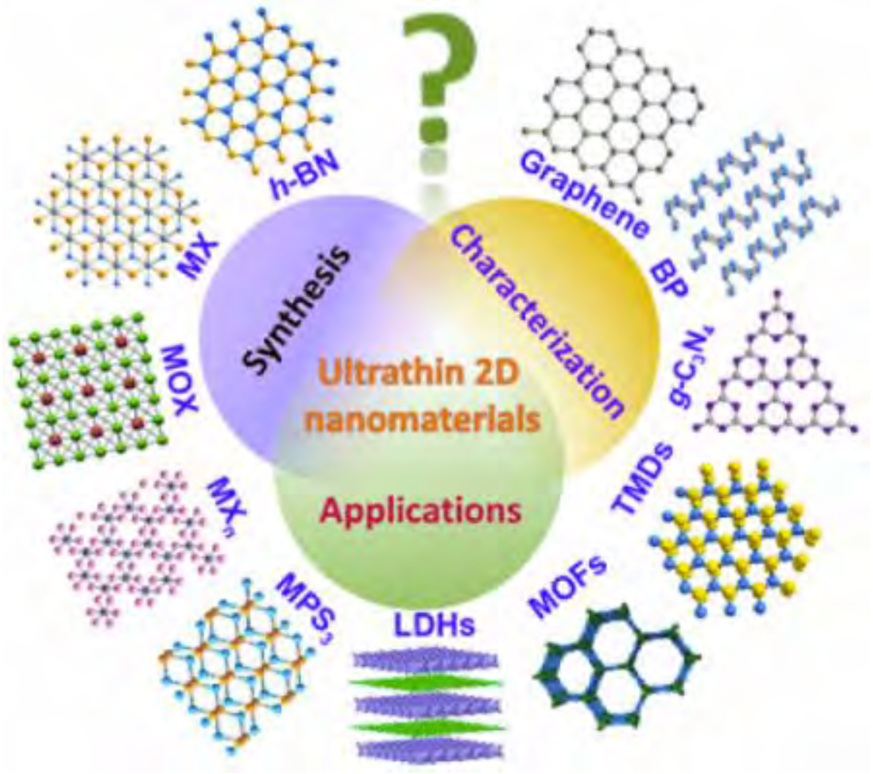

Figure 1.1 Common types of two-dimensional materials [1].

However, 2D materials have certain limitations. Firstly, some existing 2D systems are prone to oxidation and degradation in ambient condition, leading to structural damage and performance degradation. Therefore, developing 2D materials with both good performance and strong stability is challenging. Secondly, experimental and theoretical studies that most 2D materials exhibit the bandgap smaller than 2.5 eV, limiting their applications in high-frequency and high-power electronics, as well as optoelectronics in blue and ultraviolet light. Thirdly, the quantity of high-performance 2D materials that can be successfully synthesized in the laboratory are still relatively inadequate, which is also a factor inhibiting the development of 2D materials. Several traditional 2D materials are introduced below.

1.1.1 Graphene

In 2004, Novoselov *et al.* successfully obtained graphene from its monolithic-state graphite using mechanical exfoliation [2], which challenged the scientific understanding of 2D materials. This landmark discovery is also considered as one of the great achievements in materials science and technology. Graphene possesses the honeycomb structure (hexagonal crystalline single layer) with one carbon atom in each site, as shown in Figure 1.2(a). It is the thinnest and strongest nanomaterial with a thickness of 0.34 nm currently discovered [3]. It can form different forms such as zero-dimensional fullerenes, one-dimensional nanotubes and three-dimensional graphite. Each carbon atom connects to three next-nearest atoms with covalent σ bonds, forming sp^2 hybridisation combiningwith p_x and p_y orbitals [4]. There is a free electron including both low-energy and high-energy electron states hold by p_z orbitals, vertical to the plane to form the π bonds. Each C-C bond distance is only 0.142 nanometres [5], indicating strong connection between each carbon atom. When a force is applied to graphene, the surface of the atoms inside deforms and bends to counteract the force. There is no rearrangement or misalignment between the carbon atoms and the structure remains stable [6].

According to the calculated band dispersion shown in Figure 1.2(b), one can clearly find that the energy band at high symmetric K point in Brillouin region is linear. If the three-dimensional (3D) image is drawn, there will be a cone-like structure, namely Dirac point. There is no bandgap at the Dirac point, that is, the bottom of conduction band and the top of the valence band intersect at this point. Fermi surface crosses this point at the same time. It is suggested that the graphene is a semiconductor with zero bandgap, which is usually called semi-metal. It has a finite temperature range of conductance with the possibility of forming a complete conductor under thermal excitation. In the semiconductor field, 2D materials with non-zero bandgap is more attractive for practical applications. Many techniques have been developed to overcome the zero-bandgap issue and make graphene with appropriate band gaps, including doping, introducing defects and vacancies into graphene, or designing heterojunction with graphene [7].

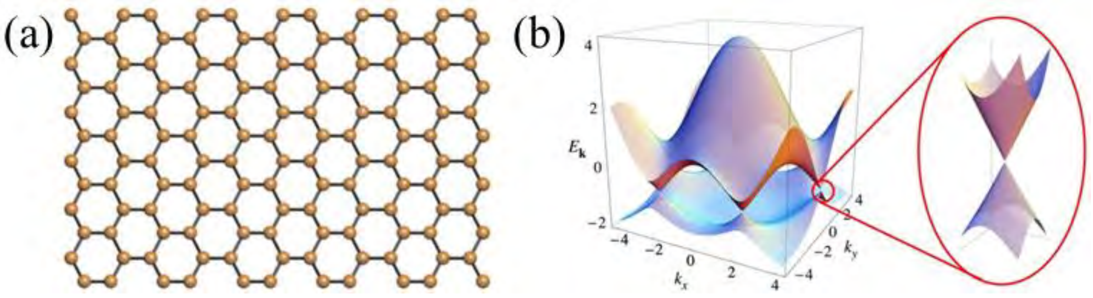

Figure 1.2 (a) The top view of structure of graphene [8]. (b) Energy band (left) in the Brillouin zone for graphene and Dirac-cone energy bands (right) at K point [9].

Theoretical calculations have revealed that graphene has high carrier mobility and ambipolarity, motivating further experimental measurement and verification. Those efforts allow the graphene to be developed into promising applicant for next-generation semiconductor applications. High-quality graphene crystal could be treated as the important criterion for the aforementioned excellent electronic properties. Namely, the density of defects, acting as the scattering centers to inhibit carrier transport, must be low. Kim *et al*. reported that the single-layer graphene exfoliated mechanically possess the electron mobility over 2×10^5 cm^2 V^{-1} s^{-1} [10]. More importantly, the carrier could migrate ballistically on the micrometre scales at room temperature, which could be very important in semiconductor industry. The ambipolar field-effect of graphene suggests that the electrons and holes could be tuned continuously under the applied gate bias, which could result from the characteristics of its Dirac point. To be specific, the Fermi level could drop (or raise) with negative (or positive) bias around the Dirac point, introducing the holes (or electrons) populate to valence band (or conduction band), see Figure 1.3 [11]. Different with the traditional logic devices based on silicon, the ambipolar semiconductor devices based on graphene could realize the dynamical control without physical changes.

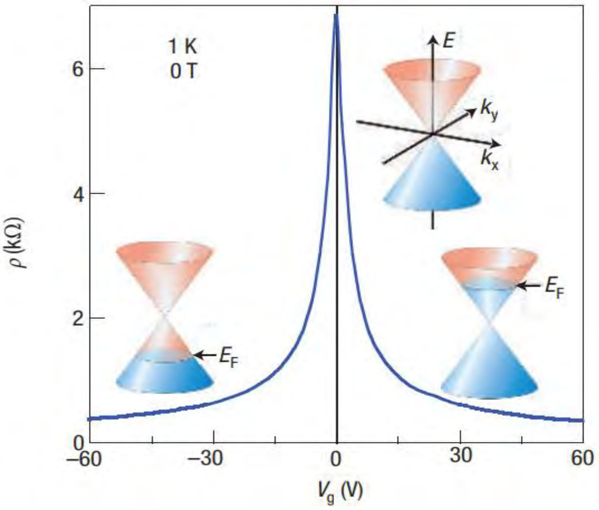

Figure 1.3 Ambipolar electric field effect in single-layer graphene [11].

Graphene quantum dots are nanometre-sized portions of graphene with a diameter below 20 nm, where carrier transport is limited in three dimensions. Theoretical study and experimental studies have revealed their distinct properties, which endows them potential candidates for electronic devices. Because of the quantum confinement effect, graphene quantum dots possesses a non-zero bandgap which is tuneable by adjusting its size and surface chemistry [12]. There is a oblivious absorption peak in spectra of graphene quantum dots [13]. Their extra functional groups also could result in the unique optical property and influence the photoluminescence properties [14]. Compared with semiconductor quantum dots, graphene quantum dots possess the wider photoluminescence bandwidth and its maximum could be modulated with increasing excitation wavelength [15].

1.1.2 Boron nitride (BN)

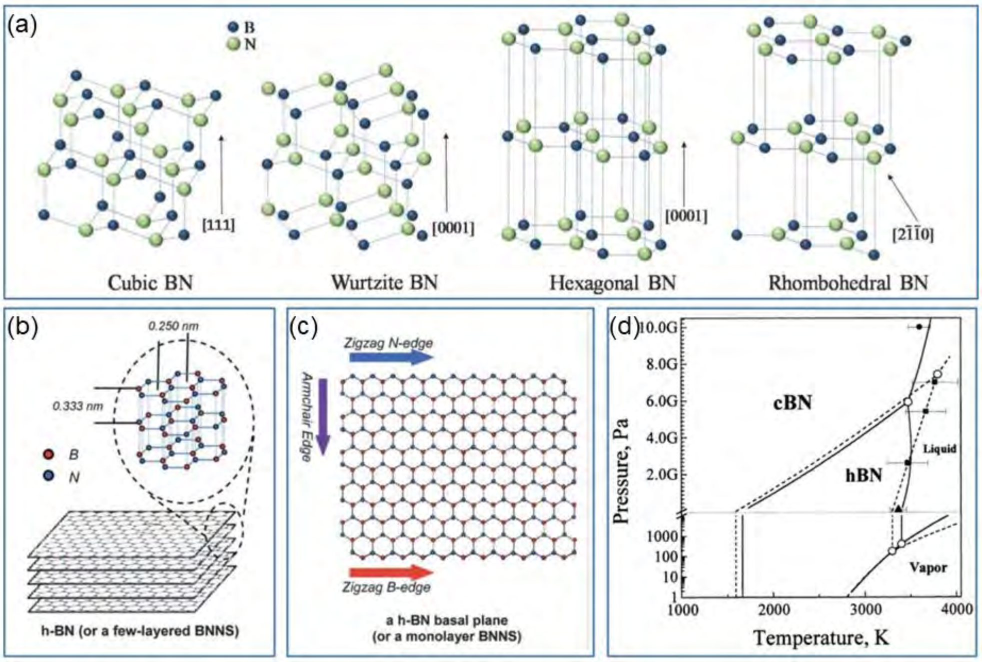

Figure 1.4 (a) Crystallographic structure of BN. (b) Layered van der Waals structure of

bulk h-BN and (c) planar view of an atomically thin sheet. (d) Thermodynamic P-T phase diagram for BN [16].

Ceramics are pivotal in engineering, widely utilized from heat shields for spacecraft to cutting-edge electronic devices' gate dielectrics. Boron nitride (BN), maintaining a B and N stoichiometric ratio of 1:1, stands as a III-V compound with insulating properties, contrasting with semiconductors like Ga-N and In-P. Though it is synthetic traditionally [17], crystalline BN has also been found in geological formations resembling its synthetic counterparts [18].

There are several kinds of stable structures of BN, as shown in Figure 1.4(a). It is mainly divided into sp^3 bonded and sp^2 bonded forms [19]. Cubic BN (c-BN), with a zincblende crystal structure, comprises overlapping face-centered cubic (fcc) lattices of B and N atoms, akin to diamond. Wurtzite BN (w-BN) features a hexagonal lattice configuration resembling rare lonsdaleite. It generally formed under extreme temperature and pressure [20]. Hexagonal BN (h-BN) has layered structure and belong to P63/mmc space group. It is similar to graphite with two different element types [21]. Alternating boron and nitrogen atoms form sp^2-bonded hexagonal framework with robust in-plane σ bonds (see Figure 1.4(b-c). Such strong interaction leads to high thermal conductivity and chemical stability. This structure renders h-BN electrically insulating [22]. Because N element have high electronegativity, it is ready to form B-N ionic bonds. In h-BN structure, layered interaction result in AA′ stacking order. Nitrogen atoms distribute directly below the boron atoms in the previous layer. AB arrangement is occasionally discovered in h-BN thin films. Moreover, rhombohedral

BN (r-BN) keeps to ABC stacking sequence. The boron atoms sit on top of the nitrogen atoms, but the first and third layers are misaligned. Generally, c-BN structure has the most favourable thermodynamicity. Other construction of BN is meta-stable and can exist finally because comparatively higher transformation energy. For example, transitioning from h-BN to c-BN requires approximately 6.5 ~10.8 eV/atom (experimentally) or 9.4 eV/atom (theoretically) (Figure 1.4 (d) [23].

1.1.3 Transition metal dichalcogenides (TMDs)

TMDs is a layered structure, similar to the single-atom graphene structure. These systems consist of two layers of chalcogenide atoms sandwiched between one layer of transition metal atoms (such as elements in group IV, group V, or group VI), forming a sandwich form (A-B-A). Adjacent layers stack together through van der Waals interaction. Different stacking order determine different symmetry and structure of corresponding bulk, including 1T, 2H, and 3R. 2H-MoS_2 is the typical TMDs with sandwich structure, as shown in Figure 1.5 (a). Molybdenum atoms are in the middle layer and bonded with six sulphur atoms. Chalcogen atoms are lie in top and bottom layers. Bulk MoS_2 has an intrinsic layered structure, exhibiting semiconductive properties with an indirect bandgap [24]. When it is exfoliated to a single layer, both conduction band minimum (CBM) and valence band maximum (VBM) are lied at the two inequivalent high-symmetry points, turning it to a direct bandgap monolayer. Its bandgap value also increases from 0.88 eV (bulk) to 1.71 eV (monolayer), see Figure 1.5(b). Moreover, the d-orbital of Mo atoms bring MoS_2 monolayer strong spin-orbit coupling (SOC), resulting in opposite spin splitting at K and -K valleys, see Figure 1.5(c). Simultaneous emergence and interaction of spin and valley degrees of freedom make it promising in valleytronic and spintronic device applications.

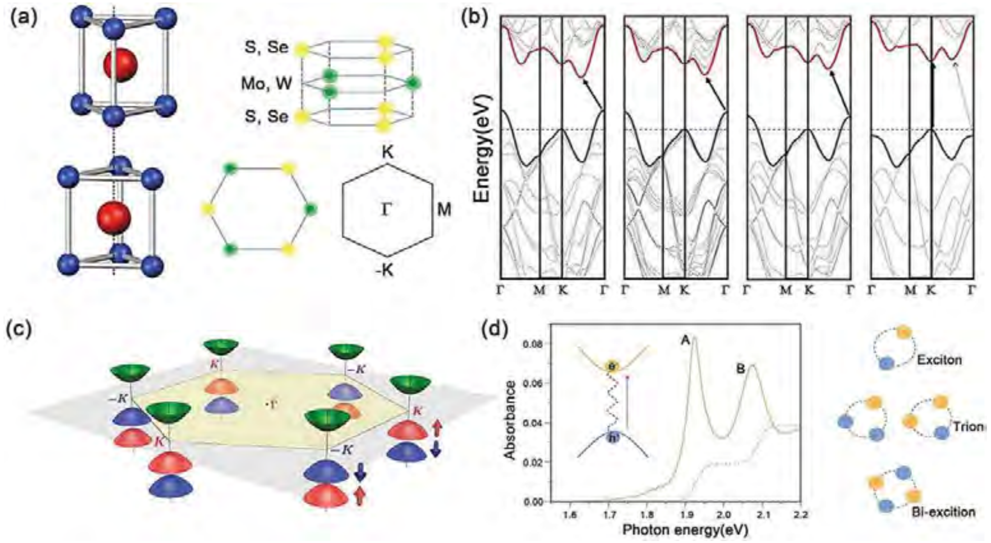

Figure 1.5 (a) The configuration of 2H monolayer MoS_2. (b) The band structure of bulk, 4 layers, 2 layers, and monolayer MoS_2, respectively. (c) Band structure at K and -K showing the properties of spin splitting. (d) Absorption spectrum of monolayer MoS_2 [25].

Different with zero-bandgap graphene and wide-bandgap h-BN, MoS_2 monolayer possesses suitable bandgap values and are potential for field-effect transistor (FET) and optical applications. However, the relatively low carrier mobility of 0.5-3 $cm^2 V^{-1} s^{-1}$ as obtained in experiments shows that it has disadvantages in device applications [26]. A recent study solves this deficiency and improves its mobility to 200 $cm^2 V^{-1} s^{-1}$. It firstly realized MoS_2-based transistor with on/off ratio up to 1×10^8. In addition, MoS_2 monolayer can be used to construct vertical heterostructure with graphene to build an FET, which is promising in information storage [27].

Figure 1.5(d) displays optical property of MoS_2 monolayer. Its robust excitonic effects leads to intense oscillatory intensity transfer and high excitonic radiative rates. They are indispensable in optoelectronics applications [28]. For instance, theoretical calculation indicates that the heterostructure consisting of MoS_2 and C_2N can be a promising candidate for photovoltaic applications [29]. It can also be applied as photodetector as well as excitonic light-emitting diodes since the good performance in light absorption [30].

1.1.4 Black phosphorene (BP)

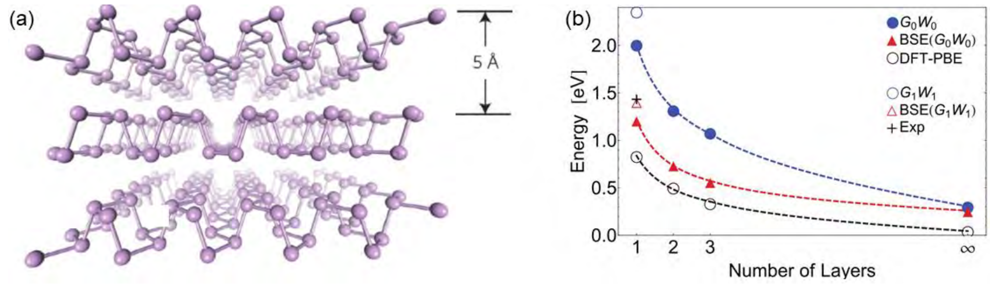

Figure 1.6 (a) Atomic structure of BP [31]. (b) Bandgap tuned with number of layers [32].

BP has garnered widespread attention due to its superior performance since its successful mechanical exfoliation in 2014 [31]. Its bulk consists of folded layered structures, which are bounded by weaker vdW forces, see Figure 1.6(a). The valence electron distribution of phosphorus atoms is $3s^2 3p^3$. Each phosphorus forms bonds with three neighbouring phosphorus, leaving behind a lone pair of electrons and constituting sp^3 hybridization. Studies have shown that BP possesses a direct bandgap tunable with its layer number, where the bandgap value rises from 0.3 to 2.0 eV as dimensionality decreases [32]. It exhibits significant quantum confinement effects. Under tensile and compressive strains, its band structure undergoes changes, leading to a metal-to-semiconductor transition.

Adjustable bandgap enable BP to spectral responses from visible to infrared light, thus filling lacks between zero-bandgap graphene and TMDs, as depicted in Figure 1.7 [33]. Importantly, BP demonstrates remarkably high carrier mobility as confirmed by both theoretical predictions and experimental measurements, indicating its hole mobilities surpass those of TMDs by several orders of magnitude (reaching up to 10^4). These characteristics make BP an ideal candidate material for optoelectronic applications.

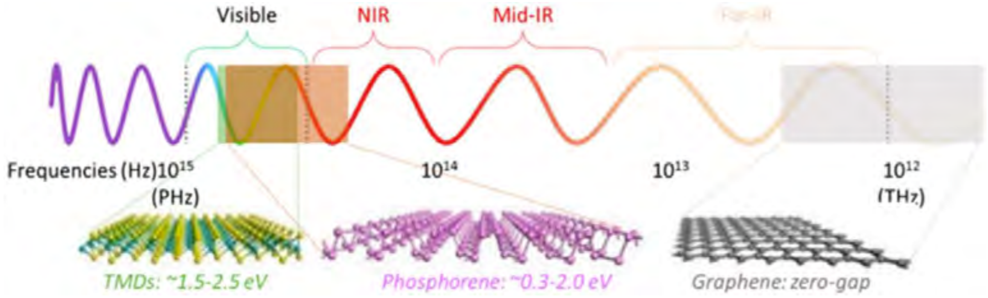

Figure 1.7 Spectral response range of bandgap of typical 2D materials.

However, BP faces a critical weakness, namely, its susceptibility to oxidation and degradation in air. Oxidation leads to structural degradation of BP, severely impacting its electronic and optical absorption properties. To address the instability of BP, researchers have explored various approaches (e.g. encapsulating BP with h-BN) to mitigate its susceptibility to oxidation. Nevertheless, such methods come with added economic costs. Therefore, it is imperative to identify 2D systems with suitable direct bandgaps and strong stability in ambient condition in regards to practical applications.

In addition, there are other 2D materials developed in this age of nanotechnology. With large photo-responses and in-plane anisotropy, layered post-TM chalcogenides are promising 2D semiconductors. For example, Bi_2Se_3 is investigated as thermoelectric candidate while many reports focus on its topological properties in recent years. Layered TM oxides are also studied widely due to their intercalation reactions similar to that of silicates. The polarity of O^{2-} endows them with non-linear and large-scale charge distributions, thus leading to potential surface and interfacial properties. Because the existence of special ionic bonds, layered halide perovskites (ABX_3) show unique properties from other 2D semiconductors. Here, A, B and X represent monovalent, bivalent cations and halogen, respectively. This system is regarded as solution type 2D system with exciting optical performance. Moreover, layered 2D carbide and nitride MXenes ($M_{n+1}X_n$, where M and X represent early TM and carbide or nitride, respectively) are also explored for their optoelectric behaviours. In most cases, numerous surface functional groups and TM carbide/nitride conductivity endow MXenes with valuable electronic and optical applications. 2D metal-organic framework (MOF) is a potentially porous extended structure consisting metal ions and organic linkers. They own large contact area, adjustable proportion of empty space, various choice of functional groups. It is useful for catalystic applications.

It is no doubt there is a series of challenges as well as opportunities in 2D materials field. Although research on 2D materials has been increasing in last twenty years and some significant progresses have been made, studies on this field are still far from mature. The most forthright direction is to discover and explore novel 2D materials. 2D materials with excellent electronic and ferromagnetic properties are being studied, making them a broad platform for nano- and atomic-level applications.

1.2 Electrical property

1.2.1 Dielectricity

Dielectricity refers to the property of a material which can be highly polarizable. In dielectric materials, charged particles are bound tightly by atomic or molecular internal forces and intermolecular forces. According to the criteria whether the centres of positive and negative charges of bound charges coincide or not, dielectric molecules can be divided into polar molecules and nonpolar molecules. The dielectric is electrically neutral in the absence of an applied electric field. However, once there is an electric field, the internal charge will be affected and response to it. In general, the positive and negative charges in dielectric form an electric dipole moment and undergo directional alignment, resulting in a nonzero sum of electric dipole moment vectors termed as polarization intensity (P, C/m^2) as expressed in Equation 1.1:

$$P = \frac{\Sigma p}{\triangle V} \quad , \qquad 1.1$$

where P, p, and $\triangle V$ represents the polarization intensity, electric dipole moment, and $\triangle V$ denotes the unit volume, respectively.

The dielectric constant is an important parameter reflecting the polarization performance of dielectric materials. Inserting a dielectric between two parallel conductive plates forms a capacitor, see Figure 1.8 [34]. According to the polarization effect of the dielectric, a potential difference will occur between substrates and thus storing charges under electric fields. The capacitor has a capacitance C, adefined as follows:

$$C = \frac{Q}{U} = \frac{\varepsilon S}{d} \quad , \qquad 1.2$$

where C, Q, U, ε, S, and d represent the capacitance, induced surface charge, potential difference between the plates, dielectric constant, and effective electrode area, respectively.

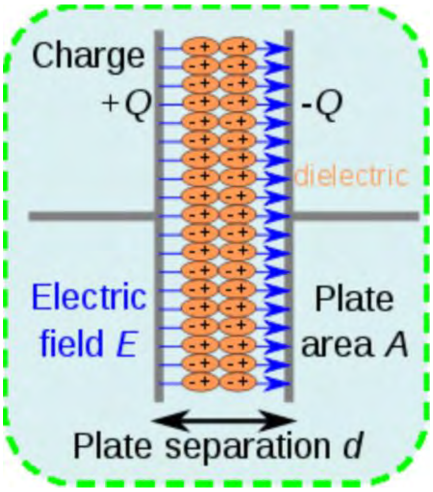

Figure 1.8 The diagram of charge separation in parallel-plate capacitor under the function of electric field.

When the externally applied electric field reaches a critical threshold, there is a sudden increase in internal current. It results in a transition from dielectric state to conductive state in dielectric materials, which is known as dielectric breakdown. The corresponding critical electric field is termed breakdown strength (E_B). There are two types of determinants that affect the occurrence of breakdown and the magnitude of breakdown voltage in dielectrics. One is intrinsic properties of the dielectric itself. Another is external factors such as electric field distribution, temperature, heat dissipation conditions, and properties of surrounding media. Moreover, it is influenced by the rate of pressure application and the duration of voltage application. Solid dielectric breakdown primarily manifests in two forms: electrical breakdown and thermal breakdown [35].

Electrical breakdown refers to the process wherein a solid dielectric loses its dielectric properties with effect of high electric field, which could result from the accumulation of sufficient quantity and energy of charge carriers within the dielectric material. The main mechanisms of electrical breakdown include three types: collision ionization breakdown, avalanche breakdown, and tunnelling breakdown. When the thermal energy generated by conduction current and displacement current under alternating electric fields in a dielectric cannot dissipate quickly enough, excessively high local temperatures are induced within the dielectric until insulation properties are compromised. Consequently, thermal breakdown is correlated with dielectric losses, thermal conductivity, and heat dissipation conditions.

The actual breakdown behaviour of dielectrics often involves a complex interplay of multiple mechanisms, including electrical and thermal effects. Moreover, the unevenness of dielectrics caused during sample preparation and processing, as well as the increase in sample thickness, can significantly influence the breakdown strength.

A dielectric capacitor functions by storing energy through the maintenance of opposite charges on electrodes separated by dielectric materials. It stands out among energy storage devices for its ability to discharge stored energy rapidly, generating powerful pulses in microseconds [36]. This ability facilitates numerous pulse power applications. In such uses, capacitors transform low-energy, prolonged inputs into high-energy, brief outputs. In dielectric systems, the energy storage density can be determined as:

$$J = \int_0^{E_B} PdE \quad . \tag{1.3}$$

Namely, J can be estimated by integrating the product of electric field strength E and polarization intensity P. Figure 1.9 shows the energy density during charging and discharging of a capacitor [37, 38]. As the electric field increases from zero to its maximum E_B, polarization also increases to its maximum P_{max}, storing electrical energy J in the capacitor, as depicted by the blue and pink areas. During discharge from E_B back to zero, the recoverable electrical energy density J_{loss} is released, as represented by the pink area. However, hysteresis loss is inevitable in the process of depolarization. A portion of the stored energy J_{rec} (shaded in blue) is dissipated. Consequently, the energy-storage efficiency can be defined based on these observations:

$$\eta = \frac{J_{rec}}{J_{loss}+J_{rec}} \times 100\% \quad . \tag{1.4}$$

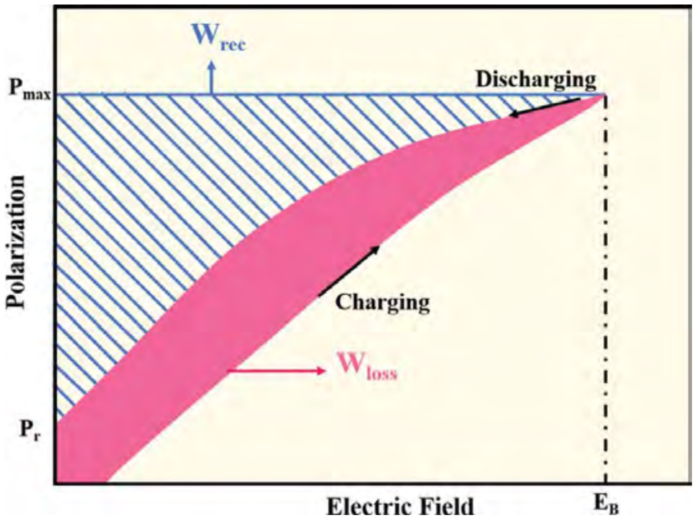

Figure 1.9 Diagram of charging and discharging of a capacitor.

From Figure 1.9, it can be observed that energy storage performance is related to the magnitude of polarization as well as variation of electric field (described by hysteresis loop). Figure 1.10 provides diagram for four types of common energy storage dielectric materials, including linear dielectrics, ferroelectrics, relaxor ferroelectrics, and antiferroelectrics [39, 40]. They are discussed separately in the following.

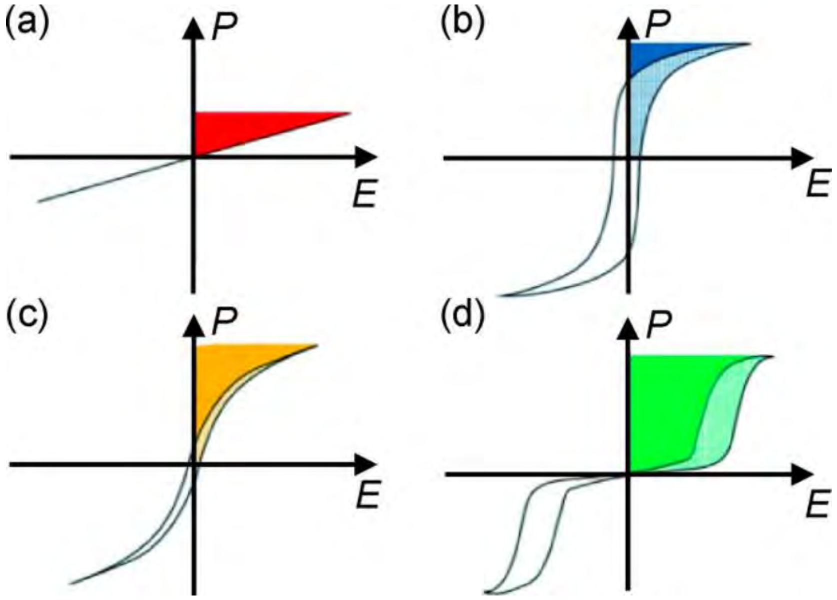

Figure 1.10 Diagram of hysteresis and energy storage density: (a) linear dielectrics, (b) ferroelectrics, (c) relaxor ferroelectrics, and (d) antiferroelectrics

For linear dielectric materials, polarization intensity P is linearly proportional to electric field strength E. Its dielectric property is independent of the electric field. Therefore, the capacity of linear dielectrics for storing energy can be expressed as: $J = \frac{1}{2}\varepsilon_r\varepsilon_0 E^2$, where ε_r and ε_0 represents relative permittivity and permittivity in vacuum, respectively. All energy stored in the linear dielectric materials in charging process could be released during discharge.

Ferroelectric materials exhibit spontaneous polarization within a certain temperature range, which can be regulated through external electric field. For energy storage applications, they feature comparatively high maximum polarization and modest breakdown strength. However, large residual polarization leads to smaller utilizable energy storage density as well as efficiency. Furthermore, their breakdown field strength is relatively low (< 100 kV/cm). Therefore, despite their favourable piezoelectric and pyroelectric properties, they are generally unsuitable for applications as energy storage materials.

Relaxor ferroelectrics are a class of ferroelectric materials with diffuse phase transitions, possessing the fundamental properties of ferroelectric materials: spontaneous polarization phenomenon and reversibility under external electric field. They also have relatively high dielectric constants. The main characteristics that distinguish relaxor ferroelectrics from ordinary ferroelectrics are smaller residual polarization intensity, lower coercive field, and relatively "slender" hysteresis loops. These factors are crucial for achieving higher energy storage density and efficiency.

Within the certain temperature scope, antiferroelectric materials possess adjacent dipoles oriented in reverse parallel and behave zero macroscopic spontaneous polarization. When external electric field is small, their dipole moments cancel each other out. While electric field becomes larger, there will be a phase transition from antiferroelectric to ferroelectric. Antiferroelectric materials exhibit double hysteresis loop shapes, characterized by low residual polarization and high spontaneous polarization. This property offers significant potential for achieving high energy storage density.

So far, most dielectric materials utilized in energy storage have been concentrated in perovskite and its various derivative ceramics. For example, $SrTiO_3$ and Al_2O_3 exhibit relatively larger breakdown strength and smaller dielectric losses. Due to their low dielectric constants, their energy storage density is usually lower than 1 J/cm^3. Zr-doped $CaTiO_3$ [41] and Mg-doped $SrTiO_3$ [42] ceramics are prepared with smaller grain size, leading to a decrease in the average field strength at boundaries. Thus, the breakdown electric field significantly increases, as well as the energy storage density and efficiency. As lead-free ferroelectricity and piezoelectricity in early stage, $BaTiO_3$ has large dielectric values and low dielectric loss. However, its lower Curie temperature limits its operating temperature. Relaxor ferroelectrics mainly include $BaTiO_3$-based, $(Bi_{0.5}Na_{0.5})TiO_3$-based, $(K_{0.5}Na_{0.5})NbO_3$-based, $NaNbO_3$-based systems. Compared with other energy storage dielectrics, their energy storage performance is relatively poor. Antiferroelectric $AgNbO_3$ are reported to improve the energy storage capability by Ta-modification [43]. With the growing request for maintainable energy sources, relevant researches are gradually increasing. 2D materials have unique structures and properties, which may offer excellent energy storage performance, such as high dielectric constant, low resistivity, and excellent electronic transport properties.

1.2.2 Piezoelectricity

In the 19th century, Curie brothers found the piezoelectric effect on quartz, which can effectively convert signals between mechanical domain and electrical domain. Generally, piezoelectric effect occurs in two situations. The positive piezoelectric effect refers to the phenomenon that applied pressure or strain on crystal material result in electrical polarization. Conversely, the negative piezoelectric effect refers to the phenomenon where the application of electric fields on piezoelectric materials leads to strain or deformation. Both of these conversion in crystals is reversible. The following takes ZnO as an example to elaborate, as shown in Figure 1.11(a) [44]. Due to the effective overlap of Zn^{2+} and O^{2-} centers, there is no polarization phenomenon in the absence of external stress. When ZnO tetrahedra is subjected to external forces, the positive and negative charge centers move in opposite directions. An electric dipole moment is generated along the direction of the force. The continuous superposition of dipole polarizations produces a macroscopic potential, namely piezoelectric potential (Figure 1.11(b)) [45]. Studies have shown that the piezoelectric effect occurs in non-metallic materials with non-centrosymmetric crystal structures [46] Their electronic structure and mechanical property impact significantly on piezoelectricity. Generally, piezoelectric materials have electronic bandgaps, which can prevent current leakage.

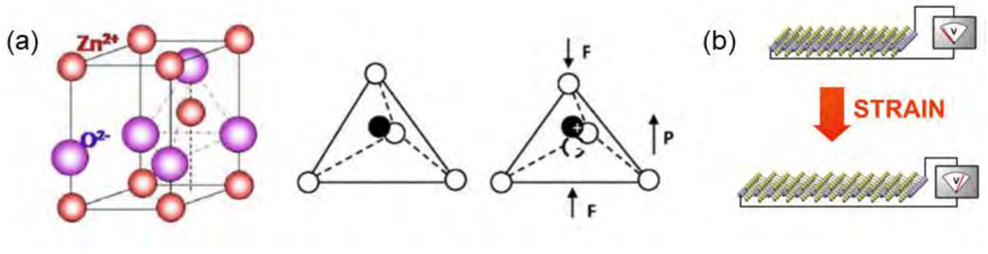

Figure 1.11 (a) Atomic model of the wurtzite-structured ZnO [44]. (b) Schematic diagram of the piezoelectric effect.[45]

In the past 140 years or so, studies in piezoelectric materials have continued to grow since piezoelectric devices are ubiquitous, such as quartz oscillators, actuators, sensors, acoustic storage devices, and energy harvesters. In addition to traditional quartz, sphalerite and wurtzite piezoelectric materials, the rapid development of perovskite piezoelectric materials has also provided industrial raw materials for electromechanical applications. In 1946, barium titanate ceramics were found to exhibit piezoelectric properties, leading to the rapid development of ceramic piezoelectric materials. In 1954, Jaffe *et al.* discovered that lead-containing perovskite ceramics, such as PZT. Their exceptionally high piezoelectric properties endow them as industrial piezoelectric materials [47]. Subsequently, lead-containing perovskite materials experienced vigorous growth with excellent piezoelectric properties, such as KNN perovskite, barium calcium titanate, BNT perovskite, and barium calcium iron titanate. In 2004, the piezoelectric coefficient d_{33} of KNN perovskite materials reached 416 pC/N [48], which has been enhanced to 700 pC/N in 2018, surpassing that of lead-containing PZT materials [49]. Besides, barium calcium titanate ceramics (BCTZ) were reported to have a tremendous piezoelectric strain coefficient d_{33} of 2027 pm/V, elevating the piezoelectric coefficient of 3D perovskite piezoelectric materials to the magnitude of 10^3 pm/V [50].

The piezoelectric effect in 2D materials emerged in 2012, generally origin from three sources: loss of central symmetry, charge delocalization and surface modification. Chandratre *et al.* [51] achieved piezoelectricity by creating triangular holes on graphene. This disrupts its intrinsic non-piezoelectric nature because the absence of inversion symmetry center, as illustrated in Figures 1.12(a-b). Ong *et al.* also obtained noncentrosymmetric graphene as well as piezoelectricity with a different approach [52]. They engineered graphene by chemical doping with different proportions of single atoms (H, Li, K, F) or diatomic molecules (LiF, HF) at various vacancies, as depicted in Figure 1.12(c). Subsequently, the piezoelectric properties of TMD and h-BN have also been investigated [45]. While bulk counterparts are not piezoelectric materials, their 2D monolayers exhibit intrinsic piezoelectricity due to broken inversion symmetry. As the typical piezoelectric effect is small, there is ongoing exploration to identify 2D materials with great piezoelectric coefficients. Through adsorbing varying proportions of H or F atoms to the surfaces of different configurations of graphene and h-BN, not only in-plane piezoelectric effects but also out-of-plane piezoelectric effects are induced [46, 53]. However, the piezoelectric response of these systems still inferior to that of 3D piezoelectric materials.

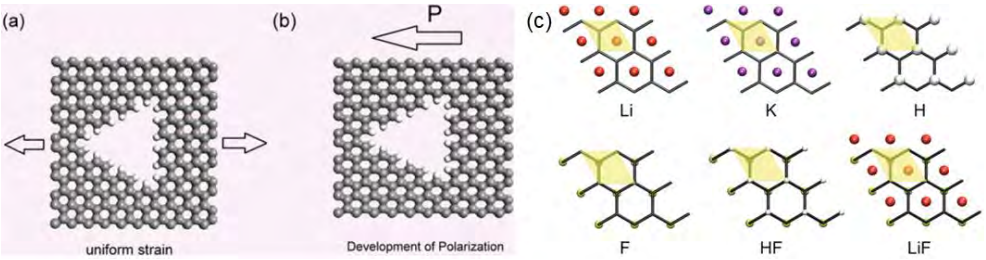

Figure 1.12 (a) The direction of applied stretch strain and (b) polarization on engineered graphene. (c) Graphene with different absorbed atoms.

In 2015, Yang *et al*. studied the piezoelectric property of Group IV monolayer sulfides [54]. They found that the in-plane piezoelectric strain coefficient d of GeS, SnS, GeSe, and SnSe reach highest among all 2D piezoelectric materials reported to date. The in-plane piezoelectric strain coefficient d_{11} of SnSe reaching an astonishing 250.58 pm/V, as shown in Figure 1.13 (a). M. Menderes Alyoruk *et al*. [25] discovered that sulfides and oxides based on transition metals Ti, Zr, Sn, and Cr exhibit better piezoelectric effects compared to those based on Mo and W. Subsequently, the exploration of 2D systems with out-of-plane piezoelectric effects has attracted widespread interest. The necessary condition is a crystal structure with non-centrosymmetric characteristics, such as folds or undulations. Because suitable 2D materials is limited, designing and predicting new structures is an effective approach.

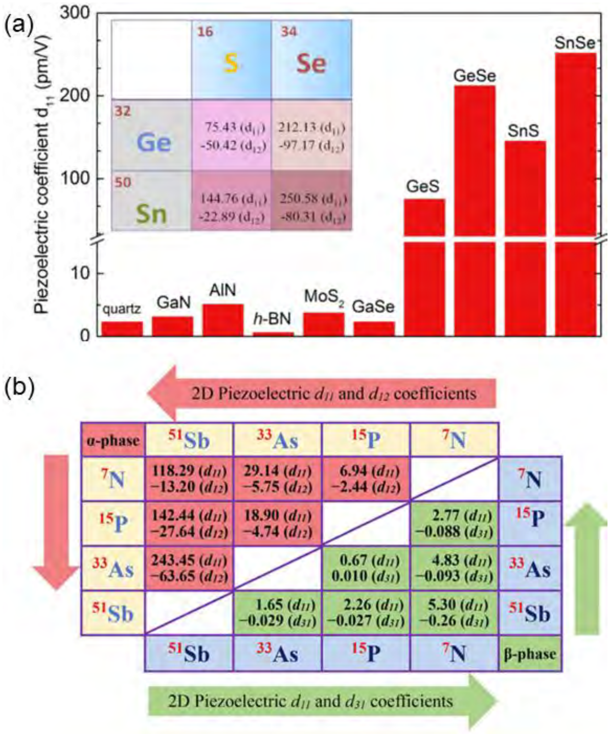

Figure 1.13 (a) Comparison of the piezoelectric coefficient d_{11} between known piezoelectric materials and group IV monochalcogenides [54]. (b) Piezoelectric coefficients of Group-V binary monolayers [55].

In 2017, the piezoelectric effects of 2D honeycomb-like single-layer folded structures of Group III-V elements are investigated [56], which outperforms currently studied 2D materials. Due to the small thickness of the folds, it is easy to achieve a large electric field perpendicular to the surface of the thin sheet experimentally. This is valuable for nano-scale devices (such as relays and FET), while impossible to achieve in bulk materials. Yin *et al.* [55] studied in-plane piezoelectric response in α-phase Group-V binary monolayers (PN, AsN, SbN, AsP, SbP and SbAs), with coefficient d_{11} ranges from 6.94 to 243.45 pm/V. Out-of-plane piezoelectric coefficients d_{31} is also confirmed in β-phase monolayers, e.g., the largest d_{31} is about −0.26 pm/V for β-SbN, as shown in Figure 1.13(b). Subsequently, Zhao *et al.* [57] theoretically designed a series of structures with Janus structures of Group III-V sulfides, as shown in Figure 1.14(a). These systems exhibit considerable in-plane piezoelectric coefficients (1.91-8.47 pm/V), almost four times better than that of perfect structures. Due to the broken mirror symmetry of Janus structure, out-of-plane piezoelectric coefficients (0.07-0.46 pm/V) are induced as well. Chemical modification is also a way to change the symmetry of the structure. For example, H and F-modified pentagonal graphene (PG) are reported to exhibit an out-of-plane piezoelectric stress coefficient e_{31} about 0.97 × 10^{-10} C/m, as shown in Figure 1.14(b) [58].

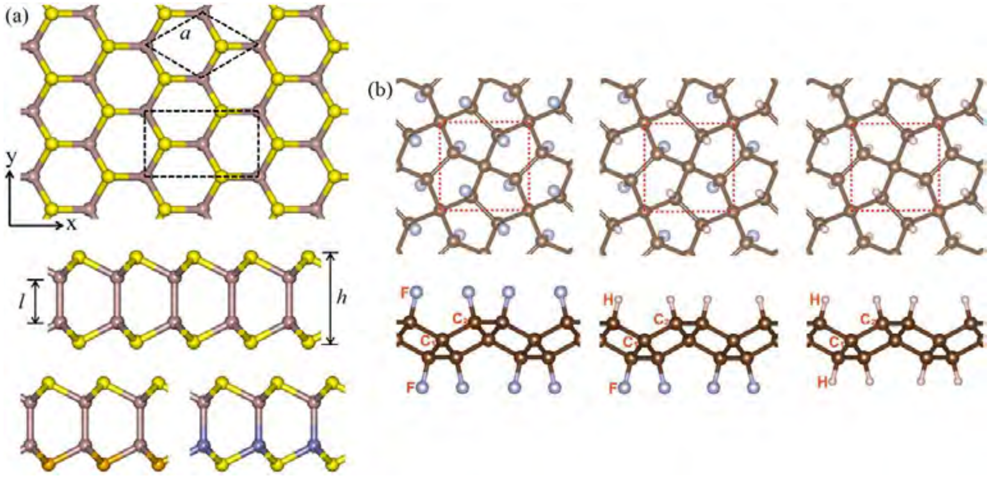

Figure 1.14 (a) Atomic structures of perfect and Janus group-III chalcogenide monolayers [57]. (b) Atomic structure of H and F modified Graphene. [58]

In intrinsic 2D crystals, out-of-plane piezoelectric effects are well investigated in M_2C_3 (M = metal, and C = chalcogen). For example, α-In_2Se_3 possess thickness-dependent d_{33} coefficient about 0.3 pm/V, while increase to 5.6 pm/V at 90 nm thick samples. [59] Interestingly, Bi_2Se_3 and Bi_2Te_3 do not behave piezoelectricity with the same structure. Based on this, Yin *et al.* theoretically design hybrid monolayers of $BiInSe_3$, $BiInTe_3$, $SbInSe_3$, and $SbInTe_3$, which possess the excellent in-plane piezoelectric coefficients as high as 362 pm/V [60].

As a breakthrough, strong out-of-polarization response was reported in bilayer crystals with simple alter of stacking order or twist angle. By transform anti-parallel stacking sequence (AA’ of bulk h-BN) to a parallel AB or BA stacking sequence, the mirror symmetry is broken and thus induce the out-of-plane polarization, as shown in Figure 1.15 [61]. Yasuda *et al*. realized this transformation through a twist between two layers, which is confirmed successfully by piezoforce microscopy (PFM). Vizner Stern *et al*. [62] also identified the polarization reverse by sliding domain wall. Clearly, heterostructures are a developing and hopeful method for achieving tuneable property and abundant performance in 2D fields.

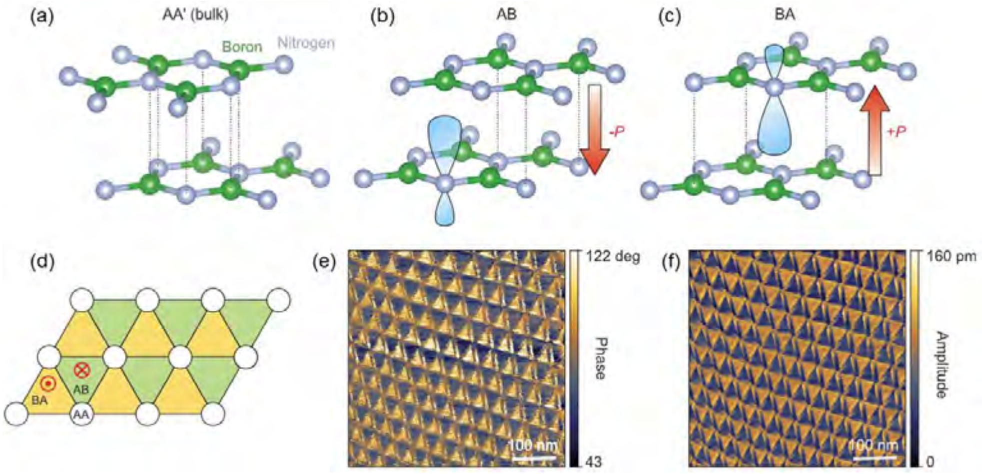

Figure 1.15 Illustration of the atomic arrangement for (a) AA′, (b) AB, and (c) BA stacking. (d) Small-angle twisted bilayer BN after the atomic reconstruction. (e) Vertical PFM phase and (f) amplitude images of twisted bilayer BN.

Piezoelectric properties in 2D materials offer significant prospects for several applications such as pressure sensors, energy harvesters, nanogenerators, etc. By selecting, designing, and integrating the optimal 2D crystals for specific applications, it is expected to achieve the transition between laboratory-scale and practical 2D piezoelectric devices, ultimately enabling large-scale deployment.

1.3 Magnetic property

Magnetism, discovered in ancient times, have attracted immense attention since its technological significance and theoretical complication. It can be used in power generator, information storage, and spintronic devices. The development of high-speed, low-energy information technologies to replace traditional charge-based microelectronic technologies has become an inevitable trend. Magnetism arises as a consequence of nonzero electron spin. According to classical electromagnetism, a current-carrying coil possesses a magnetic moment μ. Similarly, electrons orbiting the atomic nucleus also possess a magnetic moment. The Stern-Gerlach experiment demonstrated the quantized orientation of atoms in a magnetic field. Electrons have a magnetic moment of magnitude 1 Bohr magneton (μ_B), whereas the spin magnetic moment of the atomic nucleus is typically negligible compared to that of electrons. In the presence of unpaired electrons, different magnetic states can be formed. Based on the origin of material magnetism, its variation with temperature, and the magnitude of magnetization, five categories can be distinguished: diamagnetism, paramagnetism, antiferromagnetism, ferrimagnetism, and ferromagnetism, as shown in Figure 1.16 [63].

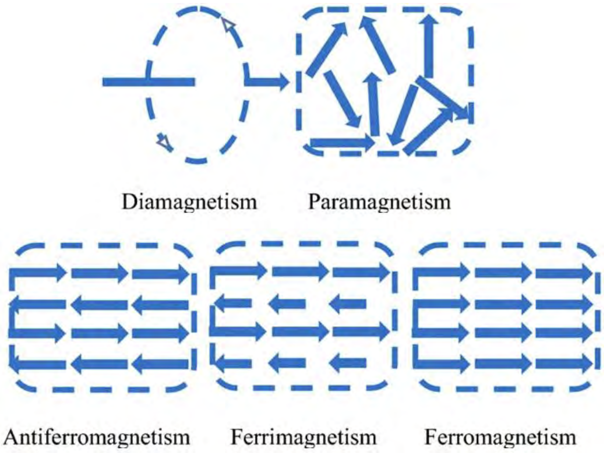

Figure 1.16 Basic magnetic structures of various magnetic materials.

Many free-state atoms possess certain magnetic moments. However, when they combine into molecules and solids, the magnetic moments often vanish in materials with saturated electron structures. There are no intrinsic magnetic moment and materials display diamagnetism. Paramagnetic materials have randomly oriented atomic magnetic moments in the absence of an external magnetic field (due to irregular thermal motion). They cancel each other out, resulting in no macroscopic magnetic moment. Gases such as NO and O_2 exhibit paramagnetism. In antiferromagnetic materials, the magnetic moments of adjacent atoms are antiparallelly aligned. Above the Néel temperature, they exhibit paramagnetism; while below the Néel temperature, the magnetization decreases with decreasing temperature because the enhanced antiferromagnetic interaction. Ferrimagnetic materials have an internal magnetic structure similar to antiferromagnetic materials while magnetic moments arranged unequally. Ferromagnetic materials exhibit ferromagnetism below the Curie temperature, transitioning to paramagnetism above it. The magnetization and temperature of paramagnetic materials follow Curie-Weiss law. The Weiss molecular field theory is a phenomenological theory explaining the microscopic magnetism of ferromagnetic materials [64]. It does not identify the nature of the molecular field and ignores the interaction between local spin magnetic moments, leading to discrepancies with experiments in describing magnetic behaviour near and below the Curie temperature. In 1928, Heisenberg proposed the direct exchange interaction between neighbouring atoms, known as the Heisenberg exchange model. As the participating electrons involved in the exchange interaction are localized near the atoms, it also be called the local electron model [65]. Magnetic materials exhibit distinct response characteristics to external magnetic fields, which can be characterized by hysteresis loops and magnetization curves.

In general, electrons in the s orbitals make no contribution to ferromagnetism. Transition metals and rare earth elements are regarded as sources of magnetism. This is because the electrons occupy partially filled d/f orbitals of these elements. Due to strong Coulomb interactions, these electrons spontaneously form localized magnetic moments according to quantum mechanical rules. Macroscopic magnetic order arises through spin interactions such as direct coupling, superexchange, or double exchange. In metallic magnetic materials, atomic magnetic moments are non-integer, exhibiting significant deviation from the magnetic moment of free atoms. This is attributed to the highly localized nature of d/f electrons. The exchange interactions between electrons lead to the splitting of spin degeneracy in electron bands, resulting in an asymmetric band structure and the formation of uncompensated spontaneous magnetic moments. Due to the static magnetic energy generated by spontaneous magnetization, magnetic domains form within ferromagnetic materials. The spontaneous magnetization direction of magnetic domains typically aligns along the easy magnetization direction of crystal, while the easy magnetization direction of iron aligned along the cubic axis of the crystal. In 2004, Coey *et al*. reported the first room-temperature insulating ferromagnetic material without partially occupied d/f orbitals: HfO_2 thin film [42]. They employed pulsed laser deposition technology and found that the prepared oxygen-deficient HfO_2 thin film exhibited ferromagnetism at room temperature, as shown in Figure 1.17.

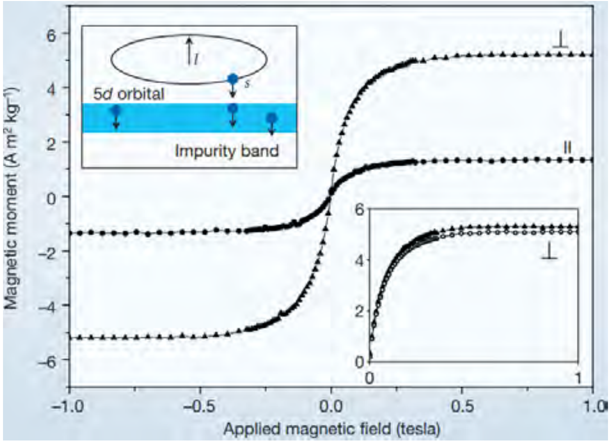

Figure 1.17 Magnetization curves for a thin film of hafnium dioxide [42].

In recent years, spintronics devices, which utilize electron spin and its associated magnetic moments, have significant applications in quantum computing and next-generation information technologies. For a long time, 2D magnetism has been at the forefront of many theoretical, experimental, and technological advancements. It was proposed over 150 years, namely, the layered materials with ferromagnetic or antiferromagnetic ground state under finite temperature [66]. Its emergence presents novel prospects for forthcoming applications in magnetoelectronics and magneto-optics. From the view of theoretical, exchange interaction and spin-orbit coupling were proposed to interpret the inner mechanism, including the origin of spin, orbital moment, and magnetic anisotropy. Since the appearance of graphene, there are many investigations devoted to develop the novel 2D magnetism. According to Mermin-Wagner theorem [67], 2D long-range magnetic order cannot maintain in the condition of $T > 0$, which is limited by its instability originating from short-range interaction and weak anisotropy.

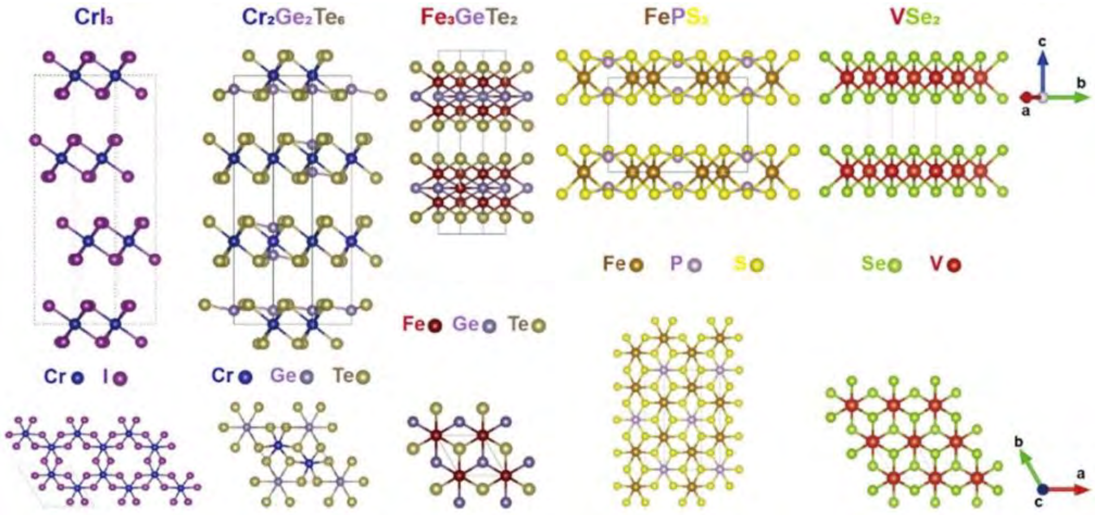

Figure 1.18 The side view and top view of five magnetic 2D materials: CrI_3, $Cr_2Ge_2Te_6$, Fe_3GeTe_2, $FePS_3$ and VSe_2 [68].

Following persistent endeavours, a handful of 2D magnets are actually synthesized through experimental processes. Bulk chromium trihalides CrX_3 (X is a halogen element) is a class of layered material (Figure 1.18). Zhang *et al*. [69] indicated that the estimated exfoliation energy of CrX_3 monolayer is even smaller than that of graphene, which can be obtained through mechanical exfoliation. First-principles calculation results demonstrate their ferromagnetism and semiconductor. Suitable bandgap, as well as absorption edge falls within the visible light spectrum, rendering them intriguing for optoelectronic devices. Moreover, CrI_3 monolayer exhibits a Curie temperature estimated to be as high as 95 K and can be further enhanced through external tuning. Subsequently, these properties have been experimentally confirmed [70-72]. Huang *et al*. employed a mechanical exfoliation method to isolate monolayer CrI_3 from bulk CrI_3 (Figure 1.19), achieving a thickness of approximately 0.6 nm. In their study, the layer number or thickness of CrI_3 was distinguished based on its transparency. They utilized magneto-optical Kerr effect microscopy to demonstrate that monolayer CrI_3 is an Ising ferromagnet with in-plane spin orientation. The Curie temperature is 45 K, slightly lower than that of bulk (61 K). Weak interlayer coupling can explain this result. This discovery represents the first confirmation of macroscopic spontaneous magnetization in a 2D system, marking a milestone breakthrough in decades-long research on 2D ferromagnetism.

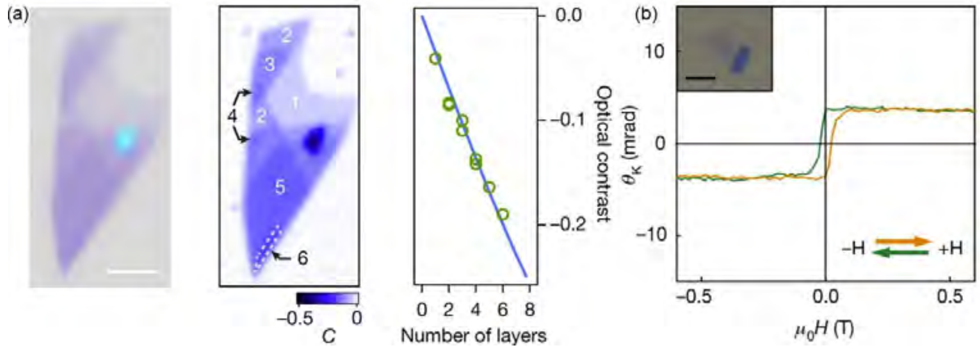

Figure 1.19 (a) Micrograph of a representative CrI_3 flake. (b) Hysteresis loop of CrI_3 monolayer.

Besides, Yang *et al*. [73] theoretically predicted the ferromagnetism of $CrGeTe_3$ monolayer. They highlighted that bulk $CrXTe_3$ is a layered crystal with interlayer vdW gaps. Their lower exfoliation energy directly demonstrating the viability of exfoliation in experiment. Additionally, they noted that $CrXTe_3$ nanosheets are 2D ferromagnetic semiconductors with estimated Curie temperatures of 35.7 K and 57.2 K, respectively. Later, few-layer $CrGeTe_3$ was successfully obtained from their layered bulk structure, paves the way for the implementation of 2D spintronics at the nanoscale [74]. In 3D systems, the Curie temperature primarily relate to the strength of exchange interaction. In 2D systems, anisotropy energy becomes paramount in maintaining magnetic order. Hence, external magnetic fields appear to serve as effective sources of anisotropy for 2D $Cr_2Ge_2Te_6$. Xu *et al.* conducted a comprehensive investigation into the origin of anisotropy in magnetic 2D materials. They found that anisotropy predominantly arises from anisotropic exchange (Kitaev interaction) in CrI_3, whereas mainly stems from single-ion anisotropy in $Cr_2Ge_2Te_6$ [75]. The differential mechanism may explain the sensitivity of the Curie temperature of 2D $Cr_2Ge_2Te_6$ to small external magnetic fields. As for Fe_3GeTe_2, its metallic nature confers it itinerant ferromagnetism and a slightly elevated Curie temperature [76]. In 2016, Zhuang *et al.* [77] demonstrate that monolayer Fe_3GeTe_2 is a potential 2D ferromagnetic metal using first-principles calculations, which was successfully synthesized by two different experimental groups subsequently [78, 79]. They report that the Curie temperature of 2D Fe_3GeTe_2 can reach 180-220 K in the layer number range of 2-6 while decrease to 130 K in monolayer, as shown in Figure 1.20.

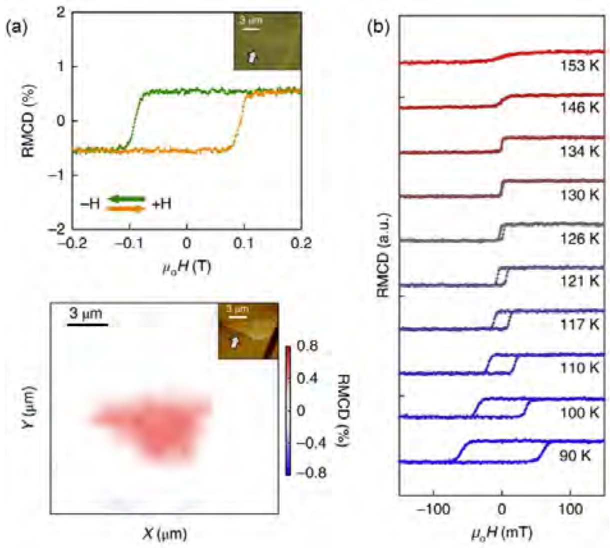

Figure 1.20 (a) Hysteresis loop and of 2D Fe_3GeTe_2 at 78K. (b) The relationship between Curie temperature and hysteresis loop [79].

Compared to ferromagnetic materials, the applications of antiferromagnetic materials are limited. They can be utilized for stabilizing spin valves or serving as fixed layer for magnetic tunnel junction. Although the use of antiferromagnetic materials is restricted due to the disappearance of net magnetic moment, they hold talented prospects for high-speed, low-power spintronic devices. Additionally, antiferromagnetic materials offer richer diversity compared to ferromagnetic materials. MPX_3 (where M can be V, Mn, Fe, Ni, etc., and X can be S, Se) represents a class of antiferromagnetic semiconductors with various magnetic configurations [80]. For $FePS_3$, each Fe^{2+} is ferromagnetically coupled with nearest neighbours while adjacent interplanars are anti-ferromagnetic coupling. Lee demonstrated the Ising-type antiferromagnetic ordering in $FePS_3$ monolayer by monitoring the Raman peaks, which have been of interest [81]. Wang *et al.* reported that Néel temperature decreases from 117 K (bulk) to 104 K (monolayer) since spin-phonon coupling [82]. Meanwhile, the properties of 2D $FePS_3$ seemly maintain unchanged with layer number from 1 to 10, which is quite different from most experimental and theoretical reports of other magnetic 2D materials.

2H and 1T-phase VS_2 and VSe_2 monolayers was predicted to exhibit magnetic ordering, which can be influenced by strain and thickness [83, 84]. However, the issue of chemical stability hinders their experimental verification. Until recently, Batzill *et al.* successfully obtained single-layer and multi-layer 1T-phase VSe_2 with substrates (graphite or MoS_2) by molecular beam epitaxy (MBE) techniques, see Figure 1.21. The magnetization-field (M-H) hysteresis loop clearly demonstrates the ferromagnetic order of 1T-phase VSe_2. They also found that the magnetic moment in single-layer VSe_2 is significantly enhanced compared to multi-layer counterparts. Interestingly, robust ferromagnetic order can persist above room temperature (up to 330 K) in VSe_2/VDW samples. This is confirmed by temperature dependence of saturation magnetization and coercive field, providing a podium for vdW spintronic devices [85]. However, it can only stabilize on some substrates. On monolayer VS_2 grown on MoS_2 substrates, there exists an anomalously high magnetic moment as well as observable in-plane anisotropy. Without strong in-plane uniaxial anisotropy, it is difficult to maintain long range ferromagnetic order at room temperature.

Although rapid development of 2D magnetic materials, the relatively low ferromagnetic Curie temperatures greatly restricting their applications at room temperature. To diversify more type of 2D magnetic materials and further expand their applications, a battery of researches has been conducted on how to induce magnetization in 2D non-magnetic materials.

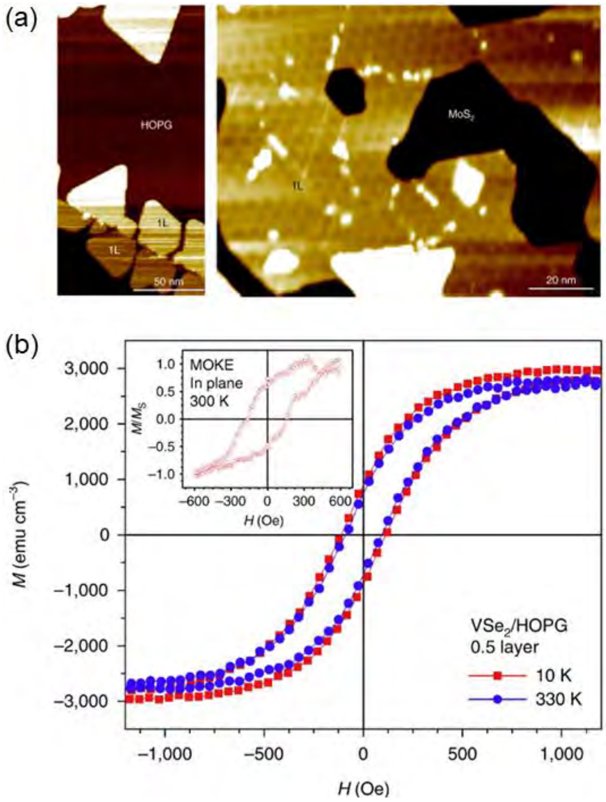

Figure 1.21 (a) VSe_2 monolayer grown on graphite and MoS_2. (b) M–H hysteresis loops of VSe_2 taken at 10 and 330 K [85].

Currently, methods for realizing magnetism in non-magnetic materials include defects, adsorption, doping, magnetic proximity effects, functional group modification, band engineering and so on. However, the induced magnetism through above methods is often weak and difficult to control experimentally. Moreover, these methods may obscure or disrupt the intrinsic physical properties of materials, such as symmetry and semiconductor characteristics [86]. These methods fail to ensure the stability of magnetic devices, thus limiting their application in information storage. In-depth studies on electronic property of 2D systems have revealed the existence of Van Hove singularities when the material exhibits Mexican-hat band edges near Fermi level, see

Figure 1.22 [87]. Electrons located at Van Hove singularities near the Fermi level are prone to be unstable, leading to novel phenomena such as magnetism and superconductivity. Cao *et al*. theoretically demonstrated that magnetism can be induced by doping holes in single-layer GaSe [88]. As doping holes can elevate the energy of Fermi level, the system transforms into a semimetal at a certain doping concentration. Liu *et al*. achieved ferromagnetic ferroelectric coupling by doping a certain concentration of holes in the ferroelectric material In_2Se_3 [89]. Additionally, Miao *et al*. demonstrated magnetism by doping electrons in single-layer InP_3 [90]. Therefore, magnetism induced by doping carriers not only enables higher Curie temperatures and enhanced magnetic stability but also allows for quantitative control of the dopant carrier concentration. Importantly, this method ensures the integrity of the 2D structure without affecting its intrinsic physicochemical properties. The key to this method lies in finding materials with relatively flat bands near the Fermi level.

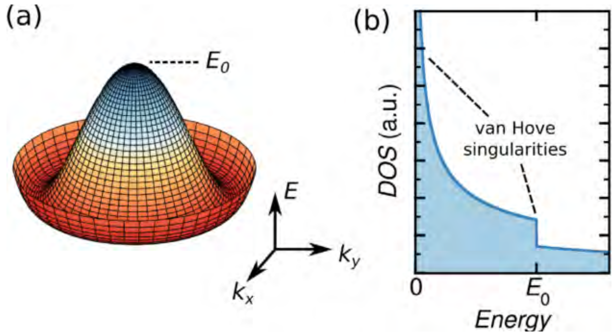

Figure 1.22 Schematic illustration of (a) Mexican-hat band edge model and (b) density of states of Van Hove singularities.

From a theoretical perspective, carrier doping induced dispersion relation for spin-up and spin-down electrons can be expressed by Stoner model [77]. In this model, the existence of Coulomb repulsion makes a struggle between kinetic energy and exchange energy. The energy of spin with different states could split through the exchange interaction. The construction of spin splitting results in the energy changes. When the relative gain in exchange interaction is larger than the cost of kinetic energy, the potential energy would decrease. These changes of total energy create the probability to satisfy the Stoner criterion ($D(E_F) \times I > 1$, where $D(E_F)$ is the density of states at Fermi level, I is strength of exchange interaction), leading to itinerant ferromagnetism. Due to the nature of itinerant electrons, this model is adopted to demonstrate the derivation of spontaneous ferromagnetism in several 2D magnetic metals, such as Fe_3GeTe_2 [77], TMDs [91], MXene [92], as well as a variety of charge doped 2D materials [88, 93, 94]. A plenty of these studied 2D metal magnetism possesses extraordinarily high Curie temperatures.

1.4 Janus structure

Generally, the electronic characteristics of materials are largely determined by their crystal structure, especially symmetry. The broken symmetry could result in novel properties, such as ferromagnetism, ferroelectricity, and phase transition. The Janus structure is an asymmetric structure that can be either natural or synthesized by design. Its name comes from a Roman God who presents two dissimilar faces. This particular construction brings distinct properties to 2D materials, such as piezoelectricity, photoelectricity, and Rashba splitting effect [95, 96].

With the development of graphene and graphene derivatives, a novel asymmetric functionalized graphene structure has been defined as Janus graphene. Graphone is earliest studied one, gained by substituting partial H atom layer in H-graphene. It behaves ferromagnetism with a small bandgap [97]. In 2011, Singh and Bester theoretically predicted a stable hydrofluorinated graphene [98]. By hydrogenation and fluorination on both sides of the graphene, an asymmetric stable structure is obtained. Unlike conventional graphene, the HFC-1 structure has an electronic bandgap with a value of about 3.34 e V. Mitchell *et al*. studied the piezoelectricity of graphene-based Janus materials [46]. Because it is difficult to obtain in nature, this type of structure can be realized experimentally by surface covalent functionalization [99].

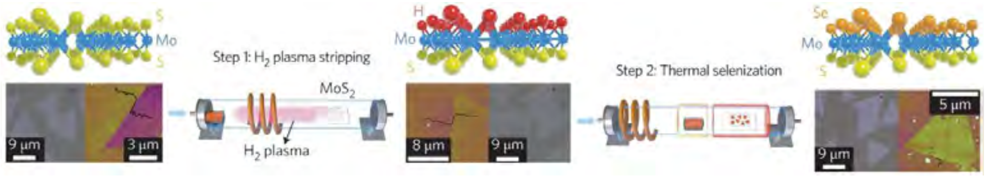

Figure 1.23 Synthesis process and optical microscopy and atomic force microscopy images for each structure [100].

Beyond the modified graphene, Janus TMDs is a typical 2D Janus system. It breaks the out-of-plane symmetry of perfect structure, causing a series of unique physical phenomena. Cheng et al. used ab initio method to study electronic property of stable Janus MXY (M=Mo, W; X, Y=S, Se, Te) monolayers [101]. Relative to perfect MX_2, there is broken mirror symmetry of Janus MXY. This leads to Rashba splitting at highest Γ point of valence band and corresponding piezoelectric response. Later, Janus MoSSe monolayer was obtained by the vulcanization growth method on the upper surface, as shown in Figure 1.23 [100]. They directly confirmed the existence of the Janus MoSSe structure by scanning transmission electron microscopy and energy-dependent X-ray photoelectron spectroscopy. Dong *et al*. studied 2D Janus MXY semiconductor and obtained their piezoelectric coefficient value using modern polarization theory as well. The results show that monolayers have enhanced in-plane piezoelectric effect (d_{11}=2.26 ~ 5.30 pm V^{-1}) and weak out-of-plane piezoelectric effect (d_{31}=0.007 ~ 0.030 pm V^{-1}). For multilayers, large out-of-plane piezoelectric polarization increase up to 5.7 ~ 13.5 pm V^{-1}, which can be compared to bulk piezoelectric AlN [102]. In 2017, Guo *et al.* constructed a group of Janus models on the basis of MX single layer with two types M_2XX' and $MM'X_2$. Compared with that of MX monolayer, the bandgap of Janus structure decreases and in-plane piezoelectric effect significantly enhances (almost four times greater than that of the perfect MX monolayer) [57]. Moreover, good light absorption, combined with electron hole pairs, makes Janus materials also useful for photocatalytic applications [103]. In addition to the existing perfect 2D materials, Janus systems can offer more possibilities and bringing excellent properties to adapt to the requirement of modern electronics.

1.5 Motivation and objectives

Although conventional 2D materials, as mentioned above, possess a series of outstanding properties, some drawbacks limit their applications as well. For example, zero bandgap of graphene is not suitable to be applied in photoelectric fields; BP cannot maintain its chemical stability in ambient surroundings; MoS_2 monolayer has low carrier mobility; and it is hard to realize the mass production of h-BN. Because of the rapid development of modern device integration and miniaturization, there is an urgent requirement to explore the novel materials to expand 2D family and investigate their promising properties in applications.

For the electrical and magnetic applications of 2D materials, several challenges are currently prominent:

1) Over the years, semiconductor materials experienced several generations. Their bandgap tends to become wider. For Ga_2O_3, its bandgap reaches 4.8 eV. With continued miniaturization of devices, the technological sizes and performance of bulk semiconductor have approached their physical limits. At post-Moore era, atomic-scale materials are very important for future integrated circuits and scaling transistors. However, there is a scarcity of 2D wide-bandgap materials with bandgaps greater than 2.5 eV. The wide-bandgap materials could sustain higher electric breakdown field. Besides, they possess higher thermal conductivity and electron saturation rates, allowing potentials for high-voltage, high-temperature, and high-power electronics. Since large bandgaps typically imply higher electron mobility and lower carrier recombination rates, thereby contributing to enhanced device performance and efficiency. However, due to the rarity of wide-bandgap materials and the challenges associated with their synthesis and property modulation, there remain numerous research and engineering obstacles. Consequently, the discovery of novel 2D wide-bandgap materials and the exploration of their property modulation and potential applications are of paramount importance in driving the advancement of electronic and optoelectronic devices.

2) The energy density of thin-film dielectric materials is still an order of magnitude lower than those of electrochemical supercapacitors and batteries, which constrains

their practical applications in energy storage. Despite these materials with a high specific surface area and tunable electrical properties, their energy density is often limited by the presence of nanoscale structures and interlayer gaps. Therefore, improving the energy density of 2D dielectric materials is currently a focus of research, which involve the optimization in selecting dielectric materials with enhanced energy storage capacity and efficiency.

3) Curie temperature is a critical temperature at which a material transforms from ferromagnetic to paramagnetic states in the absence of an external magnetic field. Due to the nano-scale and surface effects inherent in 2D materials, they often exhibit lower Curie temperatures compared to their 3D counterparts, implying that 2D magnetic materials may lose their magnetism at ambient temperatures and thereby limit their stability and reliability in practical devices. Among numerous 2D materials, intrinsic 2D magnetic materials are currently scarce. Theoretical simulations can provide us with a deeper understanding of the magnetic behavior of 2D materials, such as the mechanisms and pathways for enhancing the Curie temperature. For instance, introducing magnetism by carrier doping in 2D non-magnetic materials is a potential method in enhancing the Curie temperature.

Because of the high cost, extensive lab work, and long duration required for experimental investigations of nanomaterials, theoretical simulations are typically performed prior to experiments for optimization. Furthermore, modern computational techniques supported by advanced supercomputers enable the attainment of simulation results with high accuracy, in comparison to experimental results. Hence, this Ph.D.

study on 2D materials employs first-principles simulations, currently recognized as one of the most efficient and highly predictive computational methods available.

In this Ph.D. thesis, we predict and investigate the structures, electrical and magnetic properties of 2D materials via first-principles simulation. Several novel and potential 2D materials are considered.

The general objectives in this thesis have been set as follows:

1) To develop 2D materials with wide bandgap and investigate its structural stability, electrical properties, including band structure, dielectricity, piezoelectricity, carrier mobility, etc., which can be used for devices with multi-functionality.

2) To realize stable ferromagnetism in 2D nonferromagnetic materials which have special band edges by carrier doping. The Curie temperature of this itinerant ferromagnetism should be estimated. The external influences such as applied strains, layer numbers on electronic and magnetic properties should be considered to understand the underlying mechanisms, which could be applied to enlarge the applications of monolayer in memory and sensors.

3) To evaluate strategies for the construction of 2D Janus materials and high-entropy materials, providing avenues for the manipulation and enhancement of their electronic properties, and exploring their potential applications in nanoelectronics.

The 2D materials investigated in this thesis research are expect to facilitate the achievement of miniaturization, integration, and multi-functionalization of nano-devices. These materials enable the development of compact and efficient electronic components with enhanced performance. Moreover, their unique properties, such as high carrier mobility and tunable band structures, offer unprecedented opportunities for the design and implementation of novel functionalities in various electronic devices. Additionally, the scalability and versatility of 2D materials make them promising candidates for next-generation nanoelectronics, paving the way for the realization of advanced technologies and innovative applications across diverse fields.

Chapter 2 Research methodologies

2.1 Introduction of the first-principles calculation

Based on quantum mechanics, the first principles calculation is a method to solve the Schrodinger equation to obtain Eigen value and Eigen function, and thus the electronic structure. This method is independent of any empirical parameters, which is also its most obvious advantage. To be more specific, only atomic number and crystal structure as input, which can precisely determine the basic structure, physical and chemical properties of real materials. It can be roughly divided into two categories: first principles calculation based on Hartree-Fock self-consistent field, which is mainly used to calculate aperiodic systems; The other is the first principles calculation based on density functional theory (DFT), which is mainly used to calculate periodic systems. Compared with the former, the latter greatly reduces the calculation burden on the premise of ensuring the calculation accuracy. DFT takes charge density as the only variable, and all physical quantities of the system can be obtained by using the functional of charge density. This can not only describe the microscopic electronic properties (such as density of states and interaction between electrons) of the multi-particle system, but also obtain the physical quantities (such as binding energy, conductance, etc.) which characterize the macroscopic properties of the material. With the development of technology, it is widely used in physics, chemistry, biology, material science and other fields. In this chapter, we give a brief description of the basic theory involved in the first principles calculation, the corresponding approximation method and the calculation software package used.

2.2 Multiparticle system schrodinger equation and its solving

As mentioned earlier, quantum mechanics is the basis of first principles calculations. Therefore, the calculation of the basic properties of a study material through first principles is essentially the process of solving the Schrodinger equation of the system. In the multi-particle system, the Schrodinger equation can be expressed as:

$$\hat{H}\Psi = E\Psi \tag{2.1}$$

Where $\hat{H}$ is the total Hamiltonian operator and E is the total energy of the system. $\hat{H}$ includes the kinetic and potential energies of nuclei and electrons, which can be obtained by linear addition of the Hamiltonian of the nucleus, the nucleus and the electron, and the interaction between the electrons.

The properties of the ground-state system can be determined uniquely by the charge density. This is because the relationship between energy and charge density is one-to-one while the mapping between them is uncertain. In theory, as long as the initial state of the system is known, the relationship between system evolution and time can be obtained. For single-electron systems, exact solutions to the equations are easy to be determined. For real systems with many atoms, their wave function, with three times as many variables associated as the total number of electrons and nuclei, is extremely complex. It is impossible to solve the wave function directly in the multi-particle system and thus the Schrodinger equation must be approximated. Reasonable approximations can not only greatly simplify the problem of solving the equation, but also give reliable computational results. The following two approximations are often used in first principles calculations: Born-Oppenheier approximation (adiabatic approximation) and Hartree-Fock approximation (single electron approximation). They will be introduced and discussed in the following sections of this chapter.

2.2.1 The Born-Oppenheier approximation

In electronic structure of real materials, the number of particles per cubic centimeter in the system reach about 10^{23}. They interact with each other, which makes the exact solution of Schrodinger equation very difficult. The Born-Oppenheier approximation [104], also known as the adiabatic approximation, was proposed by Born and Oppenheimer in 1927 to help simplify the above issue. Due to the mass of the nucleus is much larger than that of the electron (1836 times), its velocity is much smaller than that of the electron in the process of movement. It can be considered that the electron moves in the potential field formed by the static nucleus. The nucleus cannot discern the exact position of the high-speed moving electron outside the nucleus and thus receive the average force. The movements of electron and nucleus can be separated as two isolate systems as the huge difference of velocity. In other words, the wave function of the system is separated into the nucleus part and the electron part to be solved separately.

If the external field and relativistic effects are not considered, the Hamiltonian $\hat{H}$ can be expressed in the following form:

$$H = H_e + H_N + H_{e-N} \quad 2.2$$

H_e is the sum of the kinetic energy of the electron and the Coulomb interaction between the electron and the electron, which can be expressed as:

$$H_e = -\sum_i \frac{\hbar^2}{2m_e}\nabla_{r_i}^2 + \frac{1}{2}\sum_{i\neq j}\frac{e^2}{\left|r_i - r_j\right|} \qquad 2.3$$

H_N is the sum of the kinetic energy of the nucleus and the Coulomb interaction between the nucleus, which can be expressed as:

$$H_N = -\sum_i \frac{\hbar^2}{2M_i}\nabla_{R_i}^2 + \frac{1}{2}\sum_{i\neq j} V_N\left(R_i - R_j\right) \qquad 2.4$$

H_{e-N} is the interaction between electrons and nucleus, which can be expressed as:

$$H_{e-N} = -\sum_{i,j} V_{e-N}\left(r_i - R_j\right) \qquad 2.5$$

Under the Born-Oppenheier approximation, the Hamiltonian $\hat{H}$ for a many-particle system has the following form:

$$H = -\sum_i \frac{\hbar^2}{2m_e}\nabla_{r_i}^2 + \frac{1}{2}\sum_{i\neq j}\frac{e^2}{\left|r_i - r_j\right|} - \sum_{i,\mathrm{j}} V_{e-N}\left(r_i - R_j\right) + \frac{1}{2}\sum_{\mathrm{i}\neq\mathrm{j}} V_N\left(R_i - R_j\right) \qquad 2.6$$

Where the nucleus is treated as stationary, and only the terms related to the electron need to be considered. Thus, the interaction between atoms and electrons can be regarded as a constant and the Hamiltonian $\hat{H}$ can be simplified as follows:

$$H = -\sum_i \frac{\hbar^2}{2m_e}\nabla_{r_i}^2 + \frac{1}{2}\sum_{i\neq j}\frac{e^2}{\left|r_i - r_j\right|} - \sum_{i,\mathrm{j}} V_{e-N}\left(r_i - R_j\right) \qquad 2.7$$

The Born-Oppenheier approximation can effectively reduce the difficulty of solving Schrodinger equation with slight error. However, the interactions of electron-electron and electron-nucleus are complicated. It is still unrealistic to solve the wave function for the real materials with a large number of atoms and further simplification and approximation are necessary.

2.2.2 The Hartree-Fock approximation

In 1928, Hartree first proposed the theory of the mean-field approximation [105], that is, the motion of each electron is independent and proceeds in the mean-field generated by all other particles. The motion of a single electron is uniquely determined by its average electron density and independent of the position of other electrons. The electron-electron interaction can be viewed as a Coulomb force, which simplify the multi-electron problem to single-electron problem. Based on this approximation, the total wave function of the multi-electron system can be composed of the product of the single-electron wave functions as follows:

$$\phi(r)=\varphi_1(r_1)\varphi_2(r_2)\ldots\varphi_n(r_n) \qquad 2.8$$

Where $\phi(r)$ is the total wave function of the system, φ_n (n=1, 2, 3 ……) is the wave function of each electron. In this case, the one-electron equation (namely Hartree equation) can be obtained using the variational principle and expressed as:

$$\left[-\frac{\hbar^2}{2m_e}\nabla_{r_i}^2-\sum_i V_{e-N}\left(r_i-R_j\right)+\sum_{j(i\neq j)}\int dr'\,\frac{e^2}{r-r'}\left|\phi_j\left(r'\right)\right|^2\right]\phi_i(r)=\varepsilon_i\phi_i(r) \qquad 2.9$$

The last term on the left of the equal sign is the average potential, that is, the single electron with the position vector r_i is subjected to the mean field action of other electrons. Because electrons are fermions, Fermi distribution statistics and Pauli exclusion principle need to be satisfied. However, the sign of wave function will not change after electron exchange position in Hartree approximation. This violates the antisymmetry principle of electron exchange. For solving this issue, Fock reformulated the wave function of the multi-electron system in terms of the Slater determinant as

[106]:

$$\phi = \frac{1}{\sqrt{N!}} \begin{vmatrix} \varphi_1(r_1) & \varphi_2(r_1) & \cdots & \varphi_N(r_1) \\ \varphi_1(r_2) & \varphi_2(r_2) & \cdots & \varphi_N(r_2) \\ \cdots & \cdots & \cdots & \cdots \\ \varphi_1(r_N) & \varphi_2(r_N) & \cdots & \varphi_N(r_N) \end{vmatrix} \qquad 2.10$$

After variational treatment, the Hartree-Fock equation of the system becomes:

$$\left[-\frac{\hbar^2}{2m_e}\nabla_{r_i}^2 + V(r) + \sum_{i'(i\neq i')}\int\frac{\left|\varphi_{i'}\left(r'\right)\right|^2}{\left|r'-r\right|}dr' - \sum_{i'(i\neq i')}\int\frac{\varphi_{i'}^{*}\left(r'\right)\varphi_{i'}\left(r'\right)}{\left|r'-r\right|}dr'\right]\varphi_i(r) = \sum_i \varepsilon_i\varphi_i(r)$$

2.11

It should be noted that the Hartree-Fock approximation only explains the exchange between spin parallel electrons, and lacks the consideration of the repulsion between spin antiparallel electrons.

2.3 Density functional theory

Although the above two approximations have effectively reduced the complexity of solving the Schrodinger equation, it is still difficult to obtain the exact solution when the number of electrons increases. This is because an electron has three degrees of freedom in space. When the wave function is regarded as variables, the problem becomes a 3n-dimensional problem and the difficulty increases exponentially. Compared with the complex wave function, the introduction of electron density simplifies it to 3D equations, which is easy calculated. Thus, Hohenberg and Kohn put forward the universal density functional theory in 1964 [107]. Its basic idea is to describe the properties of materials by replacing wave function with electron density, the only variable. This is also the key to the first principles approach, which provides a set of methods to transform the multi-electron problem into a self-consistent field single-particle problem with ground state properties. The core of the theory is the Hohenberg-Kohn theory and the Kohn-Sham equation, which are described below.

2.3.1 Hohenberg-Kohn theory

In 1964, Hohenberg and Kohn proved H-K theory [107] (inhomogeneous electron gas theory) in a concise way, which laid the foundation of DFT. In these two important theories, the complex problem between interacting electrons is simplified to a single-electron problem in the mean field, which is only dependent on the electron density.

Theorem 1 can be stated as follows: For a multi-particle system, the energy of its ground state is the only functional of the particle density distribution function ρ(r) (density for short).

It can be seen that the electron density can determine the Hamiltonian of the system. It is not necessary to get the wave function of each particle. The related properties of the system can be studied only according to the electron density of the ground state, which confirms the existence of a unique density distribution function ρ(r).

Theorem 2 can be stated as follows: If is the true and correct ground state electron density ρ(r), the obtained energy must be the minimum, that is, the ground state energy.

According to the above two theorems, the Hamiltonian and eigenvalue of the system can be expressed as follows:

$$\hat{H} = -\frac{\hbar^2}{2m_e}\sum_i \nabla_{n_i}^2 + V_{\text{ext}}(\mathbf{r}) + \frac{1}{2}\sum_{i \neq i'} \frac{e^2}{|\mathbf{r} - \mathbf{r}'|} \qquad 2.12$$

$$E[\rho(\mathbf{r})] = T[\rho(\mathbf{r})] + U[\rho(\mathbf{r})] + E_{xc}[\rho(\mathbf{r})] \qquad 2.13$$

where the right side of the equal sign is the kinetic energy functional of the system, the Coulomb repulsive interaction functional between electrons, and the exchange correlation functional in turn. The above theorems have been proved in the literature [107-110]. Although H-K theorem gives the concept of density functional theory, it is not mentioned about how to create density functional. The key is to know the specific form of electron density function and the determination of the sum of $T[\rho(\mathbf{r})]$ and $U[\rho(\mathbf{r})]$.

2.3.2 Kohn-Sham equation

In order to solve the above difficulties, Kohn and Sham proposed the method of "energy decomposition, divide and conquer" in 1965.[108] In other words, the kinetic energy and potential energy of particles without interaction are separated while the remaining part is approximated. All errors between the approximation and the true value are included in the exchange correlation functional. Supposing that the electrons in the system have no interaction with each other, and that this system has the same electron cloud distribution as the system with interacting electrons, the density function is composed of n single-electron wave functions and can be expressed as:

$$\rho(\mathbf{r}) = \sum_{i=1}^{N} |\varphi_i(\mathbf{r})|^2 \qquad 2.14$$

The kinetic energy functional and potential energy functional of the system can be written as follows:

$$T_{\mathrm{S}}[\rho(\mathbf{r})]=-\frac{\hbar^2}{2m_e}\sum_i\int d^3\mathbf{r}\varphi_i^*(\mathbf{r})\nabla^2\varphi_i(\mathbf{r}) \qquad 2.15$$

$$U_{\mathrm{S}}[\rho(\mathbf{r})]=U_H=\frac{1}{2}\int d^3\mathbf{r}d^3\mathbf{r}'\frac{\rho(\mathbf{r})\rho\left(\mathbf{r}'\right)}{\left|\mathbf{r}-\mathbf{r}'\right|} \qquad 2.16$$

Therefore, exchange correlation effect is the sum of kinetic energy difference and potential energy difference of electronic system with or without interaction, namely:

$$E_{\mathrm{XC}}=T-T_{\mathrm{S}}+U-U_{\mathrm{S}} \qquad 2.17$$

The Kohn-Sham equation is obtained by variating the energy functional to the electron density, which can be expressed as:

$$\left[-\frac{h^2}{2m}\nabla^2+V(r)+V_H(r)+V_{XC}(r)\right]\psi_i(r)=\varepsilon_i\psi_i(r) \qquad 2.18$$

In this way, the Schrodinger equation of complex multi-particle system is transformed into the solution of a single electron problem. First, an initial electron density is defined to solve the K-S equation. Next, the wave function of a single electron is obtained, which can be used to calculate the new electron density. Finally, the exact ground state energy and related properties of the system can be obtained after several iterations.

2.4 Exchange correlation functional

In the solution of the K-S equation, the exchange correlation term must be known. This term includes all the interactions of the system and its exact value is difficult to be obtained. This shows that the determination of the exchange correlation functional has a decisive impact on the accuracy of the density functional. Thus, the specific form of exchange correlation functional must be obtained. The further approximation is necessary.

2.4.1 Local-density approximation

In 1965, Kohn and Sham proposed the Local Density approximation (LDA) method to deal with the exchange correlation functional[108]. In this approximation, the inhomogeneous electron gas is divided into many small volume units dr. The electron gas density in each unit is ρ(r). Supposing that there are no interactions between the electron gases in each unit, the exchange relation of the system can be expressed in the following form:

$$E_{xc}^{LDA}[\rho(\mathbf{r})] = \int d^3\mathbf{r}\rho(\mathbf{r})\varepsilon_{xc}[\rho(\mathbf{r})] \qquad 2.19$$

Therefore, the exchange correlation term in the K-S equation can be written as:

$$V_{xc}[\rho(\mathbf{r})] = \frac{\delta E_{xc}^{LDA}[\rho(\mathbf{r})]}{\delta\rho(\mathbf{r})} = \varepsilon_{xc}[\rho(\mathbf{r})] + \rho(\mathbf{r})\frac{\delta\varepsilon_{xc}[\rho(\mathbf{r})]}{\delta\rho(\mathbf{r})} \qquad 2.20$$

In the system where the charge density changes slowly, LDA can obtain relatively accurate results. In the system where the charge density changes greatly, it is not appliable. There are some defects with the LDA. For example, the charge density of non-uniform system cannot be expressed accurately and the calculation error in strong correlation system is more appropriate.

2.4.2 Generalized Gradient Approximation

In practice, the distribution of electron density in most systems is not uniform in space and has the property of dispersion. In order to improve the accuracy of calculation, the functional with gradient distribution of electron density is introduced into the exchange correlation functional, which is the generalized gradient approximation (GGA) [111, 112]. In this approximation, the exchange correlation functional in the system not only depends on the electron density, but also considers the effect of the electron density gradient, which can be expressed as:

$$E_{xc}^{GGA}[\rho(\mathbf{r})] = \int d^3\mathbf{r}\rho(\mathbf{r})\varepsilon_{xc}[\rho(\mathbf{r}), \nabla\rho(\mathbf{r})|] \qquad 2.21$$

There are some GGA functional forms used commonly, including Perdew-Burke-Ernzerhof (PBE) [113], Perdew-Wang (PW91) [114], and Becke-Lee-Yang-Parr (BLYP) [115]. In general, GGA functional can give more accurate calculation results than LDA in solid materials with inhomogeneous electron gas.

2.4.3 Hybrid density functional

At present, LDA and GGA are the two most commonly used exchange correlation functions. In most cases, they are effective to obtain ideal results. With the demand of high-precision results, a new hybrid density functional was proposed through in-depth exploration. This functional considers both the approximate term of exchange in DFT and the exact term of exchange in Hartree-Fock. They are combined linearly and the proportion of each part can be adjusted by changing the combination coefficient. The general expression can be written as:

$$E_{xc} = (1-a)E_{xc}^{\mathrm{DFT}} + aE_{x}^{\mathrm{HF}} \qquad 2.22$$

HSE06 is the most commonly used hybrid density functional [116]. In the calculation of the band gap of semiconductor systems, LDA and GGA usually underestimate the size of the band gap while the hybrid density functional can give a more accurate result [117]. It is to be noted that the hybrid density functional is not suitable for the simulation of large systems considering the consumption of computing resources.

2.5 The First Principles simulation packages

2.5.1 Vienna Ab-initio Simulation Package (VASP)

In the above content, we give a brief introduction to density functional theory. Self-consistent iterative calculation is needed to solve the ground state energy. For complex large systems, multiple iterations are necessary, which requires a large amount of calculation. In addition to high performance computers, software packages based on density functional theory calculations are essential. The calculation in this report adopts Vienna Ab-initio Simulation Package (VASP) [118, 119], which is the most widely used first-principles software in the field of computational science. Projected Augmented Wave (PAW) self-consistent iteration is adopted to solve the Schrodinger equation. This method can obtain the ground state energy and related physical quantities of the system. The system with hundreds of atoms can be simulated with high parallel efficiency, and the predicted results are consistent with the experiment. In the process of calculation, major input files need to be set up, including INCAR (to determine the main content of calculation by setting important parameters), KPOINTS (the selection of K points in Brillouin region), POSCAR (a structural file describing the position of atoms in the system), POTCAR (the pseudopotentients corresponding to each element in the system). Cooperate with the script of submission, multiple output files can be obtained. After data analysis of these files, various properties of the system can be determined, such as mechanics, heat, optics, electricity, etc.

2.5.2 Phonopy

Phonopy is a software package developed by Atsushi Togo in Japan using python language [120]. Its core function is to calculate the phonon spectrum of materials and analyse crystal structure from phonon characteristic. There are two commonly used methods to obtain phonon spectrum. One is finite displacement method: multiple supercells are constructed by atomic displacement on the basis of the protocell, and then the force information is processed. To some extent, this method requires higher computing resources. The other is the density functional perturbation theory (DFPT) method: using the symmetry of the structure to generate all the unequal displacements of the structure. Compared with former, this method can save the calculation cost. By running Phonopy in VASP, information such as phonon spectrum and phonon state density of materials can be easily obtained through the above two methods.

Chapter 3 2D Gallium oxychloride (GaOCl)

3.1 Introduction

Since graphene was successful exfoliated in 2004, the family of 2D (2D) nanomaterials have been rapidly expanded [2]. With excellent physical and chemical properties which are remarkably different from their bulk counterparts, a series of 2D layered materials have been explored, including BP [121], h-BN [122, 123], and TMDs [124]. Owing to their extraordinary potentials for optical, mechanical and electronic applications, 2D materials have aroused a lot of interest that experimental and theoretical studies are devoted to exploring novel 2D systems with excellent properties [125-128].

The semiconductors with a wide bandgap, such as GaN and SiC, offer an extended functionality of both electronics and optoelectronics, and have been successfully industrialized. With the demand for detecting blue and ultraviolet light in a wide range of civil and military applications, such as light-emitting diodes, biological analysis, flame detection, etc., 2D materials with a wide bandgap typically exceeding 3 eV have attracted particular attention. On the other hand, the large energy separation between conduction and valence bands allow the semiconducting device to potentially operate at high temperatures and voltages [129]. Although wide-bandgap bulks h-BN (5.9 eV) [130], AlN (6.2 eV) [131], and β-Ga_2O_3 (4.85 eV) [132] have been explored extensively, most 2D materials discovered to date possess a relatively narrow bandgap, and it is a challenge in searching for novel wide-bandgap 2D materials.

In addition, the majority of existing 2D materials are intrinsically nonmagnetic, which could restrict the improvement of performance of next-generation field-effect transistors and nonvolatile memory. Particularly, it is still challenging to control or utilize the 2D ferromagnetisms at room temperature. Notwithstanding, a flat band edge could lead to a sharp van Hove singularity in the density of states (DOS) of 2D materials, providing a feasibility that the ferromagnetism can be induced in a nonmagnetic system. For example, group-III monochalcogenides (GaS, GaSe, and InSe) [88, 133, 134], group-IV monoxides (SnO and PbO) [87, 135, 136], and SnX_2 (X = S and Se) [137] were predicted to exhibit the carrier doping-induced ferromagnetism. However, such ferromagnetism occurs merely either with a limited doping concentration or high trigger-density of carriers. Thus, 2D systems with room-temperature stability and moderate carrier density are preferable for the occurrence of doping-induced ferromagnetisms.

Piezoelectric materials allow for the energy conversion between electrical and mechanical energies, which have been widely used in sensors, actuators, and energy harvesters. Due to the broken centrosymmetry caused by the reduction in their dimensions, 2D materials such as group IV monochalcogenides (SnSe/SnS and GeSe/GeS [54], ABX_2P_6 family [138], group-V binary compounds (α-SbN, α-SbP, and α-SbAs) [55], III–V semiconductor [139], and a series of Janus systems [57, 140, 141], could exhibit piezoelectricity. Unfortunately, most of 2D materials only exhibit in-plane piezoelectricity, which are restricted to be used under bending condition in a functional device. Hence, 2D systems with multidirectional piezoelectricity that the applied strain in one direction would produce polarization changes in multiple directions are more desirable and valuable for practical applications.

In this work, a novel 2D GaOCl monolayer is explored on the basis of first-principles calculations. With a low cleavage energy, it is feasible to exfoliate it from 3D bulk and its dynamical and thermodynamic stability are confirmed. Its bandgap is as large as 4.46 eV, which can be tuned by the externally applied strain. Besides, the carrier mobility is calculated to evaluate the transport property, and the elastic constants, Young's modulus, and Poisson's ratio indicate the monolayer has good mechanical properties. Because of the existence of van Hove singularity, the spontaneous magnetization could be realized and nonmagnetic-to-ferromagnetic transition occurs through hole doping in the monolayer, and the ferromagnetism is stable at room temperature. Moreover, the GaOCl monolayer exhibits multidirectional piezoelectricity with large piezoelectric constants. The results indicate that the wide-bandgap GaOCl monolayer could possess tunable ferromagnetism and piezoelectricity, providing a promising candidate for electronic and spintronic applications.

3.2 Computational details

All calculations were carried out based on density functional theory (DFT) using the Vienna ab initio Simulation Package (VASP) [118]. The projector-augmented wave (PAW) method was used to describe the ion-electron interaction. The generalized gradient approximation (GGA) [113] with the Perdew-Burke-Ernzerhof (PBE) functional was used for the exchange-correlation part of the electron-electron interaction. The plane-wave energy cutoff was set to 500 eV. The full relaxation of structures was performed until the Hellmann–Feynman force on each atom was less than 10^{-3} eV Å^{-1}. The convergence criterion of electronic iteration was set to be 10^{-6} eV for the total energy. The Brillouin zone was sampled with a 7 × 7 × 1 Monkhorst–Pack k-point grids for structural optimization [142]. To study the 2D system under periodic boundary conditions, a vacuum layer of at least 15 Å was introduced along the z-axis to avoid spurious interactions between periodic images. Electronic band structures were obtained by PBE functional and compared with those from the Heyd–Scuseria–Ernzerhof (HSE06) screened hybrid functional [143]. The phonon spectrum was calculated using PHONOPY code [144] with a 3 × 3 × 1 supercell. *Ab initio* molecular dynamics (AIMD) simulations were performed at 300 K under the NVT ensemble up to 6 ps [145]. Piezoelectricity was studied by using density functional perturbation theory (DFPT) [146]. The van der Waals (vdW) correction proposed by the DFT-D3 approach in Grimme's scheme was chosen to describe the intralayer long-range interaction [147].

3.3 Results and discussions

3.3.1 Structure of bulk

To calibrate the theoretical approach, we first focus on the crystal structure and electronic properties of bulk GaOCl firstly synthesized in 1963 [148], which have been previously examined [149-151]. GaOCl possesses the intrinsic layered structure connected by the weak vdW interaction, and belongs to the $Pca2_1$ space group, as shown in Figure 3.1(a). The cubic pristine cell is highlighted with grey dotted lines. Each metal atom is positioned in a slightly distorted tetrahedron coordinated to three

O^{2-} and one Cl^{-} ions. Oxygen atoms are shared by three tetrahedra and joined together in the puckered layers in the middle, while chlorine atoms are dependently located at the alternating sides of the Ga-O skeleton along with the given arrangement of tetrahedra. The lattice constants of fully-optimized crystal are a = 5.13 Å, b = 5.71 Å, and c = 8.34 Å, which are consistent with the experiment results (a = 5.08 Å, b = 5.65 Å, and c = 8.32 Å) [148, 149]. Each atomic layer has a thickness of 5.72 Å and stacks directly along the z-direction with an interlayer distance of 2.76 Å. Such a particular structure strongly implies that monolayer GaOCl might be exfoliated from the bulk in a manner similar to that of graphene from graphite.

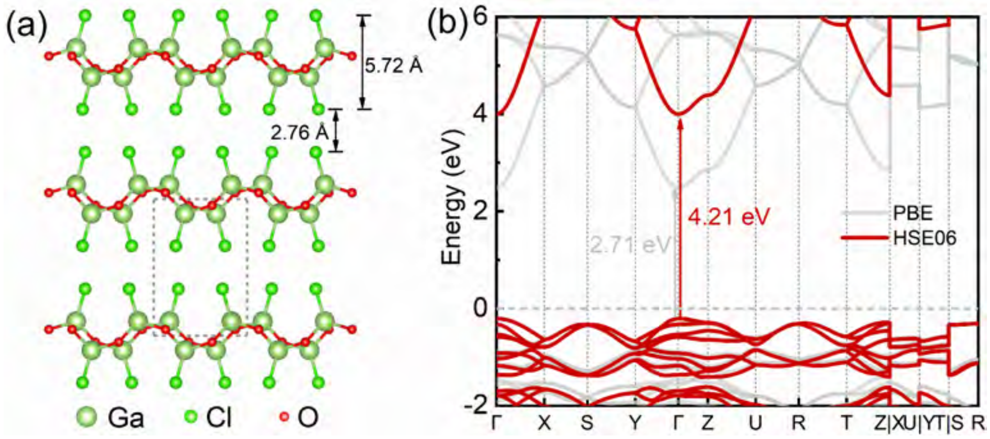

Figure 3.1 (a) The crystal structure of bulk GaOCl. The unit cell used is outlined by dash lines. (b) Electronic band structure (PBE and HSE06 levels) of bulk GaOCl. The Fermi level is set to zero.

The electronic band structure of bulk GaOCl is calculated using the PBE and HSE06 functionals, respectively, while the latter gives more accurate results. As shown in Figure 3.1(b), the dispersion of band edges expressed by grey and red lines is accordant. The VBM and the CBM are both lied at the Γ point, indicating that bulk GaOCl is a direct-bandgap semiconductor with a bandgap of 4.21 eV (2.71 eV at the PBE level). Such bandgap value is larger than those of some Ga-based materials, such as GaTeCl (2.96 eV) [152], wurtzite GaN (3.5 eV) [153] and a bit smaller than that of β-Ga_2O_3 (4.85 eV) [132].

3.3.2 Structure and stability of monolayer

To quantitatively evaluate the experimental feasibility of peeling off the GaOCl monolayer from its bulk, we simulate the process of mechanical exfoliation, as shown in Figure 3.2(a). A model with four atomic layers is adopted here and viewed as the bulk GaOCl: the bottom three layers are fixed, while the top layer is exfoliated far from the remnant part along the *z*-direction. The cleavage distance d_e is defined as the difference between the real and initial interlayer distance ($d - d_0$). The cleavage energy E_{cl} is defined as the energy required to cleave an infinite bulk crystal into two semi-infinite parts, and so is the energy to be applied for the creation of two surfaces. In the supercell approach, E_{cl} is calculated as the total-energy difference per unit surface area through the following formula: $\mathrm{E}_{cl} = \frac{(\mathrm{E}_{nl}+\mathrm{E}_{bulk-nl})-\mathrm{E}_{bulk}}{S}$, where E_{nl}, E_{bulk}, and $\mathrm{E}_{bulk-nl}$ are the total energies of monolayer GaOCl, bulk GaOCl, and the rest of bulk GaOCl after exfoliated by one layer, respectively. S is the cross-sectional area at the *ab*-plane. With increasing d_e, the cleavage energy E_{cl} increases gradually and then tends to a constant. As a result, the calculated E_{cl} of GaOCl is about 0.14 J/m^2, dramatically lower than that of BP (0.40 J/m^2) obtained using the same method. Since the BP has been exfoliated successfully in experiments, the relatively low E_{cl} for 2D GaOCl suggests that it is highly possible to obtain the GaOCl monolayer using the mechanical exfoliation method in experiments.

In the 2D limit, GaOCl monolayer exhibits an orthorhombic lattice with the C_{2v} point group. Compared with that of FeOCl-type monolayer predicted by He *et al*. [154], the structure of GaOCl monolayer studied in this work has lower total energy and better stability. Figure 3.2(b) shows the top view and side view of the GaOCl monolayer, and the optimized lattice constants are a = 5.18 Å and b = 5.71 Å, which are a little larger than those of its bulk counterpart. It could be caused by the quantum size effects which are found to exist in most 2D materials. The primitive cell of monolayer consists of 12 atoms (4 Ga, 4 Cl, and 4 O atoms). In a distorted tetrahedron, the Ga-O bonds are slightly different in bond length (varying from 1.88 to 1.91 Å), and the bond angles of O-Ga-O range from 100.56° to 106.98°. All Ga-Cl bonds are identical with the same length of 2.12 Å.

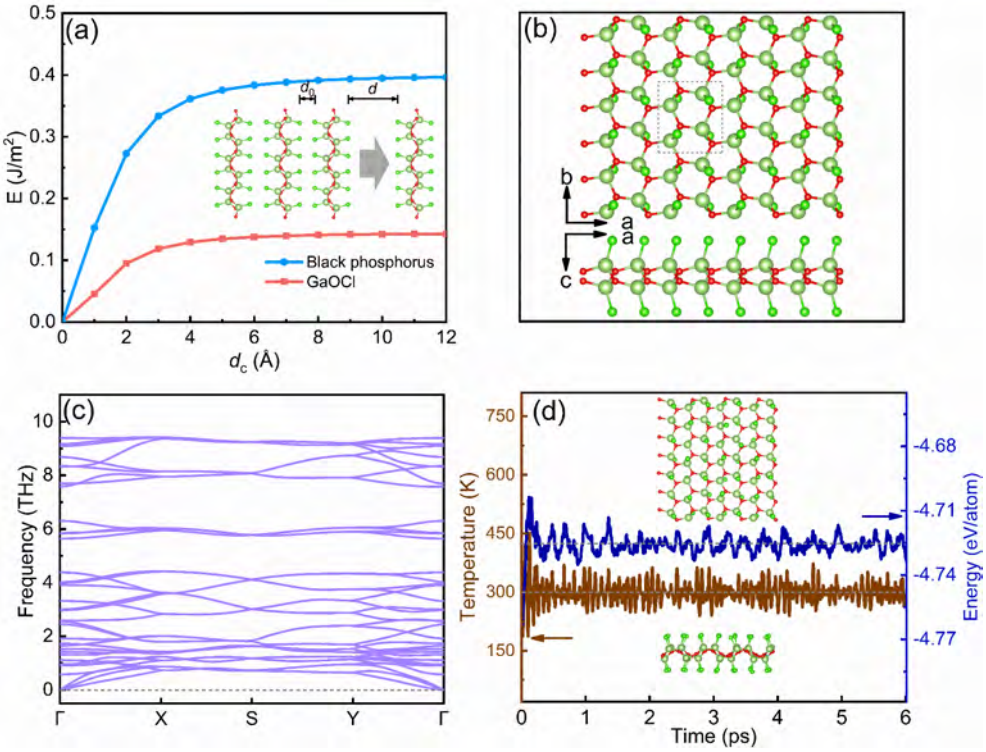

Figure 3.2 (a) Cleavage energy (E_{cl}) as a function of the cleavage distance (d_e) between the top layer and bottom layer of GaOCl and BP. The inset is the schematic diagram of

the cleavage process in generating the GaOCl monolayer from its bulk counterpart. (b) Top view and side view of GaOCl monolayer. (c) Phonon spectrum of GaOCl monolayer. (d) The variation of temperature and total energy during AIMD simulations at 300 K. The inset is the snapshots of monolayer taken at the end of the simulation.

To assess the stability of the GaOCl monolayer, the phonon spectrum and AIMD simulations are carried out. As shown in Figure 3.2(c), the absence of imaginary frequency in the phonon dispersion indicates its dynamical stability. Moreover, its thermal stability is evaluated using a 3 × 3 × 1 supercell at 300 K. The structural snapshots of the GaOCl monolayer after annealing for 6 ps with a time step of 2 fs are shown in Figure 3.2(d). Clearly, there is no broken bond and the whole configuration keeps well in its initial state. With a slight total energy fluctuation, it is confirmed that the GaOCl monolayer is thermally stable at room temperature.

3.3.3 Tunable electronic properties of monolayer

After verifying the excellent stability of GaOCl monolayer, systematic studies on its electronic properties are carrier out to reveal its viability for electronic and optoelectronic applications. The electronic band structures calculated at PBE level and corrected by those at HSE06 level are shown in Figure 3.3(a). Obviously, both the CBM and VBM are located at the Γ point with a bandgap of 4.46 eV (2.94 eV) at the HSE06 (PBE) level, implying that GaOCl monolayer is a direct-bandgap semiconductor. This characteristic could effectively promote electrons transition directly from the valence band to the conduction band while simultaneously emitting or absorbing photons, which is favourable for optoelectronic applications. Such bandgap is evidently wider than those of most reported 2D materials, such as InTeI [155] and Bi_2WO_6 [156], indicating that the GaOCl monolayer has great potential for applications in the absorbance and detection of ultraviolet light. Furthermore, the partial density of states (PDOS) is also plotted to analyze its electronic properties. The VBM is mainly occupied by the *p*-orbital of Cl atoms, while the CBM results from the combined action of Ga, Cl, and O atoms with strong hybridization. The electron density distributions at CBM and VBM displayed in Figure 3.3(b) come to the same conclusion. It is worth noting that the valence band at Γ point presents a characteristic "Mexican hat" shape, resulting in the divergent nature of the density of states. This so-called van Hove singularity point could induce the electronic instability, which highly likely leads to the occurrence of ferromagnetic order under hole doping in the monolayer.

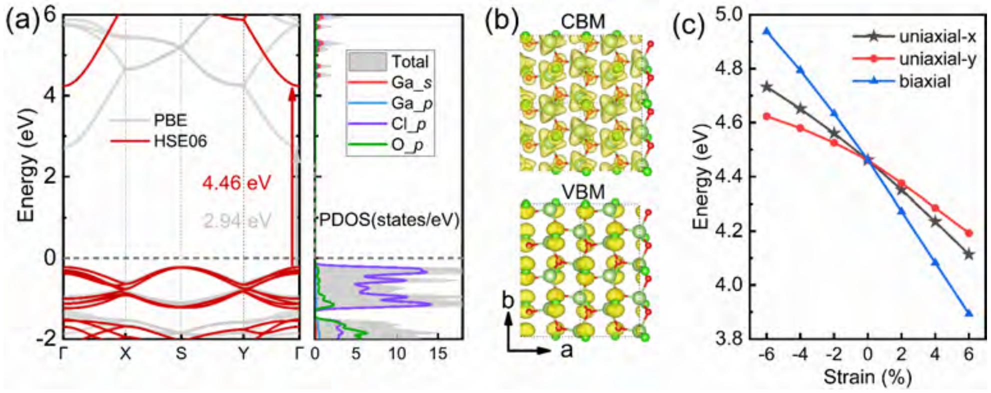

Figure 3.3 (a) Electronic band structure (at PBE and HSE06 levels) and partial density of states (PDOS) of GaOCl monolayer. The Fermi level is set to zero. (b) Electron density distribution at CBM and VBM. (c) The bandgap of GaOCl monolayer as a function of the in-plane uniaxial and biaxial strains ranging from − 6 % to + 6 %.

Since the electronic band structure of 2D nanosheets is sensitive to the alteration in their geometrical constructions, strain engineering is a common method to modulate their electronic properties. Herein, the variation of band structures of GaOCl monolayer under different uniaxial and biaxial strains varying from –6% to +6% is investigated, as shown in Figure 3.3(c). Clearly, the bandgap almost increases (decreases) linearly with increasing compressive (tensile) strain applied along the uniaxial or biaxial direction. Compared to those affected by the applied uniaxial strains (the minimum or maximum bandgap is 4.11 eV (4.19 eV) or 4.73 eV (4.62 eV), under +6% or −6% strains along x- (y-) direction, respectively), the bandgap is modulated more significantly (the minimum or maximum bandgap is 3.89 eV or 4.94 eV, under +6% or −6% strains, respectively) by the applied biaxial strains.

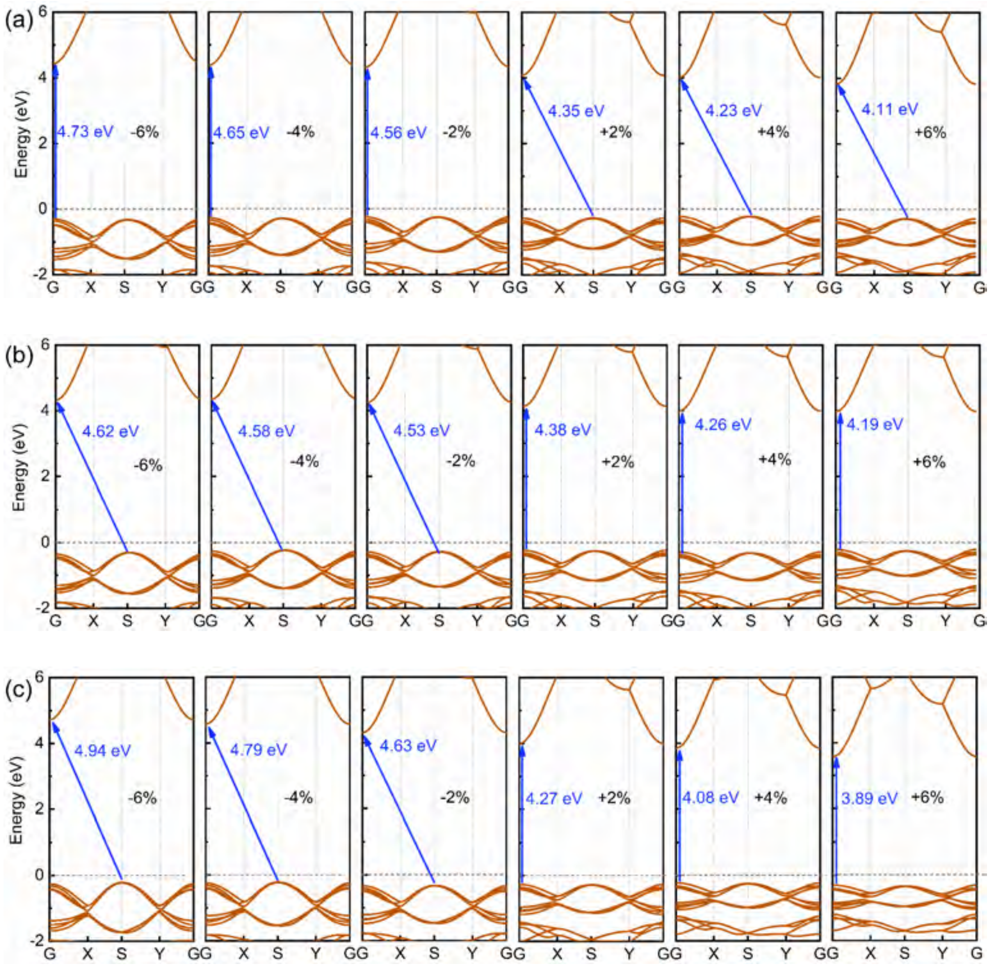

Figure 3.4 HSE06 band structures of GaOCl monolayer under the in-plane uniaxial strains varying from −6% to +6% along (a) x-, (b) y- and (c) xy-direction.

In addition to adjusting the bandgap, the external strains can also induce the shifts of band edges, as shown in Figure 3.4. When the uniaxial x-tensile strain is applied, the VBM of GaOCl monolayer move to the S point from Γ point, inducing the appearance of indirect bandgap. However, the compressive strains cannot change the direct-bandgap nature of GaOCl monolayer. The opposite bandgap characteristics can be found in the case under uniaxial y-direction strain (compressive strain: indirect bandgap; tensile strain: direct bandgap). Such different trend can be understood from the strength of the atomic bonds along the x- and y- direction. If the biaxial strains are considered, direct-to-indirect transition of bandgap is determined under compressive strains while the biaxial tensile strains do not change the intrinsic direct bandgap of GaOCl monolayer. The slight difference in the energy at Γ and S points should be the reason that such diverting phenomenon could occur. As a result, it is effective to modulate the electronic properties of GaOCl monolayer through applied strains.

3.3.4 Carrier mobility of monolayer

Table 3.1 The electronic transport parameters of GaOCl monolayer: effective mass (m^*), elastic moduli (C), deformation potentials (E_d), and carrier mobility (μ).

Direction	Carrier type	m^*/m_0	C (N/m)	E_d (eV)	μ (cm^2 V^{-1} s^{-1})
x	electron	0.415	58.03	5.68	229.96
	hole	2.658	58.03	1.58	124.31

y	electron	0.504	47.52	4.20	209.02
	hole	0.76	47.52	1.54	418.72

Besides the tunable bandgap, the transport properties of GaOCl monolayer are a significant indicator of its semiconductive properties, which are described by the carrier mobility along with the specific directions. Based on the effective mass approximation and the electron–acoustic phonon scattering mechanism, the carrier mobility of anisotropic 2D materials can be calculated by the modified formula based on the deformation potential (DP) theory, as follows [157]:

$$\mu_x = \frac{e\hbar^3\left(\frac{5C_{11}+3C_{22}}{8}\right)}{k_B T(m_x^*)^{\frac{3}{2}}(m_y^*)^{\frac{1}{2}}\left(\frac{9E_x{}^2+7E_xE_y+4E_y{}^2}{20}\right)}, \qquad 3.1$$

$$\mu_y = \frac{e\hbar^3\left(\frac{5C_{22}+3C_{11}}{8}\right)}{k_B T(m_y^*)^{\frac{3}{2}}(m_x^*)^{\frac{1}{2}}\left(\frac{9E_y{}^2+7E_xE_y+4E_x{}^2}{20}\right)}, \qquad 3.2$$

where k_B, T, e, and $\hbar$ are the Boltzmann constant, temperature, electron charge, and Planck constant divided by 2π, respectively. E_d is the DP constant, representing the shift of the CBM (VBM) for electrons (holes) induced by lattice change, and is calculated as $d\mathrm{E}_{edge}/d\varepsilon$, where E_{edge} is the energy of the band edge. C_{ij} is the elastic modulus of 2D systems, denoted as $C = [\partial^2 E/\partial\varepsilon^2]/S_0$, E is the total energy of the system, ε is the applied uniaxial strain, and S_0 is the area of the optimized system. The fitting curve in obtaining C_{ij} of GaOCl monolayer is shown in Figure 3.5. The effective mass of carrier m^* is defined as $m^* = \pm\hbar^2(\frac{d^2E_k}{dk^2})^{-1}$, E_k and k stand for the band energy and electron wave vector, respectively. All the calculated results of the above-mentioned parameters are listed in Table 3.1. Clearly, the GaOCl monolayer possesses an electron mobility along the *x*-direction up to 229.96 cm^2 V^{-1} s^{-1}, which is close to that along the *y*-direction. Moreover, the hole mobility along the *x*-direction is about 124.31 cm^2 V^{-1} s^{-1}, significantly lower than that along the *y*-direction (418.72 cm^2 V^{-1} s^{-1}). Such anisotropic mobility is mainly due to the larger effective mass along the *x*-direction and is beneficial to reduce the possibility of recombination of the photogenerated carriers. This value for GaOCl monolayer is larger than that of graphene (45 ~ 105 cm^2 V^{-1} s^{-1}) [158] and comparable to that of MoS$_2$ (200 ~ 500 cm^2 V^{-1} s^{-1}) [159]. In addition to enhancing the efficiency and performance of the photoelectronic devices, the high carrier mobility also endows GaOCl monolayer as a promising candidate for applications in modern high-performance electronic devices.

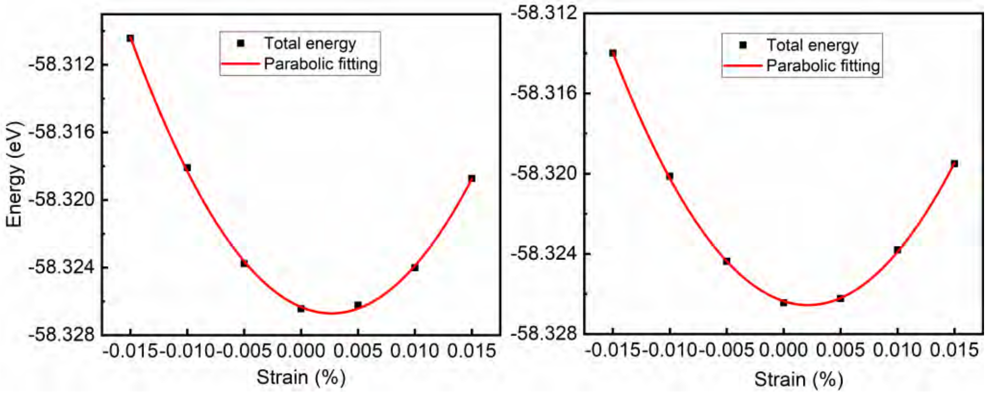

Figure 3.5 The total energy of GaOCl monolayer as a function of the uniaxial strain applied along (a) x-direction, and (b) y-direction, respectively.

3.3.5 Mechanical properties of monolayer

The mechanical properties of the GaOCl monolayer are studied by the strain-energy method based on the harmonic approximation [160]. According to the symmetry analysis, non-zero and independent elastic constants of GaOCl monolayer can be derived from the second-order derivative of the total energies versus strain as $C =$

$[\partial^2 E/\partial\varepsilon^2]/S_0$. The calculated results are C_{11} = 58.03 N/m, C_{12} = 10.81 N/m, C_{22} = 47.52 N/m, and C_{66} = 27.55 N/m, satisfying well the Born criteria ($C_{11}C_{22} - C_{12}^2 > 0$ and $C_{66} > 0$) and demonstrating the mechanical stability of the GaOCl monolayer. Based on the elastic constants, the in-plane Young's modulus and Poisson ratio as a function of θ also can be estimated by the following formula:

$$Y(\theta) = \frac{C_{11}C_{22} - C_{12}^2}{C_{22}\cos^4\theta + A\cos^2\theta\sin^2\theta + C_{11}\sin^4\theta}, \qquad 3.3$$

$$v(\theta) = \frac{C_{12}\cos^4\theta - B\cos^2\theta\sin^2\theta + C_{12}\sin^4\theta}{C_{22}\cos^4\theta + A\cos^2\theta\sin^2\theta + C_{11}\sin^4\theta}, \qquad 3.4$$

where $A = (C_{11}C_{22} - C_{12}^2)/C_{66} - 2C_{12}$ and $B = C_{11} + C_{22} - (C_{11}C_{22} - C_{12}^2)/C_{66}$. The corresponding angle-dependent Young's modulus and Poisson's ratio are shown in Figure 3.6(a) and 3.6(b), respectively. It can be seen that the Young's modulus varies from 45.51 to 59.93 N/m, demonstrating the distinct anisotropy. These values are comparable to that of phosphorene (24–102 N/m) [161] but significantly smaller than those of graphene (340 N/m) [162], MoS_2 (120-240 N/m) [163] and h-BN (271 N/m) [164], indicating the low stiffness and high flexibility of GaOCl monolayer and thus large elastic deformation under applied stresses. The Poisson's ratio is a parameter that quantitatively represents the transverse deformation of a material in the directions perpendicular to the specific direction of loading. The Poisson's ratio shown in Figure 3.6(b) exhibits remarkable anisotropy, namely, the maximum value (0.23) along the x- and y-axis and the minimum value (0.07) along the diagonal direction are much different. Meanwhile, these positive values mean that the GaOCl monolayer expands (contracts) laterally under compressive (tensile) strains. According to the theory reported by Litvinenko *et al* [165], the lower values (< 0.5) of

Poisson’s ratio indicate good compressibility of GaOCl monolayer.

Besides, the ultimate tensile strength (UTS) is also a valuable parameter to estimate the mechanical performance of 2D materials, defined as the maximum tensile stress that a material can undertake before breakage occurs. Here, the UTS of GaOCl monolayer is evaluated by the deformations along the uniaxial and biaxial directions, as depicted in Figure 3.6(c). Under small applied strains, there is a linear relationship with elastic anisotropy. The deformation can be maintained before the applied strain of 22% (30%) along the x- (y-) direction, with the UTS reaching 9.44 N/m (9.18 N/m). Moreover, the UTS under biaxial tension is 8.84 N/m, corresponding to an applied strain of 21%. Namely, the GaOCl monolayer could have good ductility exceeding 20% and high mechanical strength as high as 16.5 GPa. Therefore, the GaOCl monolayer not only has a ductility better than those of most 2D materials, such as penta-graphene (18%) [166], WS_2 (12%) [167], and MoS_2 (6%~11%) [163], but also has a large mechanical strength.

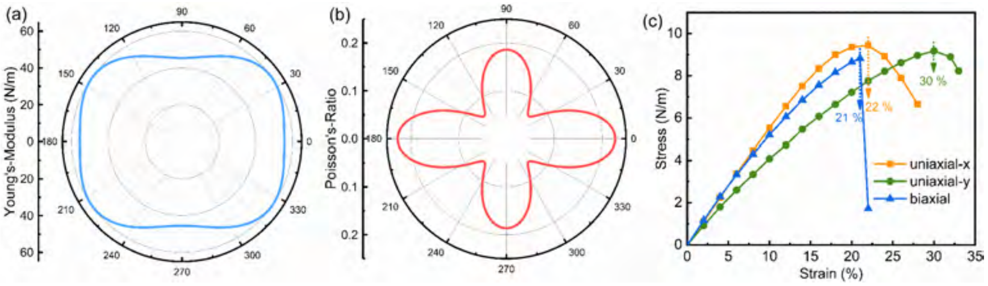

Figure 3.6 The orientation dependent (a) in-plane Young’s modulus and (b) Poisson’s ratio of GaOCl monolayer. (c) The stress-strain relations under biaxial and uniaxial (x and y directions) tensions for GaOCl monolayer.

3.3.6 Hole-doping induced magnetism

The abovementioned van Hove singularity point on the valence band indicates the possibility of a transition from the nonmagnetic to ferromagnetic states when the Fermi level is close to the divergent point, as reported in some 2D materials [133, 168, 169]. It is known that carrier doping can precisely cause the shifts of Fermi level. Thus, the influence of hole doping on the ferromagnetisms of GaOCl monolayer can be explored through spin-polarized DFT calculations. The change in the total number of electrons and a compensating jellium background of opposite charges collectively maintain the neutrality of the unit cell. The stability of ferromagnetic states is examined using the spin-polarization energy, which is defined as the energy difference between the spin and non-spin states, $\Delta \mathrm{E} = (E_{\text{non-spin}} - E_{\text{spin}})/\mathrm{n}_{\text{hole}}$, and the positive values could confirm the ferromagnetic ground states. The magnetic moment and spin-polarization energy as a function of doping density are plotted in Figure 3.7(a). Since the excessive doping concentration would lead to the structural damage inevitably¸ the density of 2 holes per unit cell (namely $6.83 \times 10^{14}/\mathrm{cm}^2$) is the upper limit considered in our study. Clearly, the spontaneous ferromagnetic phase occurs immediately at a small doping hole density (as low as $10^{13}/\mathrm{cm}^2$) and realizes 100% spin states with a magnetic moment of 1 μ_B per carrier (μ_B is the Bohr magneton). As the doping concentration increases, the injected holes are fully spin-polarized and the spin-polarization energy increases monotonically. It reaches 106.96 meV/hole at a density of $6.83 \times 10^{14}/\mathrm{cm}^2$, much higher than those of GaSe (3 meV/hole) [88], MoN_2 (75 meV/hole) [170], and $SnS_2/SnSe_2$ (500-100 meV/hole) [171], proving the strong stability of doping-induced ferromagnetism in GaOCl monolayer, which is beneficial for spintronics applications. Moreover, the work function of the monolayer could measure the feasibility of the escape of an electron, namely, the hole doping in the monolayer. In experiment, a doping density of about 4 × $10^{14}/\mathrm{cm}^2$ for 2D $Cr_2Ge_2Te_6$ has been realized through electrostatic gating [172]. With a work function (2.63 eV) lower than that of 2D $Cr_2Ge_2Te_6$ (4.97) as calculated by He *et al.* [173], the doping density could be practically realized in experiments for GaOCl monolayer studied in this work.

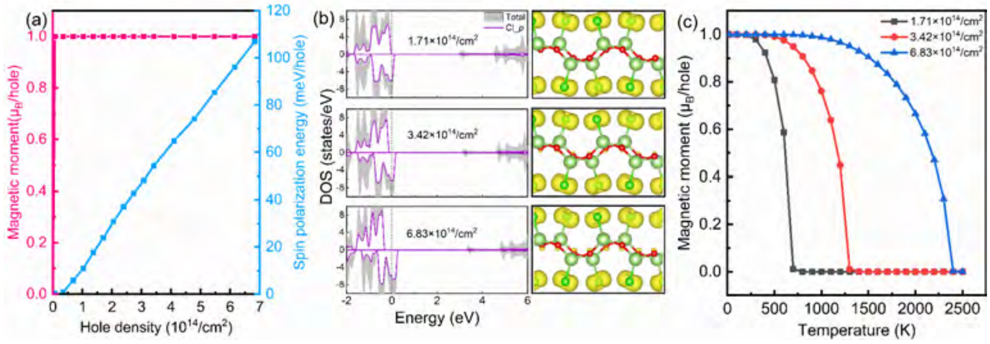

Figure 3.7 (a) Magnetic moment and spin-polarization energy as a function of hole concentration. (b) Spin-polarized partial density of states and the corresponding spin-density distribution under different hole doping densities. The yellow isosurfaces denote the spin charge density. (c) Doping-induced magnetic moment versus temperature at three different doping levels.

The spontaneous ferromagnetic order in the hole-doped GaOCl monolayer can be explained qualitatively by the Stoner mechanism [174, 175] of ferromagnetism in detail, which has been studied in nitrides and oxides with d^0 configuration [176]. In this model, the itinerant ferromagnetism tends to appear spontaneously when the criterion $ID(E_\mathrm{f}) > 1$ is met, where I is the strength of exchange interaction and $D(E_\mathrm{f})$ is the DOS at the Fermi energy of the nonmagnetic state. $I = \Delta\mathrm{ex}/M$ [177], where $\Delta\mathrm{ex}$ is the spin-splitting energy between the two spin subbands and M is the total magnetic moment per atom. The solid-state chlorine is always found in a closed-shell configuration with strong bonding, which leads to a large band dispersion and consequently small $D(E_F)$. For the peculiar electronic structure of the valence band of GaOCl monolayer, there is a direct proportionality between $D(E_F)$ and $m^*\sqrt{E_{vbm} - E_F}$, so that moderate doping can result in a large $D(E_F)$ and hence magnetism. For example, the calculated I and $D(E_F)$ are 0.30 and 9.25 at $1.71 \times 10^{14}/\text{cm}^2$, respectively, satisfy the criterion $ID(E_f) > 1$. Besides, beyond the critical level, GaOCl monolayer well manifests the criterion, indicating the existence of itinerant ferromagnetism in the hole-doped GaOCl monolayer.

In occurrence of ferromagnetisms, spin-polarized DOS with the energy splitting is of importance. Figure 3.7(b) displays the DOS of GaOCl monolayer under different hole-doping densities, where the spin-down states are crossed by the Fermi energy and the spin-up one is fully occupied, resulting in the half-metal property. It is obvious that the ferromagnetic order is prominently contributed by the p-orbital of Cl atoms. As the hole density increases, the spin splitting becomes larger gradually, reaching a value of 0.86 eV at $6.83 \times 10^{14}/\text{cm}^2$. The corresponding spin-density distribution shown in Figure 3.7(b) also provided the favorable evidence.

Normally, higher spin polarization signifies the stronger ferromagnetic coupling and thus results in a higher Curie temperature T_c. We further estimate the hole-doping dependent thermal stability of the GaOCl monolayer, which could be reflected by T_c. The finite temperature T is introduced to the system by adjusting the smearing factor

$\sigma = k_B T$ in the Fermi-Dirac distribution as described by the function 3.5 [178]:

$$f\left(\frac{\epsilon-\mu}{\sigma}\right) = \frac{1}{\exp\left(\frac{\epsilon-\mu}{\sigma}\right)+1}, \qquad 3.5$$

where μ is chemical potential. Here, different doping levels are chosen to evaluate the changes in the magnetic moment as the temperature is varied, as shown in Figure 3.7(c). Under a low doping density of 1.71 × 10^{14}/cm^2, the magnetic moment suddenly disappears at about 700 K. As expected, a higher transition temperature (defined as T_c) emerges as the doping density increases. For example, T_c surges to 1400 K and 2500 K under the doping density of 3.42 × 10^{14}/cm^2 and 6.83 × 10^{14}/cm^2, respectively. Such above-room temperature T_c is much higher than that of intrinsic magnetic systems and even higher than those of some systems with doping-induced ferromagnetism [88, 89, 179], implying the ultrahigh ferromagnetic stability of GaOCl monolayer under various hole-doping concentrations.

3.3.7 Piezoelectricity of monolayer

For piezoelectric materials, the third-rank piezoelectric stress tensor e_{ijk} and the strain tensor d_{ijk} can be evaluated by $e_{ijk} = \frac{dP_i}{d\varepsilon_{jk}}$ and $d_{ijk} = \frac{dP_i}{d\sigma_{jk}}$, respectively, where P_i, ε_{jk}, and σ_{jk} are the polarization tensor, strain tensor, and stress tensor, respectively. When the thickness is reduced to that of an atomic layer, the 2D GaOCl monolayer belongs to the C_{2v} point group without the centrosymmtery. That is to say, the in-plane and out-of-plane piezoelectricity occur simultaneously in this system. Since the nonzero and independent piezoelectric coefficients are determined by the crystal symmetry, the piezoelectric tensors of GaOCl monolayer in the form of Voigt notation can be expressed as

$$e_{ij} = \begin{pmatrix} e_{11} & e_{12} & 0 \\ 0 & 0 & e_{26} \\ e_{31} & e_{32} & 0 \end{pmatrix}, \quad 3.6$$

$$d_{ij} = \begin{pmatrix} d_{11} & d_{12} & 0 \\ 0 & 0 & d_{26} \\ d_{31} & d_{32} & 0 \end{pmatrix}, \quad 3.7$$

and are linked by the elastic constant through the equation $e_{ij} = d_{ij}C_{ij}$. Therefore, the corresponding piezoelectric strain coefficients can be written as

$$d_{11} = \frac{e_{11}C_{22} - e_{12}C_{12}}{C_{11}C_{22} - C_{12}^2}, \quad 3.8$$

$$d_{12} = \frac{e_{11}C_{12} - e_{12}C_{11}}{C_{12}^2 - C_{11}C_{22}}, \quad 3.9$$

$$d_{26} = \frac{e_{26}}{C_{26}}, \quad 3.10$$

$$d_{31} = \frac{e_{31}C_{22} - e_{32}C_{12}}{C_{11}C_{22} - C_{12}^2}, \quad 3.11$$

$$d_{32} = \frac{e_{31}C_{12} - e_{32}C_{11}}{C_{12}^2 - C_{11}C_{22}}. \quad 3.12$$

Table 3.2 Calculated piezoelectric coefficients e_{ij} (pC/m) and d_{ij} (pm/V) for GaOCl monolayer.

e_{11}	e_{12}	e_{26}	e_{31}	e_{32}	d_{11}	d_{12}	d_{26}	d_{31}	d_{32}
100.88	45.43	21.58	0.85	2.45	1.63	0.59	0.78	0.01	0.05

Based on the DFPT calculations, the nonzero coefficients e_{ij} and d_{ij} are obtained and listed in Table 3.2. It can be seen that the polarization along three different directions (*x*, *y*, and *z*) are generated synchronously when the linear strain along *x*- and *y*-directions and nonlinear strain along the *xy*-direction are applied. The e_{11} coefficient is two orders of magnitude larger than that of h-BN (1.384 pC/m) and the calculated d_{11} coefficient is comparable with those of group III–V and group-V binary buckled honeycomb monolayers [55, 56]. Besides, the out-of-plane $d_{31}$and d_{32} coefficients are in the same order of magnitude as compared with those of $CuInP_2S_6$ and $AgInP_2Se_6$ monolayers [138]. For most 2D materials, the polarization is insensitive to the shear strains due to their crystal symmetry. Interestingly, such a rare piezoelectricity can be found in GaOCl monolayer with excellent e_{26} and d_{26} coefficients. Compared with those of penta-BCN [180], penta-CNP [181], penta-BNSi [182], the piezoelectric performance of GaOCl monolayer generated by in-plane shear strains is obviously much better. Therefore, with the aforementioned high piezoelectric coefficients, the GaOCl monolayer has the multifunctional piezoelectricity which is more meaningful and beneficial for the nano-electromechanical devices.

3.4 Conclusions

In summary, based on first-principles calculations, a novel wide-bandgap GaOCl monolayer with an excellent dynamical and thermal stability at room temperature is predicted and its electronic properties are systematically investigated. The direct bandgap of monolayer is as large as 4.46 eV (at HSE06 level), beneficial for optoelectronic applications in utilizing blue and ultraviolet light. Furthermore, the bandgap can be modulated by strain engineering effectively, which can be increased to 4.94 eV under a biaxial compressive strain of −6%. The monolayer exhibits high mechanical flexibility and anisotropy, as well as good tensile ductility (>20%) and high mechanical strength (>16.5 GPa). More importantly, hole doping could induce the spontaneous magnetization and realize the full spin-polarized state in the monolayer with a low doping density. Besides, the in-plane and out-of-plane piezoelectricity are found to emerge simultaneously in the monolayer due to its specific crystal symmetry. Such a novel 2D semiconductor with wide bandgaps and tunable piezoelectricity and ferromagnetism could be a promising candidate for applications in multifunctional integrated nano-devices, which is awaiting further experimental verification.

Chapter 4 2D Janus Gallium oxychloride (GaOClX, X=F, Br, I)

4.1 Introduction

Recently, devices for energy conversion and storage such as dielectric capacitors, electrochemical supercapacitors and batteries have been developed rapidly. Among those energy storage devices, dielectric capacitors are unique since they can release the stored electrical energy in an extremely short period of time (about 1 μs) and generate pulse currents with high voltages [36, 183-185]. The basic structure of a dielectric capacitor is in a sandwich configuration, consisting of a dielectric layer and two conductive plates or electrodes on its both sides [34]. Under applied electric fields, the dielectric materials are polarized rapidly and the positive and negative charges of equal value are separately accumulated on the electrodes. Although the power density of conventional dielectrics is extremely high (up to 10^8 W/kg), their energy density (less than 10 J/cm^3) is much lower than those of electrochemical supercapacitors and batteries [34]. Therefore, it is an urgent task to explore novel dielectric materials with improved electric energy storge density, which are much desirable for energy storage devices with small dimensions, light weight, high efficiency and thermal stability.

Typically, there are four types of dielectric materials, *i.e.*, ferroelectrics, relaxor ferroelectrics, anti-ferroelectrics and linear dielectrics. The relaxor ferroelectrics have attracted much attention since they may possess large saturated polarization (P_{max}), small remnant polarization (P_r), and high electric breakdown strength [186-189], resulting in high energy storage density and efficiency. For the purpose of enhancing energy storage density, nano-dielectrics especially thin-film dielectrics are of much interest since they could exhibit ultrahigh electric breakdown strength. For examples, the (1-x)$BaTiO_3$-xBi(Mg, Ti)O_3 thin films were reported to possess a high breakdown strength (~2.17 MV/cm) with nearly linear polarization responses [190], and the energy storage density was as high as 37 J/cm^3; Ortega *et al.* studied $BaTiO_3/Ba_{0.3}Sr_{0.7}TiO_3$ superlattices which were found to possess a high breakdown strength of 5.8 ~ 6 MV/cm and a low leakage current density of 10 ~ 35 mA/cm^2, leading to a large recoverable energy storage density of 46 J/cm^3 [191]. Kim *et al.* investigated the ion-bombarded relaxor ferroelectric thin films $0.68Pb(Mg_{1/3}Nb_{2/3})O_3$-$0.32PbTiO_3$ which had an excellent combination of high polarization and ultrahigh electric breakdown strength [192], leading to an energy storage density as high as 133 J/cm^3. Nonetheless, the maximized energy storage densities of thin-film dielectrics (~100 J/cm^3) are still an order of magnitude lower than those of electrochemical supercapacitors and batteries. In general, thin-film nano-dielectrics with smaller thicknesses are more desirable to achieve ultrahigh energy storage density. In order to develop dielectric capacitors with their ultimate energy storage densities compatible to those of electrochemical supercapacitors and batteries, it is essential that the extreme of dielectrics, *i.e.*, dielectric monolayers with an atomic thickness, could be explored.

In the past two decades, a large family of 2D materials have been developed extensively. In particular, semiconducting monolayers exfoliated from van der Waals (vdW) materials are found to exhibit novel optical, dielectric, electrical and mechanical properties [193-195]. Although their bulk counterparts could be used as high-*k* or low-*k* dielectrics in electronic devices [196], 2D dielectric materials have not been well explored for their application as dielectric layers in capacitors. As mentioned above, dielectric monolayers with atomic thicknesses especially those wide bandgap semiconducting monolayers could possess ultrahigh electric breakdown strength. They are promising dielectrics which can be tailored to possess large polarization or high dielectric constants, leading to their ultrahigh energy storage densities.

Recently, 2D Janus materials have attracted much attention since they have novel physical and chemical properties especially the enhanced out-of-plane polarizations, resulting from their intrinsic asymmetric atomic structures. In our previous work, the wide bandgap GaOCl semiconducting monolayers with good thermal stability, high mechanical flexibility and doping-induced magnetisms were investigated by first-principles calculations [197]. Similar to Janus MoSSe monolayer prepared successfully through a bottom-up synthesis route [100], 2D Janus materials could be developed based on the GaOCl monolayer, which are potential candidates of 2D dielectric materials with ultrahigh energy storage densities. In this work, we systematically study the structural and thermal stabilities of Janus GaOClX (X = F, Br, and I) monolayers, which are expected to be facilely derived from the GaOCl monolayer through replacement reactions among halogen elements. Their wide indirect bandgap, anisotropic carrier mobility and mechanical properties, especially the large out-of-plane piezoelectric coefficients, are assessed comprehensively. More importantly, it is found that Janus GaOClX monolayers exhibit ultrahigh energy storage density (as high as

893.32 J/cm^3). The results are comparable with those of electrochemical supercapacitors, unparallel by other dielectric materials reported to date. Thus, this work opens a new window in searching for novel dielectric materials, which could be used in dielectric capacitors with superior energy storage density and power density, excellent efficiency and thermal stability.

4.2 Computational methods

The computation is based on density functional theory (DFT) [118, 198], using the Vienna *ab initio* simulation package (VASP) code. The core electrons are described by the projected augmented wave (PAW) pseudopotential method [199], while the generalized gradient approximation (GGA) exchange-correlation is treated by the Perdew-Burke-Ernzerhof (PBE) formulation [113]. The sampling on Brillouin zone in the reciprocal space is implemented with 6 × 6 × 1 k-point mesh by the Monkhorst-Pack scheme [142]. The cut-off energy is set to be 500 eV. Period boundary conditions are applied to the supercell where the model monolayer is separated by a vacuum slab of 25 Å along the z-direction to reduce the interlayer interaction. The convergences of energy and the Hellmann-Feynman force for a fully relaxed system are set to be 1×10^{-6} eV and 10^{-3} eV Å^{-1}, respectively. The density functional dispersion correction (DFT-D3) is employed to treat the weak dispersion forces [147]. The Heyd-Scuseria-Ernzerhof (HSE06) hybrid functional is used to determine the electronic structures [143]. The PHONOPY code is used to obtain the phonon dispersion, which is based on the density functional perturbation theory [144]. *Ab initio* molecular dynamics (AIMD) simulation at 300 K under the NVT ensemble is carried out in the model systems with $3 \times 3 \times 1$ supercell [145] and the simulation time is 6 ps.

4.3 Results and discussion

4.3.1 Atomic structure and stability of monolayers

The atomic structures of Janus GaOClX (X = F, Br, and Cl) monolayers are derived from GaOCl monolayer previously reported [197]. By substituting two chlorine atoms in one atomic layer with different halogen-element (X) atoms, the vertical mirror symmetry of GaOCl monolayer is broken, forming the Janus GaOClX monolayers shown in Figure 4.1. The atomic structure has six sublayers stacking in the order of Cl-Ga-O-O-Ga-X and each layer has atoms for one element only, and in turn their parental GaOCl structure is obtained by taking X = Cl. In this work, three possible Janus monolayers are investigated, including GaOClF, GaOClBr and GaOClI monolayers. As marked by grey dotted lines in Figure 4.1(a), the unit cell of GaOClX monolayers consists of four Ga, four O, two Cl, and two X atoms. After optimizations on their atomic structures by DFT calculations, as listed in Table 4.1, the lattice constants *a* and *b* as well as the interlayer thickness *d* of GaOClBr and GaOClI are found to be larger than those of GaOClF, which could be ascribed to the differences in atomic size and electronegativity of halogen elements. Each Ga atom is bonded with three O atoms, forming a distorted tetrahedron with slightly different bond lengths. There are Ga-Cl and Ga-X bonds, which are close to the atomic layers of oxygen and point outwards. Among the Ga-X covalent bonds, Ga-I bond is the longest (2.47 Å) while Ga-F bond is the shortest (1.75 Å), in consistent with those predicted by the periodicity. Table 4.1 compares the structural parameters of Janus GaOClX (X = F, Br, and Cl).

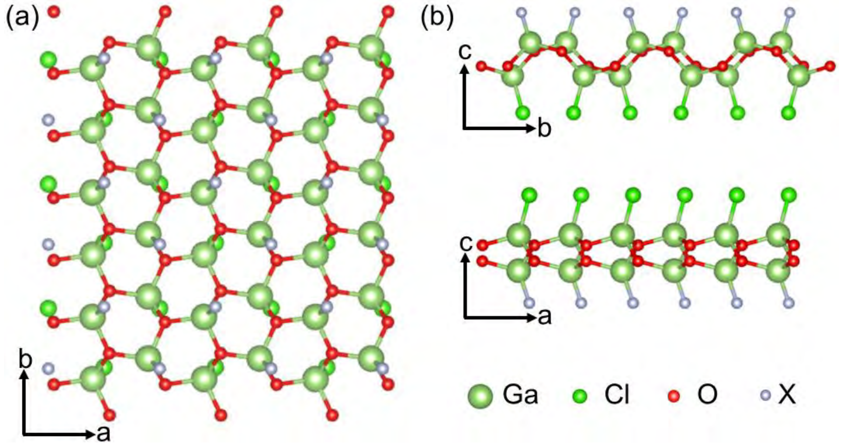

Figure 4.1 (a) Top view and (b) side view of atomic structure of GaOClX (X = F, Br, and I) monolayers.

To understand the stability of covalent-bonded GaOClX monolayers, the cohesive energy E_{coh} is calculated by the following formula:

$$E_{coh} = \frac{E_t - N_{Ga}E_{Ga} - N_O E_O - N_{Cl}E_{Cl} - N_X E_X}{N_{Ga} + N_O + N_{Cl} + N_X} \qquad 4.1$$

where E_t is the total energy of Janus GaOClX monolayers, $E_{element}$ and $N_{element}$ refer to single-atom energy and number of Ga, O, Cl, and X atoms in the unit cell, respectively. The calculated results are listed in Table 4.1. The cohesive energy of Janus GaOClX monolayers shows an upwards trend for GaOClF, GaOClBr and GaOClI, resulting from the increased electronegativity of X atoms that the formation of Janus GaOClX monolayers with stronger covalent-bonded networks is more viable. The negative values of cohesive energy E_{coh} demonstrate that the as-formed Janus GaOClX monolayers have thermodynamic stability. Although the cohesive energies of Janus GaOClX monolayers are higher than those of tetragonal TiC monolayer (−6.4 eV/atom) [200] and graphene (−8.66 eV/atom) [201], they are lower than those of single-layer metal halides such as $NiCl_2$ (−1.98 eV/atom) [202], indicating their structural stability.

Table 4.1 Calculated lattice constants *a* and *b*, interlayer thickness *d*, bond length of Ga-O, Ga-Cl, and Ga-X bonds, cohesive energy E_{coh}, and bandgaps E_g obtained with PBE and HSE06 for GaOClX (X = F, Br, and I) monolayers.

System	*a* (Å)	*b* (Å)	*d* (Å)	Ga-O (Å)	Ga-Cl (Å)	Ga-X (Å)	E_{coh} (eV)	PBE E_g (eV)	HSE06 E_g (eV)
GaOClF	5.12	5.71	5.34	1.87-1.91	2.12	1.75	-4.88	2.82	4.36
GaOClBr	5.14	5.75	5.90	1.88-1.91	2.12	2.26	-4.56	2.15	3.50
GaOClI	5.20	5.86	6.07	1.89-1.92	2.12	2.47	-4.45	1.05	2.18

The thermal and dynamical stabilities of Janus GaOClX monolayers are further investigated by AIMD simulations at 300 K and the computed phonon spectrum, respectively, as shown in Figure 4.2. From Figure 4.2(a-c), it is found that after AIMD simulation for 6 ps with a time step of 2 fs, the free energy converges with a fluctuation less than 0.004 eV. More importantly, their structural integrity is well maintained and there is no broken bond in the monolayers, indicating that the Janus GaOClX systems could be stable at room temperature. Moreover, the absence of considerable imaginary frequencies in the whole Brillouin zone in the phonon dispersion confirms that they could have dynamical stability, as shown in Figure 4.2(d-f). It is worth mentioning that the tiny protuberance like "U" shape near the Γ point in the phonon spectrum is the feature of flexural acoustic mode, which is not related to the stability of monolayers [203]. Such hard convergence of phonon bands is a common phenomenon and has been discussed for many 2D materials [60, 203, 204]. Interestingly, although X atoms are different for the Janus GaOClX monolayers, similar phonon dispersions for the monolayers are observed.

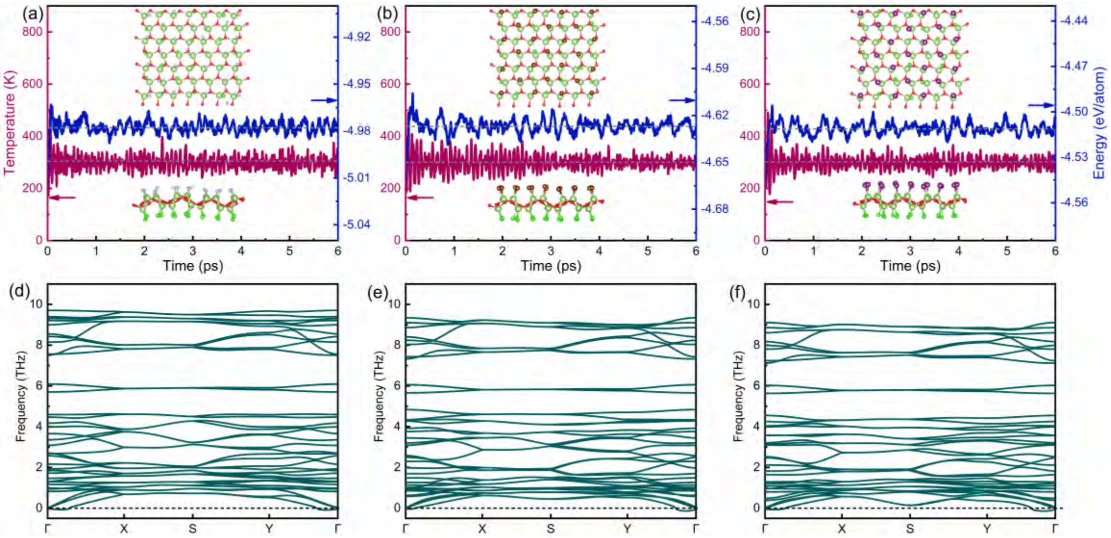

Figure 4.2 The variation of temperature and total energy during AIMD simulations at 300 K of (a) GaOClF, (b) GaOClBr, and (c) GaOClI monolayers. The inset shows the snapshots of systems taken at the end of the simulations. The phonon spectra of (d) GaOClF, (e) GaOClBr, and (f) GaOClI monolayers along with the high-symmetric points in the Brillouin zone.

4.3.2 Electronic properties of monolayers

The electronic properties of Janus GaOClX monolayers are evaluated by first-principles calculations on band structures. As shown in Figure 4.3, it is obvious that Janus GaOClX monolayers are semiconductive with an indirect bandgap E_g varying from 2.18 to 4.36 eV at HSE06 level (E_g = 1.05~2.82 eV at PBE level). Their CBM is located at Γ point while the VBM lies at S point. Since the difference in energies at Γ and S points is almost negligible, the Janus GaOClX monolayers can be considered as direct-bandgap semiconductors with a bandgap larger than those of conventional semiconductors. Compared with conventional semiconductors, such as silicon (E_g ~1.12 eV), the Janus GaOClX monolayers possess a bandgap within 2.18 ~ 4.36 eV tunable through replacing halogen atoms X, which is favorable for their electronic and optoelectronic applications. It is noted that the type of bandgap of Janus GaOClX monolayers is the same as their parental GaOCl monolayer, while the values of bandgaps are in the order of GaOClF > GaOCl > GaOClBr > GaOClI [197]. Among these monolayers, the bandgap of GaOClF monolayer (E_g = 4.36 eV) is the highest, which is larger than those of most 2D materials, such as InTeI (2.735 eV) [155], $GeSe_2$ (2.96 eV) [205], Ga_2O_3 (3.16 eV) monolayers [206].

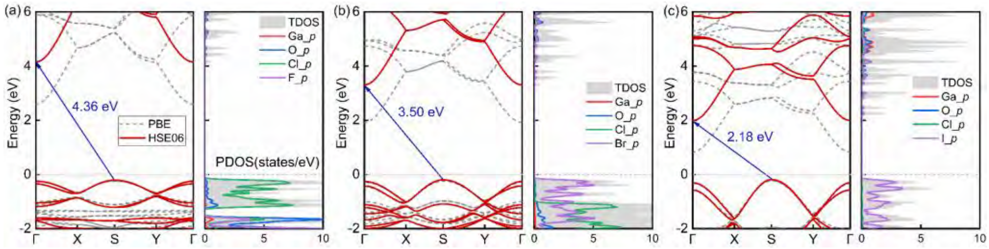

Figure 4.3 Electronic band structures (at the PBE and HSE06 levels), total density of states (TDOS) and partial density of states (PDOS) of (a) GaOClF, (b) GaOClBr, and (c) GaOClI monolayers. The Fermi level is set to be zero.

To further understand the composition of band structures at CBM and VBM for Janus GaOClX monolayers, partial density of states (PDOS) is also calculated. It is observed that for GaOClF monolayer, CBM is mostly made up of hybridization of Ga_*p*, O_*p*, Cl_*p*, and F_*p* orbitals while VBM is mainly originated from Cl_*p* orbital. In contrast, for GaOClBr or GaOClI monolayers, VBM is mainly occupied by Br_*p* orbital and I_*p* orbital, respectively. Such phenomenon can be understood from the competition of electronegativity between Cl and X atoms.

4.3.3 Carrier mobility of monolayers

Carrier mobility plays an important role in examining the electrical behaviors of 2D materials. According to the results reported in previous works, the parameters that affect carrier mobility of Janus monolayers, such as elastic modulus, are direction dependent. That means they are anisotropic along x- and y-directions in the systems. Based on the effective mass approximation and the electron–acoustic phonon scattering mechanism, the carrier mobility of anisotropic 2D materials can be calculated by the modified formula of the deformation potential (DP) theory, as follows [157]:

$$\mu_x = \frac{e\hbar^3\left(\frac{5C_{11}+3C_{22}}{8}\right)}{k_BT(m_x^*)^{\frac{3}{2}}(m_y^*)^{\frac{1}{2}}\left(\frac{9{E_x}^2+7E_xE_y+4{E_y}^2}{20}\right)} \qquad 4.2$$

$$\mu_y = \frac{e\hbar^3\left(\frac{5C_{22}+3C_{11}}{8}\right)}{k_BT(m_y^*)^{\frac{3}{2}}(m_x^*)^{\frac{1}{2}}\left(\frac{9{E_y}^2+7E_xE_y+4{E_x}^2}{20}\right)} \qquad 4.3$$

where k_B, T, e, and $\hbar$ are the Boltzmann constant, temperature, electron charge, and Planck constant divided by 2π, respectively. E_d is the DP constant, representing the shift of CBM (VBM) for electrons (holes) induced by the applied uniaxial strains. It can be calculated as $d\mathrm{E}_{edge}/d\varepsilon$, where E_{edge} is the energy of the band edges. C_{ij} is the elastic modulus of 2D systems. The effective mass of carrier m^* is defined as $m^* = \pm\hbar^2(\frac{d^2E_k}{dk^2})^{-1}$, where E_k and k stand for the band energy and electron wave vector, respectively. The parameters for Janus GaOClX monolayers are calculated and the results are summarized in Table 4.2.

Table 4.2 Calculated effective mass (m^*), 2D elastic modulus (C), deformation potential constant (E_d), and mobility (μ) of electrons and holes along x- and y-directions at 300 K for the Janus GaOClX (X = F, Cl, and Br) monolayer.

System	Direction	Carrier type	m^*/m_0	C (N/m)	E_d (eV)	μ (cm^2 V^{-1} s^{-1})
GaOClF	x	electron	0.40	55.60	6.17	224.12
		hole	1.63	55.60	2.39	60.99
	y	electron	0.50	39.01	3.32	222.20
		hole	2.24	39.01	2.30	41.39
GaOClBr	x	electron	0.41	59.28	14.89	22.00
		hole	1.39	59.28	11.31	8.82
	y	electron	0.48	50.33	20.82	15.47
		hole	0.87	50.33	19.81	6.43
GaOClI	x	electron	0.41	60.76	24.36	8.15
		hole	0.70	60.76	21.84	4.14
	y	electron	0.51	53.84	34.88	5.40
		hole	0.48	53.84	35.45	4.60

Table 4.2 clearly indicates that almost all effective masses of holes are higher than those of electrons of Janus GaOClX monolayers, except for that of the GaOClI monolayer along y-direction. The results are consistent with the band structures shown in Figure 4.3, where the conduction band is more dispersive and the valence band is comparatively smooth. The calculated results indicate that the GaOClF monolayer exhibits the largest carrier mobility and anisotropy, and its electron mobility is close to

that of its parental GaOCl monolayer and is comparable with that of MoS_2 monolayer (~200 cm^2 V^{-1} s^{-1}) [159]. For Janus GaOClBr and GaOClI monolayers, since they have relatively small effective mass and large E_d, their carrier mobilities could not surpass that of their parental GaOCl monolayer. The results also suggest that among those Janus GaClOX monolayers, GaOClF is a promising candidate of 2D materials used in nanoelectronic and nanophotonic devices.

4.3.4 Mechanical properties of monolayers

The elastic constants of Janus GaOClX monolayers are computed to investigate their mechanical properties. Determined by the structural symmetry of 2D systems, there are four non-zero independent elastic constants C_{11}, C_{12}, C_{22}, and C_{66} with Voigt notations that 1, 2 and 6 stand for xx, yy and xy, respectively. The calculated results of systems are listed in Table 4.3. Mechanical stability can be determined through these values. The elastic constants satisfy the Born–Huang stability criteria [207]: $C_{11}>|C_{12}|$, $C_{11}C_{22}–C_{12}{}^2>0$, $C_{66}>0$, indicating the structural stability of Janus GaOClX monolayers.

Table 4.3 Calculated elastic modulus C_{ij} (N/m) and piezoelectric coefficient e_{ij} (pC/m) and d_{ij} (pm/V) for Janus GaOClX monolayers.

System	C_{11}	C_{12}	C_{22}	C_{66}	e_{11} (d_{11})	e_{12} (d_{12})	e_{31} (d_{31})	e_{32} (d_{32})	e_{26} (d_{26})
GaOClF	56.57	8.06	43.56	25.28	180.88	29.18	13.96	47.85	11.78
					(3.19)	(0.08)	(0.09)	(1.08)	(0.47)
GaOClBr	59.29	12.63	50.33	27.29	89.93	52.88	13.83	12.15	-10.45

					(1.37)	(0.71)	(0.19)	(0.19)	(0.38)
GaOClI	60.76	17.23	53.84	28.36	93.13	13.25	32.25	21.95	-246.58
					(1.61)	(0.27)	(0.46)	(0.26)	(8.69)

On the basis of elastic constants, the in-plane Young’s modulus Y(θ) and Poisson ratio v(θ) as a function of in-plane angle (θ) can be also determined through using the following formula [208]:

$$Y(\theta) = \frac{C_{11}C_{22} - C_{12}^2}{C_{22}\cos^4\theta + A\cos^2\theta\sin^2\theta + C_{11}\sin^4\theta} \tag{4.4}$$

$$v(\theta) = \frac{C_{12}\cos^4\theta - B\cos^2\theta\sin^2\theta + C_{12}\sin^4\theta}{C_{22}\cos^4\theta + A\cos^2\theta\sin^2\theta + C_{11}\sin^4\theta} \tag{4.5}$$

where $A = (C_{11}C_{22} - C_{12}^2)/C_{66} - 2C_{12}$ and $B = C_{11} + C_{22} - (C_{11}C_{22} - C_{12}^2)/C_{66}$.

To investigate the effect of Janus structure on mechanical properties more directly, the corresponding results of their parental GaOCl monolayer obtained by the same method are also depicted. As shown in Figure 4.4(a), the Young’s moduli Y(θ) of GaOCl and Janus GaOClX monolayers exhibit similar features of anisotropy, with the minimum or maximum value occurred along the axial directions or diagonal direction, respectively. Y(θ) for GaOClI shows a gradual increase from the minimum value of 48.95 N/m along y-direction to the maximum value of 64.48 N/m along the direction with θ = 41°, showing the most obvious anisotropy. Moreover, the smallest value of Y(θ) for Janus GaOClX monolayers is 42.41 N/m, occurring along y-direction in Janus GaOClF monolayer. These values are far less than those of many previously reported 2D materials, such as graphene (342 N/m) [207] and MoS_2 (330 N/m) [209], suggesting that Janus GaOClX monolayers could have good flexibility. They can be structurally stable even under large in-plane applied strains.

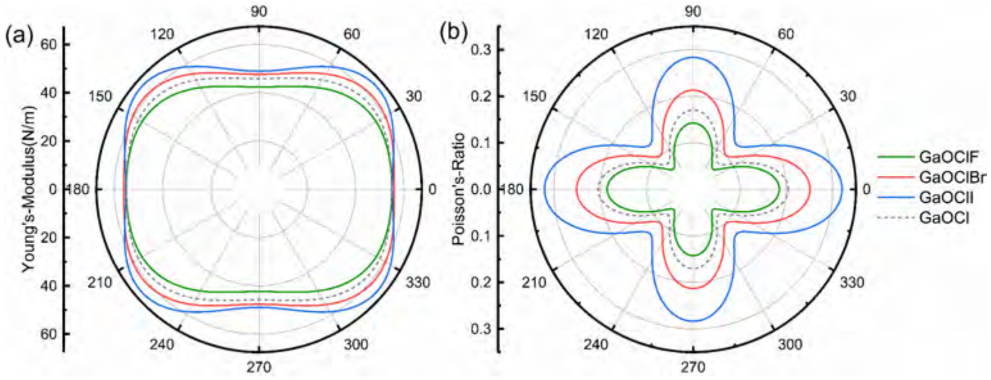

Figure 4.4 The orientation dependent (a) in-plane Young’s modulus, and (b) Poisson’s ratio of the Janus GaOClX (X = F, Cl, and Br) (solid lines) and GaOCl (dotted line) monolayers.

The highest value of Poisson’s ratio ν(θ) occurs along the axial directions, as shown in Figure 4.4(b). The value of ν(θ) also exhibits apparent anisotropy, ranging from 0.06 (for GaOClF) to 0.32 (for GaOClI). The positive value of ν(θ) indicates that the applied tensile or compressive strain could result in the expansion or contraction of Janus GaOClX monolayers, respectively. Previous studies on 2D materials suggest that the lower ν(θ) (< 0.5) the better compressibility of monolayers. Therefore, Janus GaOClX monolayers could be stable under compressive deformation. Compared with those for GaOCl monolayer, the Young’s modulus and Poisson’s ratio dependences on orientation for the as-derived Janus monolayers behave similarly, with their maximum values varied in the trend of GaOClI > GaOClBr > GaOCl > GaOClF. The results of Y(θ) and ν(θ) demonstrate that Janus GaOClX monolayers have strong stability against elastic deformation and high mechanical flexibility.

4.3.5 Piezoelectric properties of monolayers

The asymmetric atomic structures of Janus GaOClX monolayers suggest that they may become polar 2D materials. Since they have no inversion symmetry, multidirectional polarizations could be induced through applied mechanical strains in Janus GaOClX monolayers. Determined by the crystal symmetry of monolayers, there are five non-zero independent piezoelectric coefficients, namely, d_{11}, d_{12}, d_{31}, d_{32}, and d_{26}, which are expressed as follows: $d_{11} = \frac{e_{11}C_{22}-e_{12}C_{12}}{C_{11}C_{22}-C_{12}^2}$, $d_{12} = \frac{e_{11}C_{12}-e_{12}C_{11}}{C_{12}^2-C_{11}C_{22}}$, $d_{26} = \frac{e_{26}}{C_{26}}$, $d_{31} = \frac{e_{31}C_{22}-e_{32}C_{12}}{C_{11}C_{22}-C_{12}^2}$, and $d_{32} = \frac{e_{31}C_{12}-e_{32}C_{11}}{C_{12}^2-C_{11}C_{22}}$. Based on the density functional perturbation theory (DFPT), the non-zero coefficients e_{ij} and d_{ij} can be computed and the results are listed in Table 3. It can be found that the uniaxial in-plane strain (stress) along x- and y-directions can generate in-plane and out-of-plane changes in polarizations of the monolayers. The Janus GaOClF monolayer possess the largest d_{11} coefficient (3.19 pm/V), which is nearly twice as high as that of its parental GaOCl monolayer and is compatible to those of h-BN (0.61 pm/V)[139] and MoS_2 (3.73 pm/V) [45]. With the relatively stable bonding along y-direction, the in-plane coefficient d_{12} is smaller than d_{11}. Generally, the piezoelectricity of 2D materials is utilized by bending the monolayers in devices, emphasizing the significance of out-of-plane polarization since the induced charges are more easily detected and harvested in practical applications. Remarkably, the Janus GaOClF monolayer exhibits the out-of-plane coefficients d_{32} as high as 1.08 pm/V, higher than that of Janus NbOXY monolayers (0.26 ~ 0.55 pm/V) [210]. The d_{31} coefficient of Janus GaOClI monolayer (0.46 pm/V) is also larger than those of most reported 2D materials, such as Janus group-III chalcogenide monolayers (0.07 ~ 0.46 pm/V) [57], Janus BiOX (X = Cl, Br, and I) monolayers (0.10 ~ 0.21 pm/V) [211], and is comparable with those of In_2X_2X' (X and X′ = S, Se, and Te) monolayers (0.43 ~ 0.59 pm/V) [212]. Moreover, its d_{26} coefficient can reach a large value of 8.69 pm/V, meaning that an in-plane shear strain can induce changes in polarization along y-direction. Since the d_{26} coefficient of most previously reported 2D materials is below 1.0 pm/V, the ultrahigh d_{26} of Janus GaOClI monolayer suggests that it is more versatile in its areas of applications, such as sensors, actuators and mechanical energy harvesters.

4.3.6 Dielectric and energy-storage properties of monolayers

For a dielectric material, its ultimate energy-storge density J is a critical parameter, which characterizes its energy storage property and can be evaluated as follows:

$$J = \int_0^{E_{max}} P \, dE \qquad 4.6$$

where E is the external applied electric field and P is the polarization. E_{max} is the maximum field that can be applied to the dielectric without significant current leakage, which could be a measure of its electric breakdown strength. For inorganic dielectrics, E_{max} is closely associated with the intrinsic bandgap of materials that could be diminished under an applied field larger than E_{max}. Equation 4.6 thus implies that high energy-storge density could be achieved with high electric breakdown strength or E_{max} and large electric polarization.

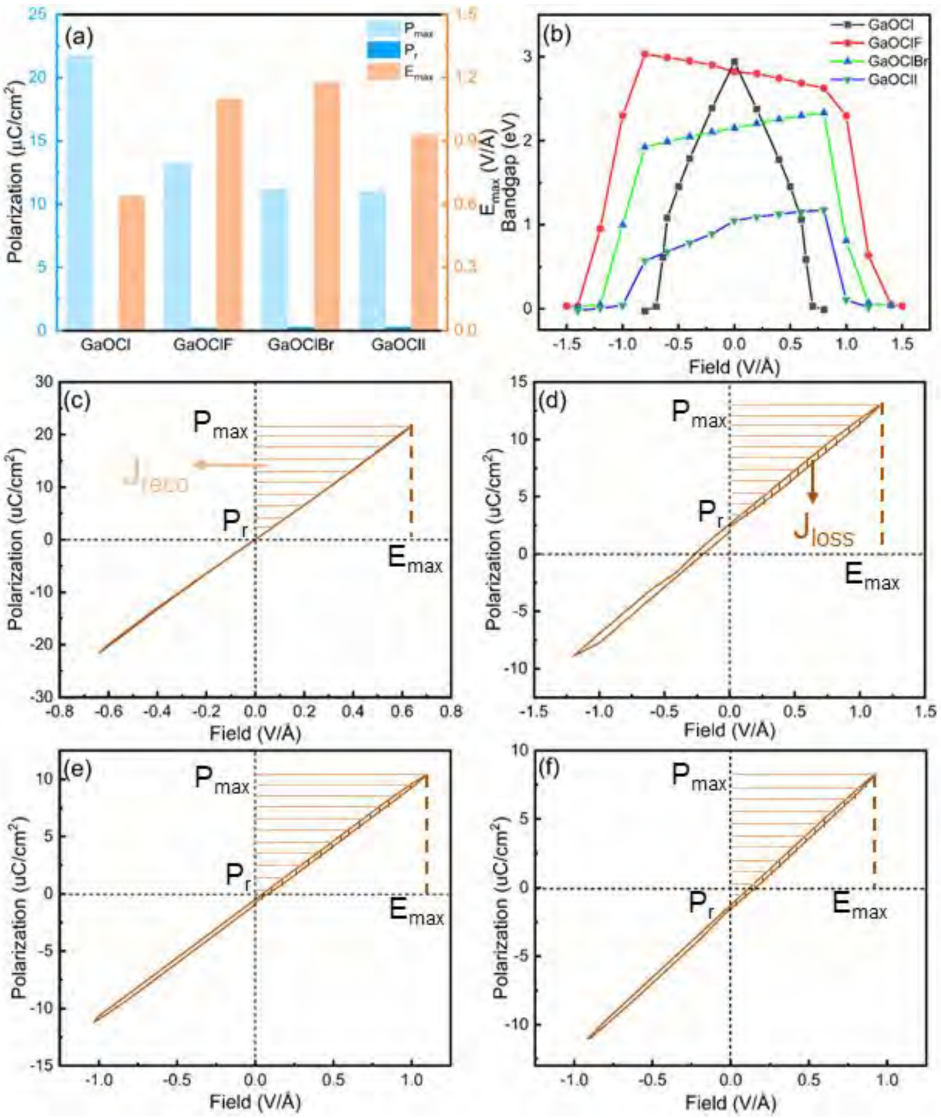

Figure 4.5 (a) The P_{max}, P_r, and E_{max} of systems studied. (b) The changes of bandgap values of systems studied under applied electric fields. The P-E loop of (c) GaOCl, (d) GaOClF, (e) GaOClBr, and (f) GaOClI monolayers. The orange and brown areas represent J_{reco} and J_{loss}, respectively.

As shown in Figure 4.5(a), the value of E_{max} for the GaOCl or Janus GaOClX monolayer is quantitatively determined by studying the influences of applied electric fields on its bandgap. An electrostatic field perpendicular to the monolayer is applied across the vacuum slabs in the supercell. Figure 4.5(b) shows the bandgaps of GaOCl and Janus GaOClX (X = F, Br, and I) monolayers under different applied fields.

Because of structural symmetry along z-direction of GaOCl, the change in the bandgap under a positive (+) applied electric field coincides with that under a negative (−) field. As the applied electric field increases, the bandgap of GaOCl monolayer decreases gradually and tends to disappear at high electric fields, which could drive the monolayer to transform from a semiconductor into a metallic-like monolayer. In this regard, E_{max} can be estimated to be the applied field (0.64 eV/Å) under which the bandgap of monolayer is reduced to 0.1 eV. Similarly, E_{max} for Janus GaOClX monolayers can be determined according to the relation between the bandgap and applied filed shown in Figure 4.5(b). Remarkably, the bandgap of GaOClF monotonously increases (decreases) almost linearly with negative (positive) electric fields ranging from -0.8 to 0.8 V/Å. This change is attributed to the build-in electric field caused by the difference in electronegativity between Cl and F atoms. Under an applied electric field, electrons tend to accumulate at halogen-element atoms with more electronegativity. Therefore, the bandgap dependence on applied field for Janus GaOClBr or GaOClI monolayer behaves oppositely in comparison with that for Janus GaOClF monolayer. For Janus GaOClX monolayers, the bandgap drops abruptly with increasing (absolute values of) applied fields, suggesting that the maximum field E_{max} applied to Janus GaOClX monolayers could be larger than 0.8 V/Å, as listed in Table 4.4 and indicated in Figure 4.5(a).

Table 4.4 The maximum applied field E_{max} (V/Å), polarization P_{max} (μC/cm^2) at E_{max}, remnant polarization P_r (μC/cm^2), recovery energy density J_{reco} (J/cm^3), energy storage density J_{stor} (J/cm^3), and energy storage efficiency η (%) of GaOCl and Janus GaOClX monolayers.

System	P_{max}	P_{r}	E_{max}	J_{reco}	J_{stor}	η (%)
GaOCl	21.77	0.00	0.64	682.43	682.43	-
GaOClF	13.20	0.20	1.18	893.32	951.71	93.86
GaOClBr	10.41	0.25	1.10	516.73	559.87	92.29
GaOClI	8.32	0.27	0.93	301.73	334.49	90.21

The electric field-polarization (P-E) loops for the monolayers are determined by calculating the electric polarizations under the applied field $-E_{max} \leq E \leq E_{max}$, as shown in Figure 4.5(c-f). The results show that the maximum polarization under E_{max} (P_{max} = 21.77 μC/cm^2) is the highest for GaOCl and changes with the monolayers in the order of GaOCl > GaOClF > GaOClBr > GaOClI, as indicated in Figure 4.5(a). The ultimate energy storage density J is then estimated by calculating the numerical integration in Eq. 4.6. During the charging process, the electrical energy J_{stor} is stored in the dielectric capacitor, as represented by the summation of orange and brown areas in Figure 4.5(c-f). Moreover, during the discharging process by reducing the field from E_{max} to zero, the polarization reduces to remnant polarization P_r and the recoverable electrical energy density J_{reco} is released, which is illustrated by the orange areas in Figure 4.5(c-f). In these processes, part of the stored energy, J_{loss} indicated by the brown areas in Figure 4.5(c-f), is exhausted. The computed J_{reco}, J_{stor} and $\eta = J_{reco}/J_{stor}$ are listed in Table 4.4. The recoverable energy storage densities J_{reco} for the monolayers are one order of magnitude higher than those of thin-film dielectrics

[100, 190, 191]. Especially for Janus GaOClF monolayer, J_{reco} is as high as 893.32 J/cm^3, which is compatible to those of electrochemical supercapacitors. In addition, all monolayers show high energy storage efficiency (> 90 %).

Although the Janus GaOClX (X = F, Br, and I) monolayers are predicted by first-principles calculations, they could be practically derived from the as-exfoliated GaOCl monolayer through a facile synthesis route that replacement reactions occur among halogen elements. Moreover, dielectric capacitors made up from the as-predicted Janus GaOClX monolayers with atomic thicknesses could be viable since the transfer of monolayers to a conductive substrate and the formation of electrodes on the top surface of monolayers are currently routine operations in micro- or nano-electronic industry. Therefore, it is expected that the application of Janus GaOClX (X = F, Br, and I) monolayers as dielectric layers in capacitors is implemented by experimental work in the near future.

4.4 Conclusions

In summary, Janus GaOClX (X = F, Br, and I) monolayers are systemically investigated based on first-principles calculations. The monolayers exhibit structural and thermal stability and are 2D semiconductors with indirect bandgaps of 2.18 ~ 4.36 eV. They possess anisotropic carrier mobility, strong mechanical flexibility and excellent out-of-plane piezoelectricity. The dielectric properties of GaOCl and Janus GaOClX monolayers are evaluated. The monolayers are found to have superior energy storage properties with the energy storage densities as high as 893.32 J/cm^3 and the the energy storage efficiencies larger than 93.86%, resulting from their high saturated polarization, low remnant polarization, and ultrahigh electric breakdown strength. Therefore, the GaOCl monolayer and the as-derived Janus GaOClX monolayers are promising candidates of dielectric materials used in dielectric capacitors, which have ultrahigh energy storage densities compatible to those of electrochemical supercapacitors and batteries. This work provides theoretical guidelines in searching for novel dielectric materials, which are much desirable for energy storage devices with small dimensions, superior energy storage density and power density, excellent efficiency and thermal stability.

Chapter 5 Doping-induced magnetism in 2D monolayers

5.1 Doping-induced magnetism in 2D Janus TiXO (X = S, Se) monolayer

5.1.1 Introduction

The 2D magnets, an indispensable family of 2D multifunctional materials, have aroused much interest in data storage, computing, spintronic devices [213] and are promising materials in next-generation information technology. In recent years, numerous intrinsic 2D magnetic semiconductors have been reported in theorical work, including chromium trihalides (CrX_3, X= F, Cl, Br, I) [69, 214], H-phase transition metal dihalide MX_2 (M = Cr, Mo, V, Mn, Co, W and X = S, Se, Te) [215], MXenes [216, 217], $CrATe_3$ (A= Si, Ge and Sn) [73, 218], transition metal chloride (TMCl; TM = Sc, Y, Zr) [219], rare-earth halides (GdI_2) [220], MnNX and CrCX (X = Cl, Br, I; C = S, Se, Te) monolayers [221, 222]. Nevertheless, there are a limited number of magnetic candidates that have been discovered in experiments. In 2017, the long-range magnetic order was experimentally revealed in $Cr_2Ge_2Te_6$ bilayer [74] and CrI_3 monolayer [72], with low critical temperatures (T_C) of 28 K and 45 K, respectively. Since then, magnetic $CrCl_3$ [223], $CrBr_3$ [224], Fe_3GeTe [78], and VSe_2 [85] monolayers have been successfully synthesized. However, most of them have the T_C below room temperature, restricting their multi-functional practical applications. Therefore, searching for 2D systems with room-temperature magnetisms is appealing as they will promote the development of micro-multifunctional electronic devices.

Since many 2D semiconductors are absent of spin ordering, it is a viable strategy that the magnetisms could be induced to nonmagnetic 2D materials, solving the problem of few intrinsic magnetic systems available. Various attempts have been focusing on defect engineering, including certain vacancies [225], dopants of magnetic atoms [226, 227] and adsorption [97, 228]. Through this method, besides the uncontrollability of defects distributions, it is also challenging to realize the strong magnetism and avoid the scattering effects of defects [229]. Alternatively, carrier doping is a desirable method to achieve tunable magnetisms without the aforementioned disadvantages. 2D materials with flat band edges endow a lot number of states of density concentrate on a relative narrow energy range, leading to the electronic instability. Such electronic properties could be regulated by band engineering in increasing carriers and shifting the Fermi level, leading to the probability of phase transition like magnetism. Carrier doping is an effective method to stimulate such 2D magnetisms. This way does not induce structural imperfections and can be simply implemented through modulation of gate voltages. By hole doping to GaSe monolayer, Cao *et al.* predicted the ferromagnetic phase transition and half-metal state in the 2D material [88]. In the work of buckled phosphorene and arsenene reported by Fu *et al.*, a stable ferromagnetic state at room-temperature was found to emerge in a wide range of hole densities [179]. Liu *et al.* reported the hole-doping induced magnetism in ferroelectric α-In_2Se_3 with high T_C, serving as a feasible method for designing 2D multiferroics [89]. Moreover, GaO [230], InO [230], SnO [87, 231], InP_3 [90] have been studied in terms of doping induced tunable magnetism. In general, most of the studies mentioned above are based on monatomic or binary compounds, clarifying the significance of carrier-doping magnetism.

Recently, 2D materials with Janus structures are widely investigated due to their high performance in electronics, photocatalysis and energy conversion. At present, Janus MoSSe monolayer has been prepared successfully from MoS_2 or $MoSe_2$ through substituting atomic layer at one side [100, 232]. Theoretically, 2D $Cr_2X_3S_3$ (X = Br, I) Janus semiconductors is predicted to have intrinsic room-temperature magnetism [233], broadening the candidates for spintronic nano-devices. It is envisaged that, through embedding transition-metal atoms, Janus MoSSe could transform to magnetic ground states [234]. For example, Liu *et al.* reported that the magnetism in Janus PA_2As (A = Si, Ge, Sn, and Pb) monolayers with a low T_C of 93.5 K could be induced by carrier doping [235]. TiXO (X = S, Se) monolayers, containing transition-metal Ti atom but nonmagnetic, has been predicted as potential candidate for photocatalysts with suitable bandgap [236]. Due to the absence of inversion symmetry, they also possess good piezoelectric properties [236]. Here, doping-induced magnetism is an interesting field to be exploited.

In this work, we study the electronic and spontaneous magnetism of electron doping TiXO (X = S, Se) monolayers using first-principles calculations. The relatively flat band structures from Γ to M points lead to electronic instability. Remarkably, with a tiny doping density, TiSO and TiSeO monolayers exhibit magnetic ground states with positive spin polarization energy and their T_C are estimated to be above the room temperature. Besides, the effects of external strains and numbers of layer on the doping-induced magnetism are evaluated. The results indicate that Janus TiXO (X=S, Se) monolayers are promising 2D magnets for novel electronic and spintronic applications.

5.1.2 Computational details

In this work, the first-principles calculations based on the density functional theory (DFT), were implemented by using the Vienna *Ab initio* Simulation Package (VASP) [118, 237, 238]. The projector-augmented wave (PAW) pseudopotential was chosen to treat electron-ion interactions and the generalized gradient approximation (GGA) as parameterized by the Perdew−Burke−Ernzerhof (PBE) form was used to describe the exchange correlation functionals [113, 239]. Considering corrections on the strong correlation of Ti 3*d*-electrons, spin-polarized GGA+U calculations [240, 241] were applied and the on-site Coulomb term U was chosen to be 4.2 eV [242-244]. In order to obtain a more accurate bandgap, Heyd-Scuseria-Ernzerhof (HSE06) [143] functional was employed to calculate the electronic structure. We added a vacuum space of 15 Å along z-direction to avoid the interaction between the periodic images. The cutoff energy was set to be 500 eV and the lattice geometry was optimized until the total forces on each atom were below 0.01 eV/Å and energy fluctuations were below 10^{-6} eV. The Brillouin zones were sampled by 15×15×1 and 23×23×1 Γ-centered K-grid meshes in the Monkhorst-Pack scheme [142] for the geometry optimization and electronic structure calculations, respectively. The long-range vdW interactions were corrected by the Grimme's DFT-D3 method [147]. In the carrier doping calculations, a jellium background with an opposite charge is added to maintain charge neutrality.

5.1.3 Results and discussion

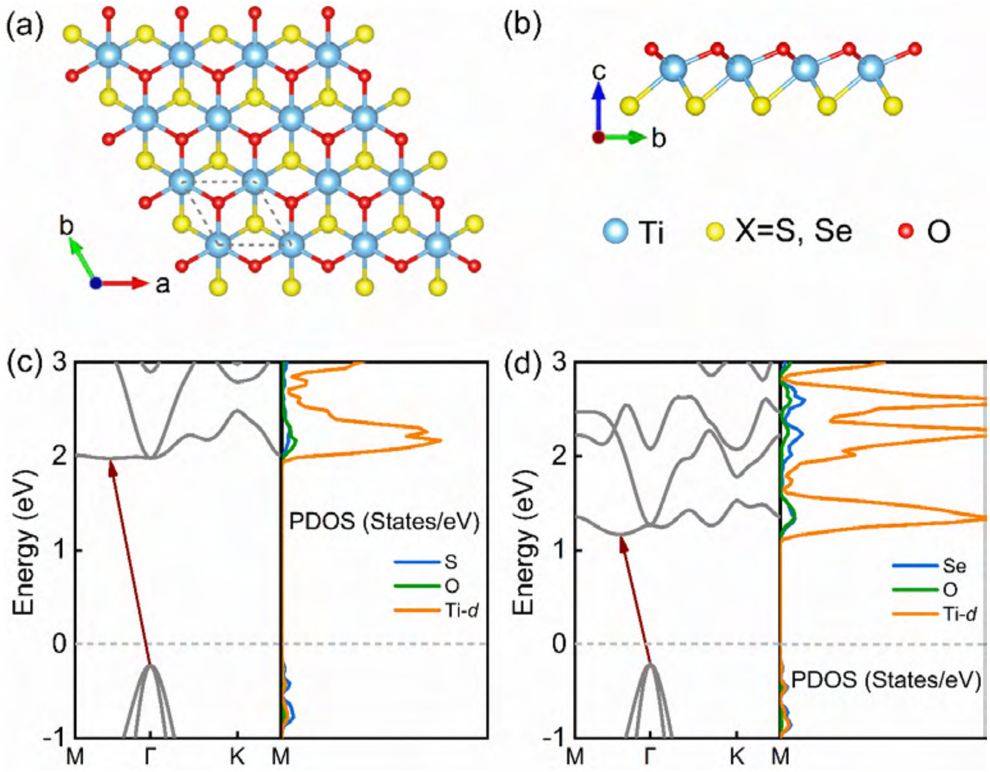

Figure 5.1 (a) Top view and (b) side view of TiXO (X = S, Se) monolayers. Hexagonal unit cell is indicated by a dotted gray line. The band structures and PDOS calculated using HSE06 functional for (c) TiSO and (d) TiSeO monolayers. The Fermi energy is set as zero.

The lattice of TiXO (X = S, Se) monolayers could be obtained from TiX_2 monolayer by replacing one layer of S or Se atoms with O atom, as reflected in the successful preparation of MoSSe monolayer in experiment [100]. Considering the diversity in lattice structures, the possible 1H and 1T stacking types and lower-energy 1T lattice structure are selected to perform the calculations, in consistent with the TiX_2 parent phase [245, 246] and previous theoretical data [236]. Figure 5.1(a) and (b) show the corresponding 2D Janus structures. From the top view, the hexagonal unit cell contains one six-fold Ti, one three-fold X and one three-fold O. Obviously, Ti layer is sandwiched between X and O layers and X is not aligned over O layer along different directions. This lattice arrangement inevitably breaks the out-of-plane symmetry and the lattice belongs to polar $P3m1$ (No. 156) space group. The fully optimized lattice parameter a = 3.22 and 3.28 Å for TiSO and TiSeO monolayers are chosen, respectively, which is agree well with previous report [236]. Due to the differences in atomic size and electronegativity between sulfur and selenium atoms, TiSO monolayer possesses a layer thickness (2.40 Å) smaller than that of TiSeO monolayer (2.51 Å). The structure involves two equal covalent bonds and the bond length of Ti-O bond and Ti-S (Se) bond is 2.03 Å (2.04 Å) and 2.44 Å (2.57 Å), respectively, for TiSO (TiSeO) monolayer. The structural parameters are listed in Table 5.1. Besides, the dynamical, thermodynamical, and mechanical stability of TiXO monolayers is confirmed as well and the details are shown in the supporting information.

Table 5.1 Optimized lattice constant, thickness, bond length, and calculated HSE06 bandgap of TiSO and TiSeO monolayers.

System	Lattice *a* (Å)	Thickness (Å)	Ti-O (Å)	Ti-S (Se) (Å)	Bandgap (eV)
TiSO	3.22	2.40	2.03	2.44	2.20
TiSeO	3.28	2.51	2.04	2.57	1.38

With the credible geometric constructures for TiXO (X = S, Se) monolayers, we now focus on their intrinsic electronic properties. In order to predict more accurately on the band structures, the HSE06 calculations are employed. Because of the existence of Ti atoms, the effect of spin orbital coupling (SOC) is examined firstly. In this work, it is found that effects of SOC on the calculated results are negligible, and the results described in the following sections are obtained without considering SOC. The calculated band structures and projected density of states (PDOS) are shown in Figure 5.1(c) and (d), respectively, resemble with each other as a whole for TiSO and TiSeO monolayers. Clearly, TiSO monolayer is an indirect-bandgap semiconductor with a HSE06 gap of 2.20 eV. The VBM is located at the Γ point while the CBM lies halfway from M to Γ point. It is worth noting that the energy difference between indirect bandgap and direct bandgap at Γ point is smaller than 1.5 meV. In addition, the consideration of on-site Coulomb term HSE+U results in the similar band structures while there is a larger band gap as compared with that in previous work [236]. From Figure 5.1(c), the corresponding PDOS in the right column further illustrates the main contribution of Ti 3d-orbital for CBM and the hybrid effects of Ti, S, and O atoms for VBM. For TiSeO monolayer, similar indirect bandgap (1.38 eV) and features of band structures are also obtained. Interestingly, the total density of states (DOS) for both TiXO monolayers increase sharply at the CBM, resulting from the relatively flat conduction band edge along the Γ-M direction. Such large DOS near the Fermi level would cause the electronic instability and thus provide the possibility to develop novel electronic properties [247, 248]. In general, appropriate carrier doping could trigger the spontaneous ferromagnetism in the 2D systems with such band edges [88, 90, 179, 248], which will be mainly exploited in this work.

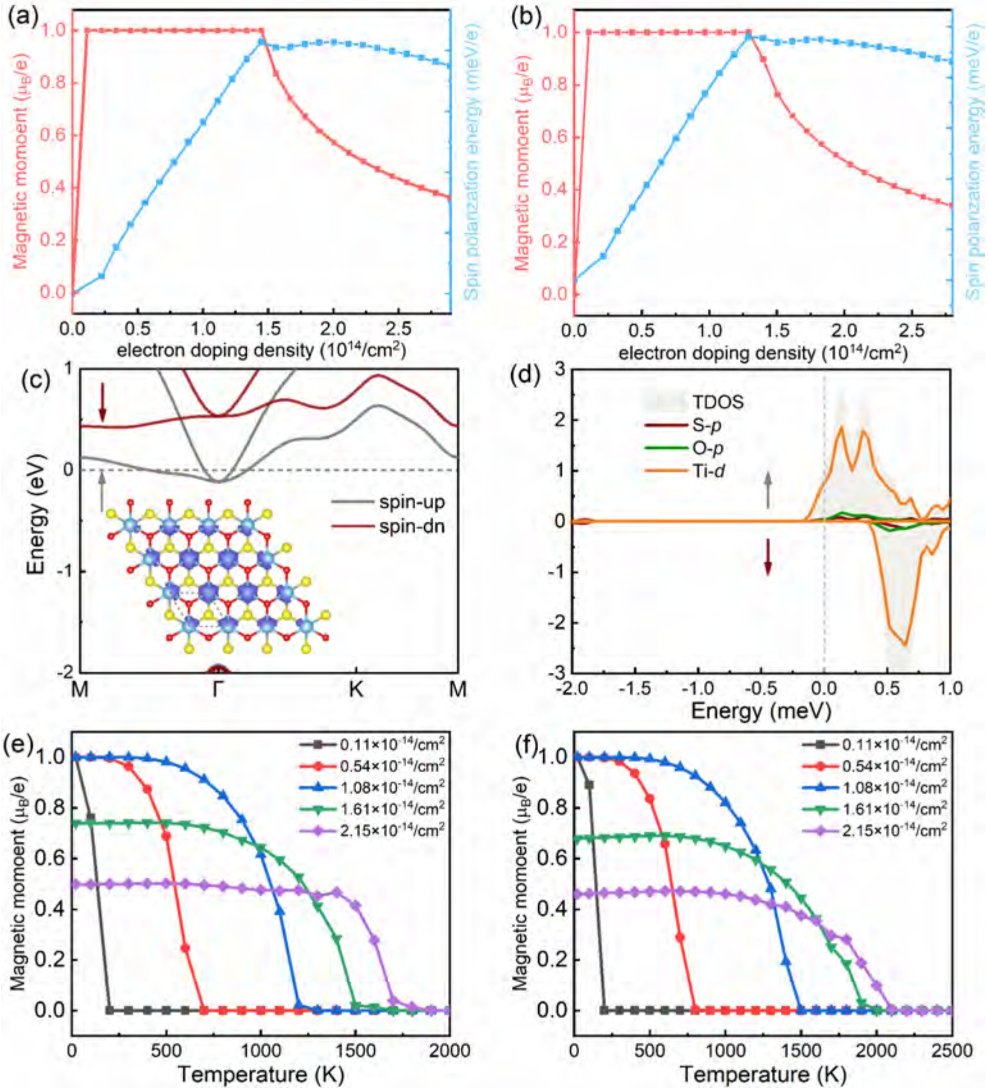

Figure 5.2 The magnetic moment and spin polarization energy per electron as a function of doping density for (a) TiSO and (b) TiSeO monolayer. (c) Band structure and (d) PDOS of TiSO monolayer at a doping density n = 1.08×10^{14}/cm^2; the inset is the spin density at the same condition. The spin magnetic moment as a function of temperature for (e) TiSO and (f) TiSeO monolayer at different doping density.

Due to the nearly flat dispersion and high density of states appeared individually at conduction band while the valence band is dispersive, herein, we only consider the electronic instability induced by the exchange interaction resulting from electron doping. In the process of electron doping, the carrier density is controlled through changing the total number of electrons in the primitive cell. The opposite charges will be added as compensating background to keep neutrality. This process can also be interpreted as the application of an external electric field to the system, introducing electrons to it. At zero doping ($n = 0$, where n represents the density of electron doping), the pristine TiSO and TiSeO monolayers are non-magnetic semiconductors. As expected, electron doping could introduce the ferromagnetism in these two systems. To investigate the stability of magnetization, we examine the magnetic moment and spin polarization energy (E_p) as a function of electron-doping density. Here, E_p is defined as the difference in total energy per electron between ferromagnetic and nonmagnetic phases, where a positive value indicates the preference and stabilization of the ferromagnetic state. As shown in Figure 5.2(a) and (b), the magnetic moment of TiSO and TiSeO monolayers could rapidly reach a saturated state with a tiny doping. The magnetic moment reaches a constant value with 1.00 μ_B per electron. To be specific, 100 % spin polarization appears at a critical doping density of $n = 2\times10^{13}/\mathrm{cm}^2$ (0.002 electron per unit cell) and $n = 1\times10^{13}/\mathrm{cm}^2$ (0.001 electron per unit cell) for TiSO and TiSeO monolayers, respectively. Such low magnetism-emerging doping level is comparable with that of α-In_2Se_3 [89], PSn_2As and PPb_2As monolayers [235]. The magnetic moment per electron is closely relevant to the electron-doping concentration n. With increasing doping level, the magnetic moment is still saturated with a fully spin-polarized state during a wide range of n, up to $n_0 = 1.45\times10^{14}/\mathrm{cm}^2$ (0.13 electron per unit cell) and $1.40\times10^{14}/\mathrm{cm}^2$ (0.12 electron per unit cell) for TiSO and TiSeO monolayers, respectively. Meanwhile, their spin polarization energy increases monotonically with increasing n and the maximum value occurs at about 62.11 and 72.06 meV per electron for TiSO and TiSeO monolayers, respectively. These values are an order of magnitude larger than those of 2D GaSe [88] and C_2N [229], and is comparable with that of γ-GeSe [249]. The positive E_p suggests that ferromagnetic ground states of doped TiXO monolayers are stable with $n < n_0$. When the doping concentration exceeds n_0, the magnetic moment drops suddenly with further increment of n and tends to decrease gradually. The spin polarization energy E_p also shows a downward trend.

Normally, carrier doping would lead to the transformation of electronic properties and the resulting ferromagnetism breaks the time-reversal symmetry as well. Without electron doping, the spin-up and spin-down bands overlap closely and the systems are nonmagnetic. However, the spin splitting occurs as the electrons are introduced into the system. Namely, the spin-up bands shift down and the spin-down bands shift up, causing a minority-spin gap. In Figure 5.2(c), we plot the typical spin-polarization band structure of TiSO monolayer at the doping density of $n = 1.08\times10^{14}/\text{cm}^2$ (about 0.1 electron per unit cell) as an example. It can be observed that energy splitting of the conduction band is about 0.65 eV between two spin states. Such splitting appears around the Fermi level results from the strong exchange interaction, leading to the ferromagnetic states. Compared with pristine TiSO monolayer, electron doping gives rise to the upward shift of Fermi level. In this situation, spin-down bands above Fermi energy are not occupied, demonstrating an insulating state. In contrast, the spin-up channels across the Fermi level, leading to spontaneous magnetization and a metal characteristic. This half-metal property is beneficial for spintronic devices. At the same time, the relatively flat spin-polarized band implies the strong localization of electron states, indicating that the magnetic moment is localized as well. As shown in the inset of Figure 5.2(c), the spin density isosurface, obtained by calculating the difference between spin-up and spin-down densities, indicates the dominate contribution of Ti atoms to the nonmagnetic-ferromagnetic transition. The spin-resolved PDOS in Figure 5.2(d) also illustrates such phenomenon, which is beneficial to polarized spin transport. We can see that the hybridization of Ti-*d*, O-*p*, and Se-*p* orbital occurs at the Fermi level, indicating their stronger coulomb interaction. Moreover, the valence of Ti^{4+} changes and thus a small doping density of electron could induce the half full state of 3d orbital of Ti atom. At the doping range $n < n_0$, the spin splitting increases with the increasement of doping density. The system is in a high spin state. While at the doping range $n > n_0$, the adding electron breaks this half full state and the difference between spin-up and spin-down states decrease. The system tends to the low spin states. This phenomenon elaborates the relationship between doping density and magnetic moment, which is consisted with the depiction in Figure 5.2(a) and 5.2(b).

We also qualitatively examine the probability of doping-induced magnetism in terms of physical origin. As we known, the spontaneous magnetization tends to occur if the Stoner's criterion is fulfilled after electron doping, namely $N(E_F)I > 1$ [250], Where $N(E_F)$ is the DOS at the Fermi energy in the nonspin states and I is the Stoner constant. At the case of $n = 1.45\times10^{14}/\text{cm}^2$ for TiSO and $n = 1.40\times10^{14}/\text{cm}^2$ and TiSeO monolayer, $N(E_F)$ are measured as 0.75 and 1.11, respectively. I is defined as the ratio between spin splitting energy Δ_{xc} and magnetic moment M of the unit cell. For TiSO monolayer, $\Delta_{xc} = 0.65$, $M = 0.10$, and $I = 6.50$; for TiSeO monolayer, $\Delta_{xc} = 0.67$, $M = 0.10$, and $I = 6.70$. Obviously, the criterion $N(E_F)I > 1$ is satisfied well and thus electron doping could generate self-magnetization for TiXO systems.

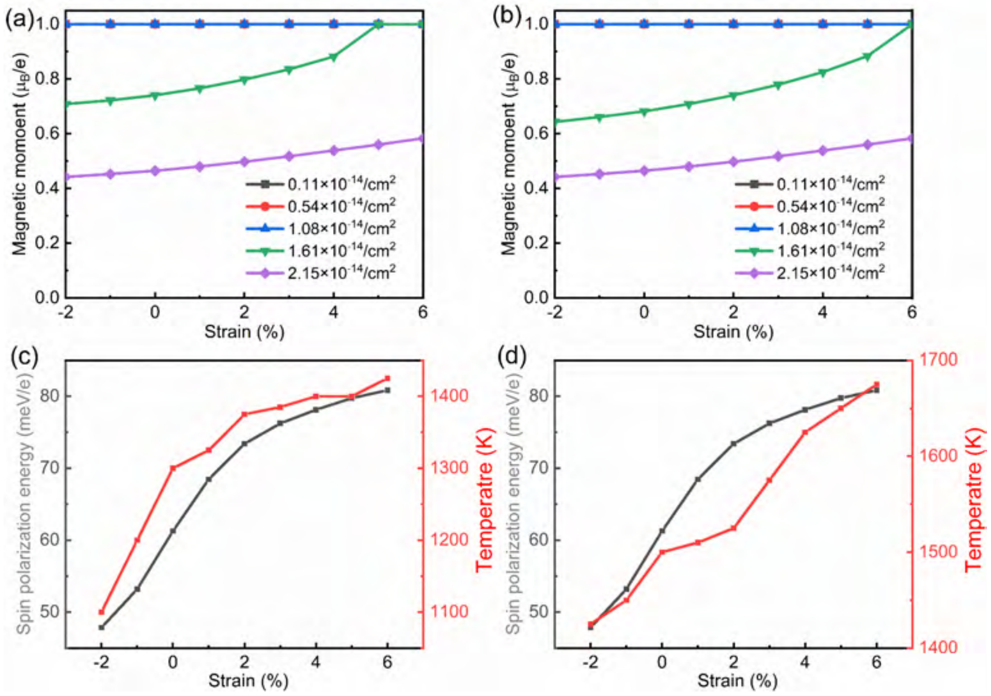

Figure 5.3 Effects of strains on magnetic moments for (a) TiSO and (b) TiSeO monolayers. Effects of strains on spin polarization energy and TC for (c) TiSO and (d) TiSeO monolayers.

In addition, whether the itinerant ferromagnetism in doped TiXO monolayers could be thermodynamically stable is also a critical issue, which can be determined directly by the ferromagnetic transition temperature (T_C). Since the electrons satisfy the Fermi-Dirac distribution as described by the function $f\left(\frac{\epsilon-\mu}{\sigma}\right) = \frac{1}{\exp\left(\frac{\epsilon-\mu}{\sigma}\right)+1}$, where μ is chemical potential, the finite temperature T could be estimated through adjusting the smearing factor $\sigma = k_B T$ and minimizing the free energy [178]. Herein, different electron doping concentration are chosen to describe the relationship between magnetic moment and T, as shown in Figure 5.2(e) and (f) for TiSO and TiSeO monolayers, respectively. At the low doping level, such as $n = 0.11\times10^{14}/\text{cm}^2$, the magnetic moment decreases from 1.00 μ_B per electron to zero with increasing T. The calculated T_C are about 230 K for TiSO and TiSeO monolayers, respectively. Gradually, T_C exceeds room temperature with increasing doping density. At $n = 1.08\times10^{14}/\text{cm}^2$, the fully spin-polarized states could be maintained well above room temperature and estimated T_C reaches 1300 K (1500K) for TiSO (TiSeO) monolayer. In other words, doped TiXO monolayers possess stable ferromagnetic above the room temperature, which are comparable with many hole doping systems, such as buckled phosphorene and arsenene [179], iodinene [251], and α-In_2Se_3 [89].

It is known that physical properties of ultrathin 2D monolayers are easily modulated by external strains. The original buckling configurations of Janus TiXO monolayers make it possible to alternate their physical properties by the strains as induced by the substrate. In terms of the doping-induced ferromagnetism, we examine the influence of applied strain in a small range (from -2 % to 6 %). As shown in Figure 5.3(a), for TiSO monolayer with $n < 1.45\times10^{14}/\text{cm}^2$, 100 % spin-polarized states are well maintained under an applied compressive or tensile strain; While for TiSO monolayer with $n > 1.45\times10^{14}/\text{cm}^2$, its magnetic moment can be enhanced (suppressive) under increasing applied tensile (compressive) strains. With 6% tensile strain, the magnetic moment tends to a saturation value. This phenomenon can be understood from the band structures. Under the tensile strain, the flatter conduction band near the Fermi level occupies the larger parts of Brillouin zone. That means the electronic instability will be greater and the electron doping could enhance the ferromagnetism. For TiSeO monolayer, similar strain dependence of magnetic moment can be observed due to the similar electronic properties, as shown in Figure 5.3(b). Meanwhile, the spin polarization energy and T_C are also influenced by the applied strains. Their dependences on the strain for TiSO and TiSeO monolayers at a doping density of n = 1.08×10^{14}/cm^2 are illustrated in Figure 5.3(c) and (d). Obviously, the compressive strain reduces the spin polarization energy and T_C whereas the tensile strain enhances them. Under applied tensile strains of 0 – 6 %, the spin polarization energy for TiXO monolayers increase by 30% and T_C increases from 1000 K to 2000 K. With 6 % tensile strain, T_C reach 1425 K and 1675 K for TiSO and TiSeO monolayer, respectively. The tensile-strain enhanced high T_C for TiXO monolayers could be reasonable since ferromagnetic ground states are more favorable under increased tensile strains, resulting in larger magnetic moments as shown in Figure 5.3(a-b) and thus higher T_C.

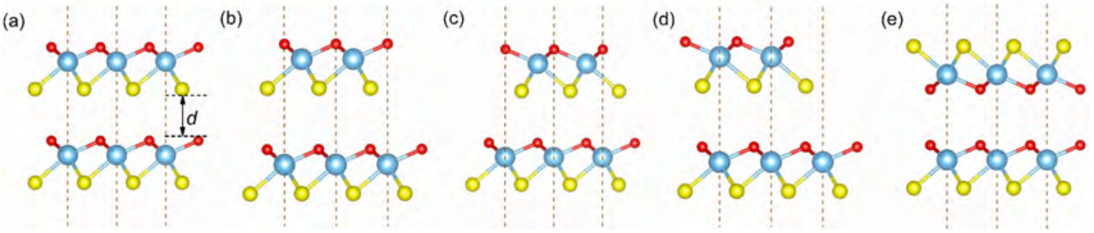

Figure 5.4 Five different possible stacking configurations for TiXO (X = S, Se) bilayers: (a) AA; (b) AB; (c) r-AA; (d) r-AB; (e)A’A.

In order to investigate how the interlayer-interaction influence the doping-induced ferromagnetism, we investigate typical bilayer structures. They could be feasibly prepared by mechanical exfoliation methods for 2D systems [232]. Generally, the layers are connected by van der Waal interactions in Janus multilayers [100, 232]. Herein, five different stacking configurations (AA, AB, r-AA, r-AB, and A'A) are considered. The corresponding fully optimized structures are displayed in Figure 5.4. The interaction between two layers is characterized by the distance *d* along the *z* direction. Among them, two reverse types of in-plane orientation, parallel (AA and AB) and antiparallel (r-AA, r-AB) arrangement, are discussed. All stacking orders have a characteristic in common except the A'A in Figure 5.4(e), i.e., the O-layer is arranged above the Ti-layer while the S (or Se)-layer is underneath the Ti-layer. Consequently, the vertical polarity does not be altered in these four stacking configurations. Specially, the top layer and bottom layers show a mirror symmetry along the z-direction in the A'A configuration. The stability of multilayers is assessed using the binding energy E_b defined as $E_b = \frac{E_n - nE_{monolayer}}{S}$, where E_n ($E_{monolayer}$), n, S are the total energy of Janus TiXO multilayer (monolayer), the number of layers and the area in *x-y* plane, respectively. The negative value means that it is energetically favorable to form the multilayers through the advanced techniques.

Table 5.2 Lattice constant a, interlayer distance d, and binding energy E_b of optimized structures with five possible stacking orders for TiXO (X = S, Se) bilayer.

	a (Å)	*d* (Å)	E_b (meV/Å^2)	a (Å)	*d* (Å)	E_b (meV/Å^2)
		TiSO bilayer			TiSeO bilayer	
AA	3.22	2.95	-21.63	3.27	3.05	-22.82
AB	3.22	3.30	-17.04	3.27	3.41	-17.93
r-AA	3.22	2.97	-21.20	3.28	3.07	-22.17
r-AB	3.21	3.30	-17.08	3.27	3.41	-18.03

A’A	3.21	3.12	-16.93	3.27	3.17	-16.81

The calculated lattice constant *a*, interlayer distance *d* and binding energy E_b of bilayer structures are listed in Table 5.2. There are various degrees of disparity for different structures. According to the results, the structure with directly vertical stacking and without in-plane slip (AA) exhibits the smallest interlayer distance (2.95 Å) and the lowest E_b. Therefore, the AA configuration is the most stable stacking order for bilayer TiSO and TiSeO, in consistent with the ground states in TiS_2 [245, 252] and $TiSe_2$ bulks [246].

The band structures of Janus TiXO bilayers at the HSE06 level are shown in Figure 5.5(a) and (b). Compared with TiXO monolayers, the TiXO bilayers exhibit indirect but smaller bandgaps (1.5 and 1.0 eV for TiSO and TiSeO bilayers, respectively). Such reduced bandgap in bilayer structures can be found in many 2D systems [155, 253, 254]. It is because that the energy of VBM is almost a constant while that of CBM decreases as the layer number increases. Interestingly, the original VBM and CBM are contributed by different TiXO layers if they are defined to be the top and bottom ones, typically reflecting the features of type-II heterojunction band structure. Such electronic properties can be found in polarized In_2X_3 (X = S, Se) [255] and Ga_2O_3 [168] bilayers. Because there are polarizations induced by the broken centro-symmetry in the bilayers, a built-in electric field could exist and the atoms in different layers may experience different electric potentials. Notably, the bottom conduction band of bilayers, originating from the top TiXO layer, still shows the characteristic of flat band structures similar with those in the monolayers.

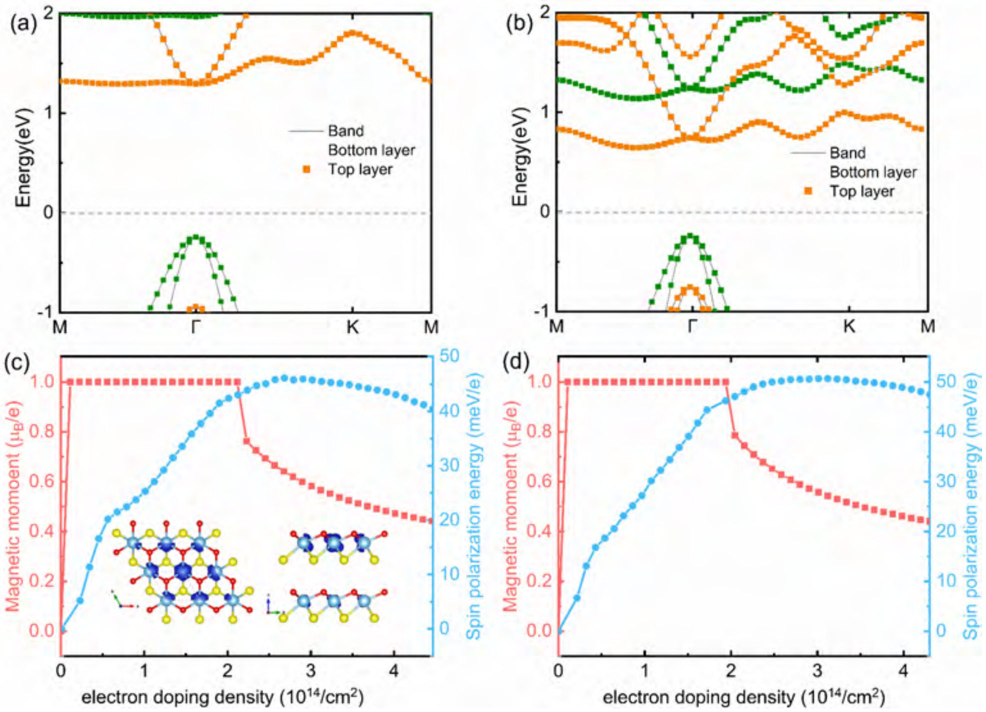

Figure 5.5 The band structures of (a) TiSO and (b) TiSeO bilayer calculated on HSE06 level. The magnetic moment and spin polarization energy as a function of doping density for (c) TiSO and (d) TiSeO bilayers. The inset is the spin density at n = 1.08×10^{14}/cm^2 for TiSO bilayer.

Electron-doping induced ferromagnetisms in the bilayer systems are investigated by increasing the doping. As shown in Figure 5.5(c) and (d) for TiSO and TiSeO bilayers, respectively. Clearly, the 100 % spin-polarized states with a magnetic moment of 1.00 μ_B/electron also can be stimulated with a relative low doping density, about the order of 10^{13}/cm^2. Different with multilayer α-In_2Se_3 [89] and bilayer iodine [251], the increase of the number of layers does not reduce the magnetism induced by low-concentration doping. It is caused by the combined effects of interlayer interaction and the built-in electric field in the TiXO bilayers. Besides, the fully ferromagnetic states can be maintained in a wider range of doping density (from 1×10^{13}/cm^2 to 2.12

$\times 10^{13}$/cm^2 and 1.93$\times 10^{14}$/cm^2 for TiSO and TiSeO bilayers, respectively) than those for monolayers. It can be found that the spin polarized energy monotonically increases with doping concentration, demonstrating the stability of doping-induced magnetisms in the bilayers. From the spin density shown in the inset of Figure 5.5(c), we can see that the magnetic moment mainly accumulates in the Ti atoms at the top layer, instead of evenly distributing in the space. This phenomenon is due to the inherent polarity and consistent with the characteristics of band structures as shown in Figure 5.5(a) and (b). Furthermore, the magnetic moments induced by electron doping in trilayer, tetra-layer, and penta-layer structures are evaluated at different doping levels. Generally, with increasing number of layers, the interaction between the adjacent layers from the bottom to top layers is weakened gradually. The roles of polarity are found to be the most dominant in the systems with three or four layers, while the magnetic moment of the system is still contributed from Ti atoms in the top layer. Consequently, the magnetic moment increases to a certain extent and then decreases with increasing number of layers.

5.1.4 Conclusions

In summary, based on the first-principles calculations, we systematically investigate the electronic properties and carrier-doping induced magnetic properties for Janus TiXO (X = S, Se) monolayers and multilayers. Due to the flat band edge of conduction band along Γ-M path, there is high peak in density of states near the Fermi energy. Electron doping gives rise to the transition from nonmagnetic to magnetic ground states and leads to half-metal property. Besides, estimated T_C are above the room temperature. The doping-induced magnetism can be modulated effectively by the external strain and number of layers. Our study provides a type of Janus ternary compounds for multifunctional electronics and spintronics devices.

5.2 Doping-induced magnetism in 2D Janus XYP_2 (X/Y= Si, Ge, Sn, and Pb; X≠Y) monolayer

5.2.1 Introduction

Since the discovery of graphene in 2004, 2D materials have aroused much attention due to their excellent physical and chemical properties, which are promising for applications in electronics, sensors, energy conversion, and photonics. Although graphene has been fabricated into several nano-devices that exhibit high performance in electronics, its zero bandgap has restricted graphene from wide-spread practical applications. Therefore, numerous novel 2D systems have been developed, such as h-BN, TMDs, MXenes, and transition metal oxides. Among those 2D materials, Janus monolayers, whose name originates from the Roman God, have stimulated a great surge of scientific interest. They have two different faces in their particular 2D structures and exhibit distinct properties, such as piezoelectric, photoelectric and photocatalytic properties, and Rashba splitting effect [95, 96]. Graphone is the first Janus material obtained by replacing half of the H atoms in H-graphene, showing the ferromagnetism and a bandgap of 0.46 eV [97]. The graphene-based Janus structures are also reported to exhibit piezoelectric properties [46]. In experiments, it is feasible to fabricate those Janus structures by surface covalent functionalization [99]. Similarly, other 2D systems with Janus structures such as Janus TMD have been developed. For example, the Janus MoSSe monolayer was synthesized successfully by bottom-up methods, replacing the utter-layer S with Se atoms in the MoS_2 monolayer [100]. Particularly, those 2D Janus structures are found to have outstanding piezoelectricity [256], and photocatalytic properties [96]. Due to their excellent physical and chemical properties and accessible synthesis routes, it is necessary to explore novel 2D Janus materials in response to the increasing demands on their applications as mentioned above.

Spintronics, which could take advantage of the spin degree of free electrons to realize the high-speed and low-energy-consumption information delivery and storage, are superior than conventional semiconductors and are desirable for applications in next-generation electronics [213]. In the past decades, the half-metallic materials, such as heusler alloys [257], manganese perovskites [258], and transition-metal oxides and dichalcogenides [259, 260], have been considered as suitable spintronic materials. In particular, the 2D half-metallic systems, such as GaSe [88], buckled phosphorene [179], SnO [87, 231], and InP_3 monolayers [90], are much promising for applications in spintronics since they could possess fully spin-polarized carriers and ferromagnetisms as induced or tuned by carrier doping. However, most of them would contain transition metals whose fabrication processes could not be compatible with current semiconductor industry [261]. It is thus desirable to search for 2D half-metallic materials containing group-IV or group-V elements.

Recently, a family of stable 2D group IV-V A_2B_2 (A = C, Si, Ge, Sn, Pb; B = N, P, As, Sb, Bi) systems that are composed of four intrinsic sub-layers were predicted to exhibit half-metallic or semiconducting properties by first-principle calculations [262]. In addition, 2D Janus structures derived from these 2D systems were further investigated. Among them, the Janus PA_2As (A = Si, Ge, Sn, and Pb) monolayers were predicted to possess hole-doping induced Stoner's ferromagnetism [235].

In this work, another 2D Janus structure derived from the 2D A_2B_2 systems, the Janus XYP_2 (X/Y= Si, Ge, Sn, and Pb; X≠Y) monolayer, is systematically investigated, which in experiments could be fabricated by replacing the inner-layer atoms of 2D A_2B_2 with X and Y atoms (X/Y = Si, Ge, Sn, and Pb; X≠Y). Based on the first-principles calculations and *ab-initio* molecular dynamic (AIMD) simulations, the Janus XYP_2 monolayers with a hexagonal crystal structure are found to show dynamical and thermodynamical stability. They are typical indirect-bandgap semiconductors with a bandgap ranging from 0.56 to 2.18 eV. More importantly, with good mechanical flexibility, the Janus XYP_2 monolayers have in-plane and out-of-plane piezoelectricity. Furthermore, the non-magnetic $SiGeP_2$, $GeSnP_2$ and $SnPbP_2$ monolayers can be adjusted to show ferromagnetic properties by hole doping. The results could facilitate the development of 2D materials for electronic, piezoelectric and spintronic applications.

5.2.2 Computational details

Our calculations were performed using the first-principles method based on the density functional theory as implemented with the Vienna ab initio simulation package (VASP) [118]. The projector-augmented wave method (PAW) was used to describe the interaction between valence electrons and the core [198, 199]. For the exchange-correlation potential, the generalized gradient approximation (GGA) proposed by Perdew Burke Ernzerhof (PBE) was used [113]. The kinetic energy cutoff for the plane-wave basis was set to be 500 eV. In the geometry optimization and the calculations of electronic band structures and elastic stiffness tensors, the Brillouin zone was sampled using a regular 12×12×1 Monkhorst Pack k-point mesh [142]. The convergence criteria of electronic and ionic relaxations were set to be 10^{-6} eV and 0.01 eV Å^{-1}, respectively. A vacuum layer with a thickness of 15 Å was added along the z-direction to avoid the interaction between adjacent slabs. The electronic band structure was also checked under the screened hybrid functional method at the Heyd–Scuseria–Ernzerhof (HSE06) level [143]. In the AIMD calculations, the 4×4×1 supercell and periodic boundary conditions were employed to minimize the size effects and the temperature was kept at 300 K. The piezoelectricity was calculated through the density functional perturbation theory (DFPT).

5.2.3 Results and details

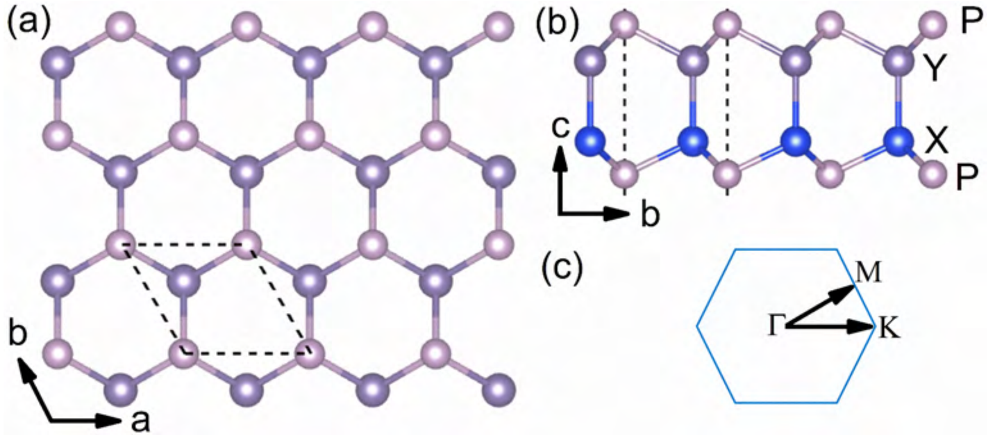

Figure 5.6 Top (a) and side (b) view of Janus XYP_2 monolayers. (c) The first Brillouin zone with high-symmetry points in the reciprocal space.

As derived from the 2D A_2B_2 systems, the Janus XYP_2 monolayers present a hexagonal crystal structure, which belongs to the $P3m1$ space group (No. 156). There are four atoms in the primitive cell with an independent lattice constant a. The following Janus

XYP_2 monolayers are studied in this work, namely, $SiGeP_2$, $SiSnP_2$, $SiPbP_2$, $GeSnP_2$, $GePbP_2$, and $SnPbP_2$. Figure 5.6 (a) and (b) shows their geometric structure with four sublayers (P atoms are located at the top and bottom layers, while X and Y atoms are stuck in the middle two layers), which is a typical Janus construction. Each X (Y) atom bonded with three adjacent P and Y (X) atoms with different bond lengths and angles.

Table 5.3 The calculated structural parameters (lattice constants a, bond length, and ΔZ), values and type of bandgap of Janus XYP_2 monolayers.

System	*a* (Å)	Bond length (Å)			ΔZ (Å)	Bandgap (eV)		Type
		X-P	Y-P	X-Y		PBE	HSE06	
$SiGeP_2$	3.58	2.29	2.34	2.42	0.099	1.46	2.18	Indirect
$SiSnP_2$	3.71	2.35	2.49	2.62	0.309	0.57	1.29	Indirect
$SiPbP_2$	3.76	2.37	2.57	2.69	0.428	0.04	0.56	Indirect
$GeSnP_2$	3.78	2.41	2.51	2.68	0.201	0.97	1.72	Indirect
$GePbP_2$	3.84	2.44	2.58	2.76	0.310	0.17	0.83	Indirect
$SnPbP_2$	4.00	2.57	2.62	2.95	0.113	0.82	1.39	Indirect

Table 5.3 lists the optimized structural parameters of Janus XYP_2 monolayers. The lattice constant *a* could vary from 3.58 to 4.00 Å, which increases with increasing atomic number of group-V elements (X or Y). Similarly, the bond length between X and Y atoms increases with increasing atomic number of X or Y. For example, $SiGeP_2$ monolayer exhibits the smallest *a* and X-Y bond length, whereas the $SnPbP_2$ monolayer shows the largest ones. All Janus XYP_2 systems possess a longer Y-P bond compared with X-P bond. Besides, there is a center along the z-direction, and the distances l_1 (l_2)

between X (Y) and the center are different. The difference between l_1 and l_2, $\Delta Z = l_1 - l_2$, could be a measure of the out-of-plane piezoelectricity of the monolayer.

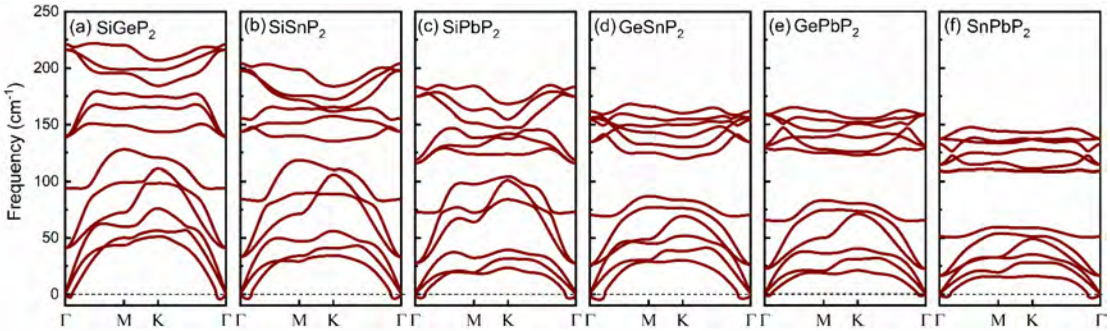

Figure 5.7 The phonon spectra of Janus XYP_2 monolayers.

The stability of Janus XYP_2 monolayers is first evaluated by using the phonon spectrum, as shown in Figure 5.7. It is clear that there is no appreciable negative frequency that can be observed in the Brillouin zone (For 2D materials, the slightly negative frequency in Γ point is negligible), indicating the dynamical stability of 2D XYP_2. Then, AIMD simulations are carried out to explore their thermal stability at 300 K, as shown in Figure 5.8. After the simulation of 6 ps with a step of 2 fs, the 2D structures remain relatively intact and the free energy fluctuation converges to a constant, implying that the Janus XYP_2 monolayers are thermally stable at room temperature.

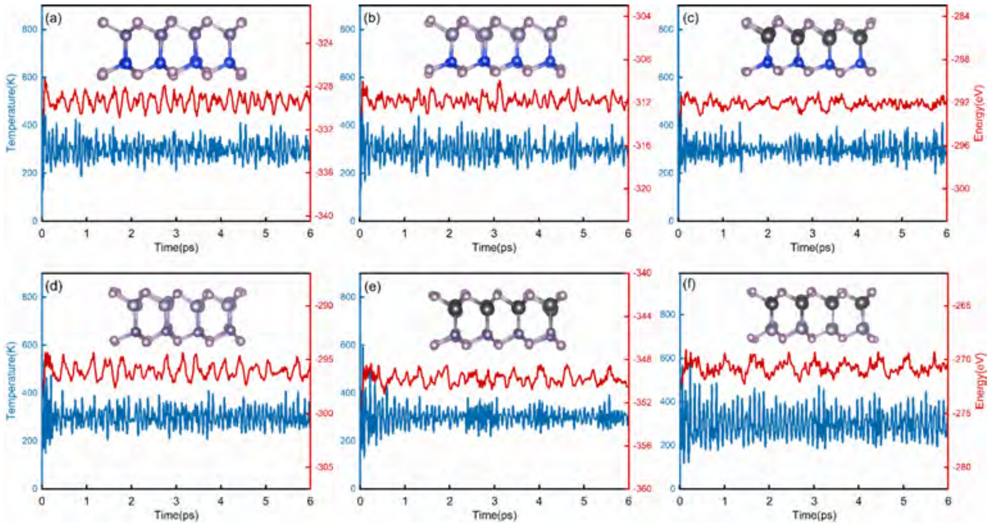

Figure 5.8 The evolution of temperature and free energy during the AIMD simulation at 300 K for Janus XYP_2 monolayers (a) $SiGeP_2$, (b) $SiSnP_2$, (c) $SiPbP_2$, (d) $GeSnP_2$, (e) $GePbP_2$, and (f) $SnPbP_2$. The insets are the structures after 6 ps.

The electronic properties of Janus XYP_2 monolayers can be calculated without considering the spin orbital coupling (SOC) effect, based on the fact that the influences of SOC on the band structure have been demonstrated to be negligible. Figure 5.9 shows the band structures along with the high-symmetry direction calculated by PBE and HES06 methods, respectively, which can be found to exhibit almost the same profiles. Clearly, all six 2D Janus systems studied in this work are indirect-bandgap semiconductors: the CBM locates at Γ-point while the VBM lies in the M-point. As summarized in Table 5.4, the bandgap determined by the HSE06 method varies between 0.56 and 2.18 eV for the Janus XYP_2 monolayer, which could be more accurate than that underestimated results by the PBE method. For $SiYP_2$ monolayers, the trend of change in bandgap values can be described as: $SiGeP_2 > SiSnP_2 > SiPbP_2$. Such increase in bandgap with increasing atomic number of Y is also found in the $GeYP_2$ monolayers. This is because heavier elements (such as Sn and Pb) have lower atomic orbital energy levels. Compared to lighter elements, their energy level difference decreases, leading to a smaller bandgap. Among all six 2D Janus systems, $SiGeP_2$ monolayer possesses the largest bandgap while $SiPbP_2$ monolayer exhibits the smallest one. The VBMs almost maintain with the same energy while the CBM varies obviously with the constituent elements in the 2D systems. To get more insights into the formation of electronic bands, the project density of states (PDOS) is also calculated using the

HSE06 method, as shown in Figure 5.9. In general, the PDOS of monolayers are quite similar, indicating that the VBM and CBM are mainly predominated by the *p*-orbital of X, Y and P atoms, whereas the *s*-orbital contributes slightly to the band structures in the vicinity of the Fermi energy. The p-orbitals of heavier elements (such as Pb) contribute more to the valence band, while the contributions from lighter elements (such as Si and Ge) are more concentrated in the conduction band.

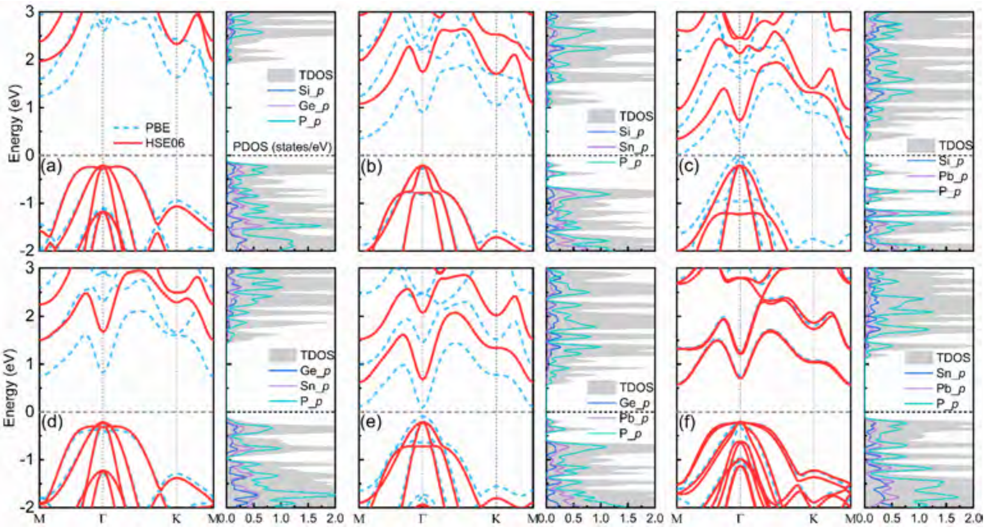

Figure 5.9 Band structures and projected density of states (PDOS) of Janus XYP_2 monolayers (a) $SiGeP_2$, (b) $SiSnP_2$, (c) $SiPbP_2$, (d) $GeSnP_2$, (e) $GePbP_2$, and (f) $SnPbP_2$, as calculated by PBE (blue dotted line) and HSE06 (red solid line) methods, respectively.

It is worth noting that the "Mexican hat" shape of profiles appears at the valence band structure of $SiGeP_2$, $GeSnP_2$, and $SnPbP_2$ monolayers, corresponding to the high density of states near the Fermi energy. This van Hove singularity leads to the electronic instability, providing the possibility that the monolayer would transform from a nonmagnetic state to a ferromagnetic state.

For the unique Janus structures, their mechanical properties are essential for their applications in electronic and spintronic nano-devices. Since the Janus XYP_2 monolayers belong to 3m point-group, there are only two independent elastic constants (C_{ij}), C_{11} and C_{12}, which can be calculated as $C_{11} = \frac{1}{A_0}\frac{\partial^2 U}{\partial \varepsilon_{11}^2}$, $C_{12} = \frac{1}{A_0}\frac{\partial^2 U}{\partial \varepsilon_{11} \partial \varepsilon_{22}}$, where A_0 is the area of unit cell at zero strain and U is the total energy of the system under in-plane strains ε_{ij}. The calculated elastic constants of monolayers are listed in Table 5.4. All monolayers can be found to well satisfy the Born criteria [263] for crystals with a hexagonal symmetry, namely, $C_{11} > 0$, $C_{66} > 0$, and $C_{11} - C_{12} > 0$, indicating their good mechanical stability. The elastic constants seem to increase with decreasing atomic number of element X or Y. For example, $SiGeP_2$ has the largest C_{11} (124.94 C/m) while $SnPbP_2$ has the smallest one (74.90 C/m). Meanwhile, C_{11} of 2D XYP_2 are comparable with those of most 2D materials, such as SnSe [264], MoS_2 [45], and GaSe [265], implying that the Janus XYP_2 monolayers possess good mechanical flexibility.

Table 5.4 The calculated elastic constants C_{ij} (N/m), Young's modulus Y_{2D} (N/m), layer modulus γ^{2D} (N/m), and Poisson's ratio v.

System	C_{11}	C_{12}	C_{66}	Y_{2D}	γ^{2D}	v
$SiGeP_2$	124.94	23.37	50.78	120.57	74.15	0.19
$SiSnP_2$	104.91	22.08	41.42	100.27	63.50	0.21
$SiPbP_2$	78.68	27.62	25.53	68.99	53.15	0.35
$GeSnP_2$	96.25	20.77	37.74	91.76	58.51	0.22
$GePbP_2$	83.78	18.85	32.46	79.54	51.31	0.22
$SnPbP_2$	74.90	18.45	28.22	70.35	46.68	0.25

On the basis of obtained elastic constants, the mechanical properties of Janus XYP_2 monolayers can be explored, such as Young's modulus $Y_{2D} = (C_{11}^2 - C_{12}^2)/C_{11}$, layer modulus $\gamma^{2D} = (C_{11} + C_{12})/2$, and Poisson's ratio $v = C_{12}/C_{11}$ [235]. As summarized in Table 5.4, the Young's modulus and layer modulus decrease with increasing atomic number of element X or Y. That is to say, large lattice constant *a* could lead to lower in-plane stiffness of Janus XYP_2 monolayers, which is still much higher than those of previous-studied Janus PA_2As (A = Si, Ge, Sn, and Pb) monolayers.

Table 5.5 The calculated piezoelectric coefficients e_{ij} (pC/m) and d_{ij} (pm/V).

System	e_{22}	e_{31}	d_{22}	d_{31}
$SiGeP_2$	123.16	9.5	1.21	0.064
$SiSnP_2$	111.74	12.78	1.35	0.101
$SiPbP_2$	64.04	13.18	1.25	0.124
$GeSnP_2$	82.9	3.5	1.10	0.030
$GePbP_2$	43.84	12.98	0.68	0.127
$SnPbP_2$	60.52	9.84	1.07	0.105

In non-centersymmetric crystals, the external strain or stress could induce changes of polarization. Such piezoelectricity can be evaluated by the rank-three piezoelectric stress tensor e_{ijk} and strain tensor d_{ijk} defined as follow:

$$e_{ijk} = \frac{dP_i}{d\varepsilon_{jk}}, \tag{5.1}$$

$$d_{ijk} = \frac{dP_i}{d\sigma_{jk}}, \tag{5.2}$$

where P_i, ε_{jk}, and σ_{jk} are the polarization vector, strain and stress tensors, respectively. In the formula, the first subscript i (1, 2, and 3) for polarization P_i

represents the polarization component along x-, y-, or z-directions. The last two subscripts j and k refer to the ε_{jk} and σ_{jk} tensors, which can be simplified by a single index 1 = xx, 2 = yy, 3 = zz, 4 = yz, 5 = zx, and 6 = xy in Voigt notation [266]. Here, only in-plane strains are considered for 2D materials and thus the piezoelectric coefficients can be expressed as e_{ij} and d_{ij}. In general, the Janus XYP_2 monolayers with 3m point-group symmetry lack both the inversion symmetry and reflectional symmetry on the *xy*-plane, which endow them to exhibit only four independent piezoelectric coefficients: the in-plane e_{22} and d_{22}, as well as out-of-plane e_{31} and d_{31}. Consequently, the corresponding piezoelectric stress and strain tensors become:

$$e_{ij} = \begin{pmatrix} 0 & 0 & -e_{22} \\ -e_{22} & e_{22} & 0 \\ e_{31} & e_{31} & 0 \end{pmatrix}, \quad 5.3$$

$$d_{ij} = \begin{pmatrix} 0 & 0 & -d_{22} \\ -d_{22} & d_{22} & 0 \\ d_{31} & d_{31} & 0 \end{pmatrix}. \quad 5.4$$

Specifically, they can be related by the elastic tensor C_{ij} through $e_{ij} = d_{ij}C_{ij}$. It is known that the nonzero independent elastic tensor for 2D hexagonal crystal is

$$C_{ij} = \begin{pmatrix} C_{11} & C_{12} & 0 \\ C_{12} & C_{11} & 0 \\ 0 & 0 & \frac{C_{11}-C_{12}}{2} \end{pmatrix}. \quad 5.5$$

Therefore, d_{22} and d_{31} can be calculated from e_{22} and e_{31} as

$$d_{22} = \frac{e_{22}}{C_{11}-C_{12}}, \quad 5.6$$

$$d_{31} = \frac{e_{31}}{C_{11}+C_{12}}. \quad 5.7$$

In order to analyze the piezoelectricity of Janus XYP_2 monolayers, the DFPT method is adopted to calculate the e_{ij} coefficients. From the results summarized in Table 5.4, we can see that the e_{22} and e_{31} coefficients exhibit the opposite trend of changes with increasing atomic number of element X or Y. For example, based on the same X atom, the e_{22} coefficient decreases as the atomic number of Y increases, while the e_{31} coefficient increases. The change in e_{31} coefficient can be related to ΔZ as listed in Table 5.3. As ΔZ increases, the distance between the center of positive charges and that of negative charges (the geometric center of the monolayer) increases as well, implying the existences of larger polarization and higher e_{31} coefficient in the monolayer. The d_{22} and d_{31} coefficients can be determined by Equation 5.6 and 5.7 and the corresponding results are also listed in Table 5.5. The in-plane d_{22} coefficients of most Janus XYP_2 monolayers are lower than 1 pm/V and the Janus $SiSnP_2$ monolayer has the largest d_{22} coefficient (1.35 pm/V), superior than those of Janus TMTC monolayers (0.02~0.08 pm/V) and 2D Janus $CrCl_{1:5}I_{1:5}$ (0.956 pm/V) [267]. Besides, the d_{31} and e_{31} coefficients increase as ΔZ increases. The values of e_{31} coefficients varying from 0.03 to 0.127 pm/V are comparable with those of Janus TMD monolayers (0.03 pm/V) [102], functionalized h-BN (0.13 pm/V) [53], and Janus group-III chalcogenide monolayers (0.07~0.46 pm/V) [57]. Such coexistence of in-plane and out-of-plane piezoelectricity as measured by large piezoelectric coefficients could facilitate the practical applications of Janus XYP_2 monolayers in nano-electronic and nano-electro-mechanical devices.

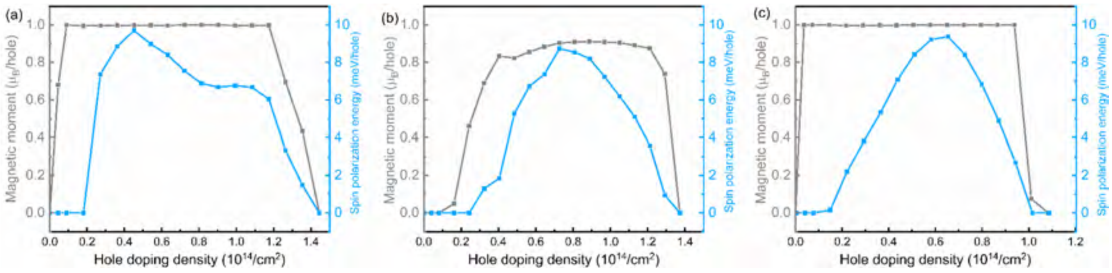

Figure 5.10 The magnetic moment per doping carrier and the spin polarization energy at different hole-doping density for (a) $SiGeP_2$, (b) $GeSnP_2$, and (c) $SnPbP_2$ monolayers.

The carrier doping is an effective approach in alternating the Fermi energy, leading to tunable electronic and ferromagnetic properties of 2D systems. It can be applied to induce or tune the ferromagnetisms of Janus XYP_2 monolayers. As mentioned above, $SiGeP_2$, $GeSnP_2$, and $SnPbP_2$ monolayers show van Hove points as the presence of flat bands but behave as non-ferromagnetic semiconductors, which are expected to have ferromagnetisms under hole doping with a small carrier density.

For the monolayers studied in this work, the hole doping can be carried out by adding holes to the unit cell. The opposite charges acting as compensating background keeps its charge neutrality. The spin polarization energy can be calculated with various hole-doping density n. That is the energy difference between the nonmagnetic and ferromagnetic states. A positive value implies the stable ferromagnetic phase. Consequently, the critical hole doping density (n_c) at which the ferromagnetic transition occurs in the monolayer is determined. Figure 5.10 (a-c) shows the evolution of magnetic moment and spin polarization energy as a function of carrier density for the $SiGeP_2$, $GeSnP_2$, and $SnPbP_2$ monolayers with hole doping, respectively. Clearly, for the $SiGeP_2$ monolayer, when the hole-doping density n is less than $n_c = 0.18\times10^{14}/cm^2$ (equivalent to 0.02 holes per unit cell), the magnetic moment occurs but the spin-polarization energy is about zero, suggesting the nonmagnetic state of 2D $SiGeP_2$. When $n > n_c$, the magnetic moment reaches the maximum of 1 μ_B/hole and the positive spin polarization energy further confirms the preferable ferromagnetic states of the monolayer. As the hole-doping density further increases, such fully spin-polarized state could be maintained until $n = 0.99\times10^{14}/cm^2$. However, the magnetic moment as well as the spin-polarization energy gradually drop to zero at $n > 1.44\times10^{14}/cm^2$, meaning that the ferromagnetic state disappears completely in 2D $SiGeP_2$ with a high hole-doping density. Besides, for 2D $GeSnP_2$, the ferromagnetic transition occurs when the hole-doping density is above $n_c = 0.24\times10^{14}/cm^2$ and disappears at $n > 1.37\times10^{14}/cm^2$, and no fully spin-polarized state can be obtained during the hole-doping process. This is because the relatively slow increasement of DOS near the Fermi level. Figure 5.10 (c) shows the ferromagnetisms induced by hole doping in 2D $SnPbP_2$, suggesting that the fully spin-polarized states can be obtained with n_c $(0.07\times10^{14}/cm^2) < n < 0.94\times10^{14}/cm^2$. Therefore, desirable ferromagnetic properties can be induced and tuned with various hole-doping densities in different Janus XYP_2 monolayers, which could be beneficial for various scenario of applications in electronics and spintronics.

5.2.4 Conclusions

In summary, the piezoelectricity and doping induced ferromagnetisms of 2D Janus XYP_2 structures (X/Y= Si, Ge, Sn, and Pb; X≠Y) are investigated by first-principles calculations. The monolayers are indirect-bandgap semiconductors with a bandgap varying from 0.56 and 2.18 eV. The 2D structures containing four sublayers are demonstrated to be dynamically and thermodynamically stable at room temperature. The calculated elastic constants as well as other mechanical properties indicate that they have good mechanical flexibility. Specially, the Janus XYP_2 monolayers exhibit in-plane and out-of-plane piezoelectricity, which is comparable to that of previously-explored 2D materials. Due to the electronic instability caused by van Hove singularity in the monolayers, hole doping is found to be an effective approach in inducing or tuning different ferromagnetic states in the Janus $SiGeP_2$, $GeSnP_2$, and $SnPbP_2$ monolayers. The results suggest that Janus XYP_2 monolayers could be promising 2D materials for applications in nano-electronic, spintronic and nano-electro-mechanical devices.

Chapter 6 High-entropy (MoWFeCoX)S_2 (X=Gd, Sm, and Nd) monolayers

6.1. Introduction

Since the introduction of high-entropy (HE) alloys by Yeh et al. in 2004 [268], HE materials have revolutionized the field of materials research. Comprising at least five multiple principal elements with equimolar or near-equimolar compositions, HE alloys have been increasingly studied and shown great potentials in widespread applications due to their excellent performance, such as catalysis [269], superconductors [270], and hydrogen storage [271]. Four key characteristics are cooperatively responsible for their chemical disorder structures and excellent performances: high entropy of mixing, severe lattice distortion, sluggish diffusion, and the cocktail effect [272]. Subsequently, the concept of HE materials has been extended to various compounds, including high-entropy oxides [273], carbides [274], borides [275], silicide [276], nitrides [277], etc. Some of them exhibit outstanding properties that exceed those of materials without chemical disorder, such as improved mechanical properties [274], ultra-low thermal conductivity [278] and huge dielectric constant [279]. Recently, the concept of HE was expanded to thin film. Layered HE materials have emerged as promising candidates for multifunctional applications due to their exceptional performance in energy storage and conversion [280, 281]. Nonetheless, HE effects in 2D systems have to be further explored.

Transition metal dichalcogenides (TMDCs), notable for their diverse chemical compositions and layered nature, possess excellent physical properties and have promising applications in several fields [282-284]. The cation sites in a crystal lattice not only have rich compositional tunability but also show large structural tolerance for doping atoms [285]. TMDC is a versatile materials class, which could be a valuable platform for developing HE 2D materials. For example, Cavin et al. successfully synthesized HE transition metal disulfides involving group V and VI transition metals using the chemical vapor transport method and liquid phase exfoliation technique [281]. It was found that $(MoWVNbTa)S_2$ shows extremely high activity for CO_2 electroreduction. Highly orientated $(VNbMoTaW)S_2$ layers were also realized by Tanaka et al., which provided a general synthesis route to prepare multi-compositions compounds. Besides, Qu et al. reported a low-temperature approach to obtain $(MoWReMnCr)S_2$ and evaluated its improved catalytic performance for hydrogen evolution electrocatalysis [286]. Nguyen et al. indicated that $(FeNiCoCrX)S_2$ (where X = Mn, Cu, Zn, or Al) exhibit superior oxygen evolution reaction activity with an exceptionally low overpotential [287]. Moreover, HE disulfides show potential as electrode materials for reversible electrochemical energy storage [288].

Currently, previous studies have focused on either high-entropy transition metal systems or high-entropy rare earth metal systems independently. The cationic elements of most layered HE disulfides are confined to the homogeneous types of elements. They are typically sandwiched with non-metal element S. Except these earth-abundant metals, the exist of rare earth elements allow materials valuable electrical and magnetic properties due to their partially filled f shells [289]. In this work, we firstly to introduce both transition metals and rare earth metals into a single HE system. 2D HE disulfides $(MoWFeCoX)S_2$ (X=Nd, Sm, and Gd) were constructed, where the atomic ratio of each cationic component is equal. We predict their stability with the formation energy and Gibbs free energy based on density functional theory (DFT). They can be stabilized at moderate temperatures, which can be achieved by recent experimental techniques. The relatively high adsorption coefficients in a broad energy range, especially in ultraviolet region, make them promising in optical applications. Besides, they have mechanical flexibility and anisotropy. These novel systems provide a materials platform to design 2D HE compounds containing both transition metals and rare earth elements.

6.2. Computational details

All calculations were performed within the framework of DFT using the Vienna *ab initio* simulation package (VASP) [198]. The exchange-correlation potential was treated with the generalized gradient approximation (GGA) using the Perdew-Burke-Ernzerhof (PBE) method [113]. The projector augmented wave (PAW) method was applied to describe electron-ion interactions. A plane-wave basis set with a kinetic energy cut-off of 500 eV was employed. For Brillouin zone sampling, a regular 2×2×1 Monkhorst−Pack k-point mesh was utilized [142]. Structural optimizations were carried out until the total energy convergence criterion of 10^{-5} eV and the Hellmann−Feynman forces were less than 10^{-2} eV/Å. The special quasi-random structures (SQS) method was employed to model the random solid solution structures of HE $(MoWFeCoX)S_2$ monolayers. The MCSQS tool [290] from the Alloy Theoretic Automated Toolkit (ATAT) package [291] was utilized to generate SQS supercells. In this study, 5 × 5 × 1 supercells with 75 atoms were constructed. The SQS supercells were optimized by running the MCSQS code multiple times and selecting the configuration with the lowest energy value. A vacuum slab of approximately 15 Å was used to prevent interactions between periodic images of the monolayer. Van der Waals interactions within layers were corrected using the DFT-D3 approach following Grimme’s scheme [147].

6.3. Results and discussion

6.3.1 Structures and stability

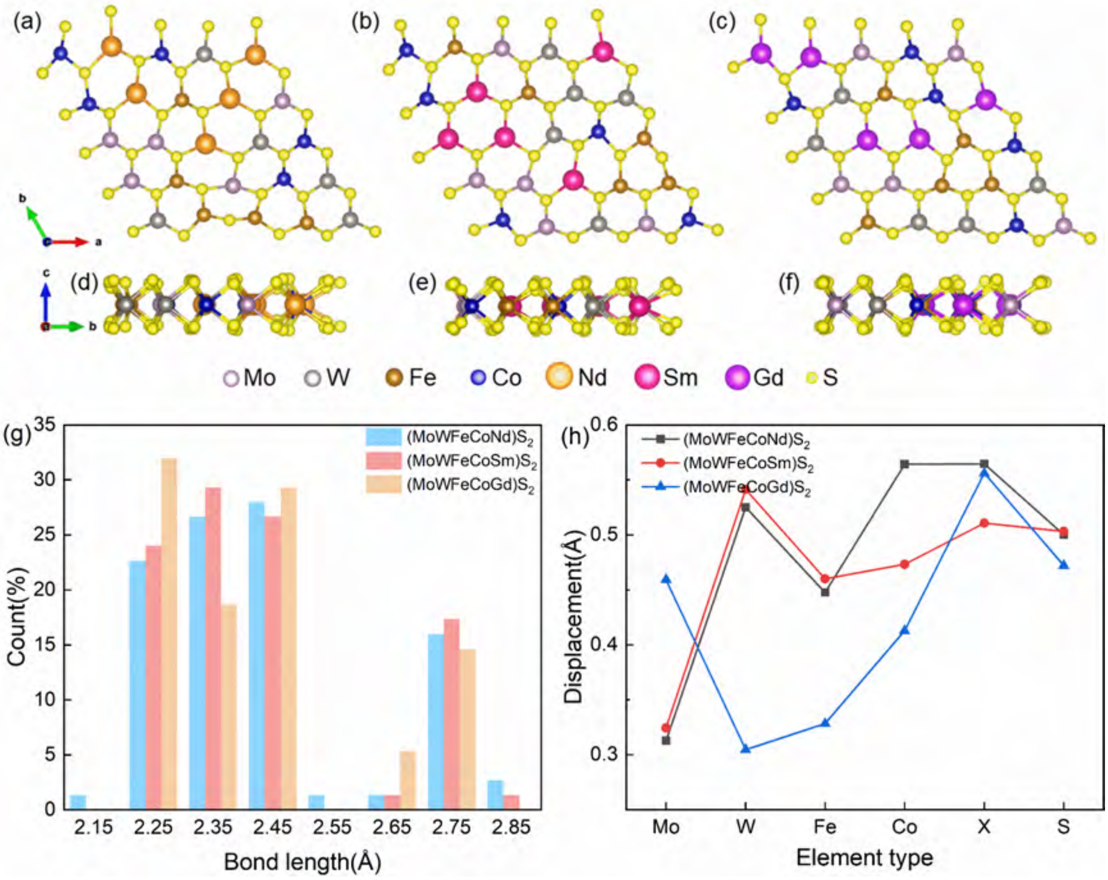

Figure 6.1 Top view (a-c) and side view (d-f) of 5 × 5 ×1 supercell of HE

$(MoWFeCoX)S_2$ (X=Nd, Sm, and Gd) monolayers, respectively. (g) Corresponding metal-nonmetal bond length distribution and (h) average atomic displacement.

To simulate chemical disorder states in the MoS_2-based HE $(MoWFeCoX)S_2$ (X=Nd, Sm, and Gd) sublattice completely, the 5 × 5 × 1 SQS supercells are generated. They are obtained by partly replacing the molybdenum (Mo) atom by transition metal element tungsten (W), iron (Fe), cobalt (Co), as well as one of rear-earth elements chosen from neodymium (Nd), samarium (Sm) and gadolinium (Gd) using ATAT software. We carry out the selection on the SQS supercell for several times and choose the lowest-energy one for discussion. The choice of elements for these systems is based on several key considerations. Firstly, Mo and W are selected to stabilize the whole frame. This is because that MoS_2 and WS_2 are widely studied and synthesized in their 2D forms, exhibiting strong stability and desirable electronic properties. Secondly, both Fe and Co are common transition metals with strong magnetic behaviors, which could contribute significantly to the overall magnetic characteristics of the HE material. Thirdly, rare earth elements such as Nd, Sm, and Gd were chosen for their unique electronic configurations, particularly their half-filled f-orbitals. The larger atomic radii of these elements could induce large lattice distortions, potentially affecting the mechanical properties and electronic structure of the HE monolayers. Because 1T-MoS_2 is not thermodynamically stable, we only consider the 1H phase in this study. The full relaxed atomic structures of three HE monolayers are shown in Figure 6.1. These monolayers consist of three layers stacked in the sequence of S-M-S, where M represents metals. The desired five M cations locate at sublattices randomly and have the same coordination environment, namely, each M atoms bonded with three S atoms above and three below. After structural optimization, the M-S bonds in the HE monolayer experience varying degrees of distortion, resulting in atomic-scale corrugation. It could be related to different atomic sizes and electronegativities of M cations. The histograms of bond length of M-S bonds in each monolayer give a clear description, as shown in Figure 6.1(g-i). The M-S distance varies from 2.2 to 2.9 Å where the bond lengths larger than 2.5 Å are attributed to rare earth M-S bond. Such significant range of bond length indicates large local distortion. Mean square displacements (MSDs) are also calculated through the following formula: $MSD = \frac{1}{N}\sum_{1}^{N}(r_i(t) - r_i(0))^2$, where N is the number of total atoms and r_i is the location of ith atom. According to the value listed in Table 6.1, Nd-containing disulfides has the most prominent distortion, followed by Sm- and Gd-containing disulfides, which is consistent with the bond-length changes. The relaxed lattice constants a and b are listed in Table 6.1. Though some wrinkle appears in structures, all three HE monolayers remain intact with the thickness about 3.33~3.40 Å, slightly larger than that of MoS_2 (3.13 Å).

Table 6.1 The lattice constants a and b (Å), layer thickness (Å), MSD (Å^2), formation energy E_{form} (eV/atom), formation enthalpy ΔH_f (eV/f.u.), and estimated temperature T (K) at which the five-cation HE systems are more stable than the parent sulfides for HE $(MoWFeCoX)S_2$ monolayers, respectively.

System	a	b	Δh	MSD	E_{form}	ΔH_{mix}	T
(MoWFeCoNd)S_2	16.30	14.31	3.33	0.53	-0.76	0.17	1217
(MoWFeCoSm)S_2	16.33	14.48	3.37	0.50	-0.78	0.11	819
(MoWFeCoGd)S_2	16.60	14.29	3.40	0.48	-0.79	0.10	735

To confirm the chemical stability of HE (MoWFeCoX)S_2 monolayers, the formation energy (E_{form}) is evaluated through the following formula [292]:

$$E_{form} = (E_{tot} - \sum N_i E_{i-bulk})/\sum N_i, \qquad 6.1$$

where E_{tot} is the total energy of HE monolayers, E_{i-bulk} is the energy of one atom of the *i*th-type in their respective stable crystal, N_i is the number of the corresponding atoms. Theoretically, negative formation energy implies the stable structure of monolayer and a greater negative value means higher stability. As shown in Table 6.1, the formation energies of three monolayers are all negative, indicating the energetically favorable conditions for the formation of such HE systems. The E_{form} value of (MoWFeCoGd)S_2 (-0.79 eV/atom) demonstrates its better stability than those of (MoWFeCoNd)S_2 and (MoWFeCoSm)S_2 monolayers.

Additionally, to access the thermodynamic stability of HE monolayers, formation enthalpy (ΔH_{mix}) is calculated based on the corresponding parent single-cation sulfides MS_2 as [292]:

$$\Delta H_{mix} = (E_{tot} - \sum N_i E_i^{MS_2})/\sum N_i, \qquad 6.2$$

where E_{tot} and $E_i^{MS_2}$ are the total energy of HE monolayer and individual thermodynamically stable MS_2 monolayer, respectively. N_i is the number of metal sulfides MS_2. The results of ΔH_{mix} summarized in Table 6.1 are positive, suggesting that the formation of HE monolayer from isostructural binary sulfides is an endothermic process. The results could be related to the appearance of bond distortions, which enhance the energy of HE systems compared to their parent sulfides. However, the magnitude of ΔH_{mix} is rather small, with the largest value of only 0.17 eV, which is about the same magnitude with those of stable HE metal diborides [293] and metal dichalcogenides [294]. It is noted that ΔH_{mix} is not the only criteria to determine the thermodynamic stabilities of a HE system. The variance of Gibbs free energy between HE $(MoWFeCoX)S_2$ monolayers and their parent MS_2 is also an important influential factor, which can be expressed in terms of mixing enthalpy and entropy [292]:

$$\Delta G_{mix} = \Delta H_{mix} - T\Delta S_{mix}, \tag{6.3}$$

where T is the absolute temperature. While vibrational entropy is significant at finite temperatures [295], the vibrational component of entropy difference between the HE systems and the parent structures can be ignored due to their similar bonding [294]. This approximation is proven to be effective and reasonable in other alloy materials [296, 297]. With the results of DFT calculations at 0 K, the ΔS_{mix} value is approximately equal to enthalpy differences at various temperatures [298]. By ignoring vibrational contributions to both enthalpy and entropy, we can estimate the temperature at which HE $(MoWFeCoX)S_2$ systems become more stable than their parent disulfides using $T \cong \Delta H_{mix}/\Delta S_{mix}$. Here, ΔS_{mix} is the mixing entropy, which can be evaluated based on the possibility when five different cations are equally distributed among the available sites. With the equal possibility of occupancy of each cation at a lattice site and the exclusion of (temperature-dependent) vibrational contributions, ΔS_{mix} remains constant at all temperatures:

$$\Delta S_{mix} = -Rnx\ln x = 1.609R, \tag{6.4}$$

where R is the universal gas constant, n is the number of components in the system (n=5 in this work), and $x=\frac{1}{n}$=0.2 represents the mixing concentration of each component. Thus, as long as the temperature is high enough, the effect of entropy is greater than that of enthalpy and a negative Gibbs free energy can be obtained. In that case, HE (MoWFeCoX)S_2 systems can be formed theoretically. The calculated stabilization temperatures T range from 735 to 1217 K, as listed in Table 6.1. The temperatures required for producing high-quality layered materials are often influenced by kinetic factors and can be refined through practice. According to current experimental techniques [281, 298-300], the synthesis temperature of HE sulfides and nitrides is also appropriate for ensuring growth and stability of HE (MoWFeCoX)S_2 systems.

6.3.2 Electronic properties

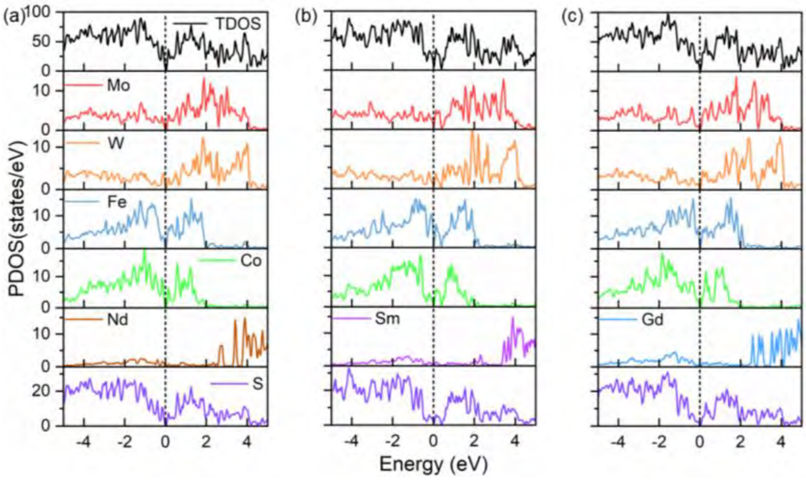

Figure 6.2 The PDOS of HE (MoWFeCoNd)S_2, (MoWFeCoSm)S_2, and (MoWFeCoGd)S_2 monolayers, respectively. The Fermi level is set to zero.

To explore how the rare earth element influences the electronic structure of HE (MoWFeCoX)S_2 systems, the total density of states (TDOS) and projected density of states (PDOS) distributions are investigated, as shown in Figure 6.2. The Fermi level (E_F) is set to zero and marked by a dashed line. There is non-zero value at the Fermi level, indicating the metallic chrematistics of monolayers, which is consistent with other HE sulfides [301]. In the valence band region, Mo, W, Fe, Co and S atoms exhibit a strong interaction, giving rise to covalent bonds between them. Rare earth Nd, Sm, and Gd atoms interact strongly with S atom at high energy at the conduction band region.

6.3.3 Optical properties

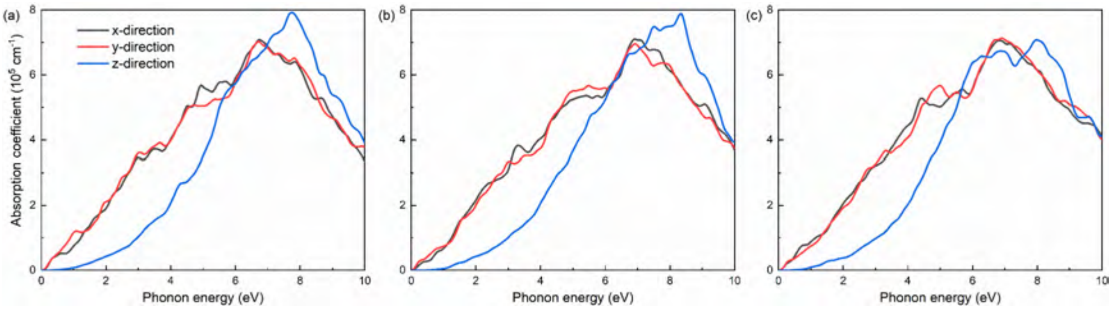

Figure 6.3 Calculated absorption coefficients of HE (MoWFeCoNd)S_2, (MoWFeCoSm)S_2, and (MoWFeCoGd)S_2 monolayers, respectively, with the incident light along x-, y-, and z-direction.

The study of optical properties in 2D materials has obtained significant attention due to their potential applications in optoelectronics, photovoltaics, and photodetectors.

Here, we investigate the optical absorption characteristics of three HE (MoWFeCoX)S_2 systems from the imaginary part of the dielectric function. It can be obtained by the following formula: $\alpha = \sqrt{2}\omega\left[\sqrt{\varepsilon_1^2(\omega)+\varepsilon_2^2(\omega)}-\varepsilon_1^2(\omega)\right]^{\frac{1}{2}}$ [302, 303], where $\varepsilon_1(\omega)$ and $\varepsilon_2(\omega)$ are the real and imaginary parts of the frequency dependent dielectric functions, respectively. The optical absorption spectra for the three materials are shown in Figure 6.3. The x-, y-, and z-directional absorption coefficients are plotted as functions of photon energy, indicating anisotropic optical responses. As shown in Figure 6.3(a), the absorption coefficient of Nd-containing monolayer increases with increasing photon energy, exhibiting a peak at about 7 ~ 8 eV. Along z-direction, the 2D material exhibits a higher absorption coefficient (as high as 7.92×10^5 cm^{-1}) compared to those along x- and y-directions, suggesting strong out-of-plane optical transitions. Sm-containing monolayer presents similar trends, and the absorption coefficient exhibits a peak at about 6 ~ 7 eV (Figure 6.3(b)). For Gd-containing monolayer (see Figure 6.3(c)), the absorption peak is broadened, spanning from 6 to 8 eV with significant contributions from all three directions. These three monolayers can absorb a broad energy range from the visible to the ultraviolet regions, with some absorption activities occurred in the infrared range as well. Specifically, the absorption coefficients increase from about 0 ~ 1 eV and maintain at high values across the spectrum. The results suggest that they are promising candidates for applications in optoelectronic devices, such as photodetectors and solar cells. The anisotropic nature of their optical responses can be leveraged to design devices with directional sensitivity, enhancing performance and efficiency.

6.3.4 Mechanical properties

Table 6.2 Independent elastic constants C_{ij} (N/m) of HE (MoWFeCoX)S_2 monolayers.

System	C_{11}	C_{12}	C_{16}	C_{22}	C_{26}	C_{66}
(MoWFeCoNd)S_2	70.77	31.40	1.77	66.27	0.46	19.21
(MoWFeCoSm)S_2	63.55	28.82	2.01	71.00	0.34	20.09
(MoWFeCoGd)S_2	72.59	30.32	-2.68	74.19	-1.48	19.84

The mechanical properties of HE (MoWFeCoX)S_2 monolayers are further examined by calculating the associated elastic constants, describing their resistance to deformation or distortions under the external strains. For 2D systems in the linear elastic range, the stress σ response to the presence of applied strain ε obeys the generalized Hooke's law and can be expressed in the Voigt notation as C_{ij} (i=1, 2, 6), where 1-xx, 2-yy, and 6-xy [266]. The strain-stress method is used to derive six independent C_{ij} for the monolayers studied, namely, C_{11}, C_{12}, C_{16}, C_{22}, C_{26} and C_{66}, and the results are listed in Table 6.2. Based on the obtained elastic constants C_{ij}, the mechanical stability, anisotropic behavior and hardness of monolayers can be assessed. Clearly, the calculated elastic constants satisfy the Born criterion of 2D materials:[207] $C_{11} > |C_{12}|$, $C_{11}C_{22}–C_{12}^2 > 0$, $C_{66} > 0$, indicating the structural stability of HE (MoWFeCoX)S_2 monolayer.

Besides, we estimate the in-plane Young's modulus and Poisson ratio as a function of angle θ by the following relation: $Y(\theta) = \frac{C_{11}C_{22}-C_{12}^2}{C_{22}\cos^4\theta+A\cos^2\theta\sin^2\theta+C_{11}\sin^4\theta}$, $v(\theta) = \frac{C_{12}\cos^4\theta-B\cos^2\theta\sin^2\theta+C_{12}\sin^4\theta}{C_{22}\cos^4\theta+A\cos^2\theta\sin^2\theta+C_{11}\sin^4\theta}$, where $A = (C_{11}C_{22} - C_{12}^2)/C_{66} - 2C_{12}$ and $B = C_{11} + C_{22} - (C_{11}C_{22} - C_{12}^2)/C_{66}$. As shown in Figure 6.3, both Young's modulus and

Possion’s ratio of these three HE monolayers exhibit anisotropy. The Young’s modulus of $(MoWFeCoSm)S_2$ and $(MoWFeCoGd)S_2$ monolayers have the similar changing trend with the orientation. At θ =0 and 180° (x direction), the Young’s modulus of Nd-containing monolayer reaches the largest value (55.89 N/m). Those of Sm- and Gd-containing monolayers behave the opposite trend and possess the lowest value of $Y(\theta)$ at θ =0° and 180° (x direction), whereas it is as high as 57.93 N/m and 61.522 N/m, respectively, at 90° and 270° (y direction). The results indicate that Nd-containing monolayer shows greater rigidity against deformation along x direction, while that of Sm- and Gd-containing monolayers is along y direction. Moreover, their $Y(\theta)$ value is lower than that of traditional 2D materials, such as graphene (340 N/m) [304], h-BN (275.8 N/m) [207], and MoS_2 (330 N/m) [209], suggesting they are potential materials used in next-generation flexible devices. The Possion’s ratio describes the mechanical response of material under uniaxial strains, namely, the ratio of the strain along transverse direction to that along longitudinal direction. Its positive value means that the material will shrink along x direction against the strain along y direction. Nd-, Sm-, and Gd-containing monolayers reach the highest values of $\nu(\theta)$ (0.47, 0.45, 0.45, respectively) at 0°, 90°, and 47°, respectively. Such low value (< 0.5) suggests the good compressibility of the HE monolayers studied.

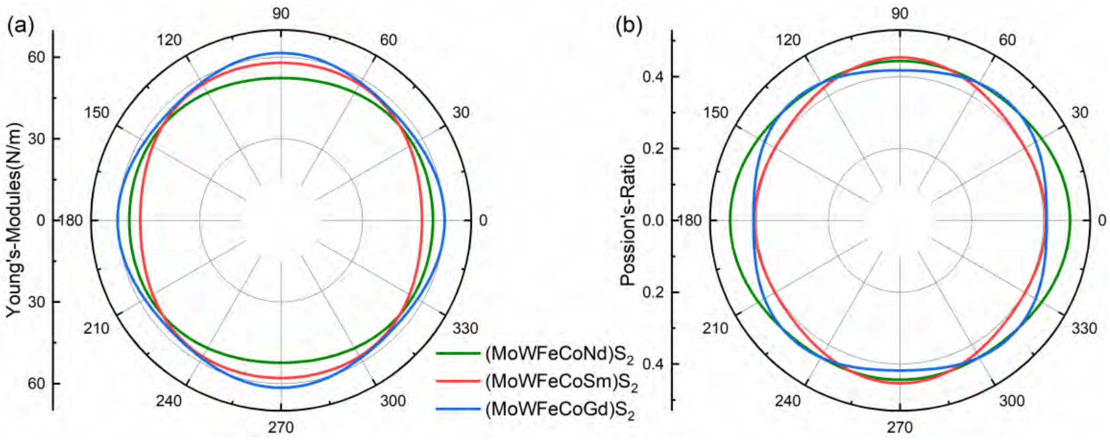

Figure 6.4 The polar diagrams representing (a) Young's modulus and (b) Poisson's ratio for all HE (MoWFeCoX)S_2 monolayers studied.

6.4. Conclusions

In summary, the investigation of 2D HE disulfides, (MoWFeCoX)S_2 (X=Nd, Sm, and Gd) monolayers reveals their potential for multifunctional applications. Despite the local distortions inherent in atomic structures, these HE compounds exhibit remarkable stability and are predicted to be achievable under moderate synthesis temperatures. The high absorption coefficients over a broad spectral range indicates their suitability for advanced optoelectronic applications. Additionally, the anisotropic mechanical properties further enhance their versatility, making these HE disulfides promising candidates used in next-generation multifunctional devices. The 2D HE disulfide provides a platform for developing HE materials containing transition metals and rare earth elements in a single system, providing innovative solutions for diverse technological applications.

Chapter 7 Conclusions and outlooks

The emerging 2D materials have attracted widespread attention due to their potential applications in various devices such as sensors, capacitors, energy harvesting devices, piezoelectric electronics, and spintronics. The research on the structure and properties of 2D materials not only promotes the development of fundamental physics but also holds significant importance for the advancement of materials science and multifunctional integrated devices. There are some limitations of the electrical and magnetic properties of 2D materials, as follows: First, most reported 2D materials possess the bandgap smaller than 2.5 eV, which limit the application in utilizing blue and ultraviolet light. Second, 2D systems with multidirectional piezoelectricity that the applied strain in one direction would produce polarization changes in multiple directions are more desirable and valuable for practical applications. Third, 2D dielectric materials have not been well explored for their application as dielectric layers in capacitors. Fourth, intrinsic magnetism in 2D family has been intensively predicted in theoretically reports, but few are synthesized in experiment with Curie temperature higher than room temperature. Therefore, the exploration of 2D materials with integrated excellent properties is crucial for the applications of multifunctional devices. In this thesis, we design and investigate the structure, stability, electronic properties, and magnetic properties of several novel 2D materials through first-principles calculations based on density functional theory. The main research findings are as follows:

1) We predict a novel 2D GaOCl monolayer and investigate its excellent properties. As a wide-bandgap semiconductor with a bandgap value of 4.46 eV, GaOCl monolayer possesses stability at room temperature and can be obtained by mechanical exfoliation. The viability of electric band structures under applied strains reveals its mouldability. High anisotropic carrier mobility enables its potential applications in modern electronic devices. Because of the existence of van Hove singularity, its ferromagnetism can be induced by hole doping. The in-plane and out-of-plane piezoelectricity are simultaneously identified in GaOCl monolayer, which are compatible to other previously reported 2D piezoelectric materials. This work demonstrates that GaOCl monolayer is a promising 2D candidate for nanodevice applications, which is awaiting for further experimental verification.

2) Based on first-principles calculations, 2D Janus GaOClX (X = F, Br, and I) monolayers are identified to be promising dielectric materials with superior energy storage properties. These monolayers exhibit characteristics of indirect-bandgap properties, with bandgaps ranging from 2.18 to 4.36 eV. Moreover, the monolayer possesses anisotropic carrier mobility, strong mechanical flexibility, and excellent out-of-plane piezoelectricity. Importantly, our findings reveal that both parent GaOCl monolayer and Janus GaOClX monolayers demonstrate ultrahigh energy storage density, which is as high as 893.32 J/cm^3, comparable to those of electrochemical supercapacitors and batteries. It is because that they have large electric breakdown strength and low remnant polarization. The results open up new avenues for the development of novel dielectric materials with superior energy storage density and

power density, offering excellent efficiency and thermal stability. The discovery of 2D dielectric materials holds significant promise for the advancement of energy conversion and storage technologies.

3) Based on first-principles calculations, we observe that at a certain concentration of electron doping ranging from ~10^{13} to ~10^{14} cm^{-2}, the Janus TiXO (X = S, Se) systems maintain a fully spin-polarized state with a Curie temperature estimated to be above room temperature. This finding opens avenues for applications in electronics and spintronics, where tunable magnetism is highly desirable. Additionally, by varying doping concentrations and applying strains, we demonstrate that it is viable to substantially modulate doping-induced magnetisms and Curie temperature in Janus TiXO multilayers. These results contribute to advancing our understanding of 2D materials that could be potential materials in next-generation electronic devices.

In addition, novel Janus XYP_2 (X/Y = Si, Ge, Sn, and Pb; X $\neq$ Y) monolayers with their promising multifunctional properties for various nano-electronic and electromechanical applications are investigated. These 2D materials exhibit excellent stability, electronic, mechanical, and piezoelectric properties. With bandgaps varying from 0.56 to 2.18 eV, they offer possibility of bandgap engineering for specific application requirements. Notably, hole doping is proved to be an effective approach in inducing or tuning different ferromagnetic states in Janus $SiGeP_2$, $GeSnP_2$, and $SnPbP_2$ monolayers, highlighting their versatility for spintronic applications. The transformation from semiconductor to half metal also occurs due to the spin splitting. Furthermore, the large piezoelectric coefficients observed in these monolayers suggest they are promising piezoelectric materials for nano-electromechanical systems. These findings pave the way for the development of advanced 2D materials for diverse technological needs.

4) The investigation of 2D HE disulfides, (MoWFeCoX)S_2 (X=Gd, Sm, and Nd) monolayers, reveals that they can be promising multifunctional nanomaterials. Despite the local distortions inherent in their structures, these HE compounds exhibit remarkable stability, achievable under moderate synthesis temperatures. The high absorption coefficients over a broad spectral range, underscore their suitability for advanced optoelectronic applications. Additionally, the anisotropic mechanical properties further enhance their versatility, making these HE disulfides promising candidates for next-generation multifunctional devices. This study provides a platform for HE materials containing transition metals and rare earth elements, developing innovative solutions for diverse technological applications.

Despite the remarkable advancements in the field of 2D materials, several challenges remain. One significant issue is the scalability of synthesis methods. Many promising 2D materials are still produced in limited quantities, hindering their integration into large-scale industrial applications. Additionally, the stability of these materials under ambient conditions needs further investigation to ensure long-term functionality in real-world environments. Another challenge lies in the precise control of electronic properties, as slight variations in synthesis can lead to significant differences in performance. Moreover, the interface and contact engineering in devices made from 2D materials require optimization to enhance efficiency and reduce energy losses.

First-principles calculations have proven to be an effective tool in predicting the properties of 2D materials, offering insights that guide experimental efforts. The theoretical studies allow researchers to explore novel 2D candidates efficiently, identifying materials with desirable characteristics before committing to costly and time-consuming experiments.

Looking forward, the integration of first-principles predictions with advanced experimental techniques will accelerate the development of 2D materials. Efforts should focus on combining expertise in materials science, chemistry, physics, and engineering to overcome current limitations. The continued computational prediction and investigation holds the promise of unlocking the full potential of 2D materials, paving the way for revolutionary advancements in nanotechnology and materials science.

References

[1] C. Tan, X. Cao, X.-J. Wu, Q. He, J. Yang, X. Zhang, J. Chen, W. Zhao, S. Han, G.-H. Nam, M. Sindoro and H. Zhang, *Chemical Reviews*, 2017, **117**, 6225-6331.

[2] K. S. Novoselov, A. K. Geim, S. V. Morozov, D. Jiang, Y. Zhang, S. V. Dubonos, I. V. Grigorieva and A. A. Firsov, *Science*, 2004, **306**, 666.

[3] J. C. Slonczewski and P. R. Weiss, *Physical Review*, 1958, **109**, 272-279.

[4] S. K. Tiwari, S. Sahoo, N. Wang and A. Huczko, *Journal of Science: Advanced Materials and Devices*, 2020, **5**, 10-29.

[5] Y. Zhang, Y.-W. Tan, H. L. Stormer and P. Kim, *Nature*, 2005, **438**, 201-204.

[6] K. S. Novoselov, Z. Jiang, Y. Zhang, S. V. Morozov, H. L. Stormer, U. Zeitler, J. C. Maan, G. S. Boebinger, P. Kim and A. K. Geim, *Science*, 2007, **315**, 1379-1379.

[7] G. Giovannetti, P. A. Khomyakov, G. Brocks, P. J. Kelly and J. van den Brink, *Physical Review B*, 2007, **76**, 073103.

[8] Y. Liu, X. Duan, Y. Huang and X. Duan, *Chemical Society Reviews*, 2018, **47**, 6388-6409.

[9] A. H. Castro Neto, F. Guinea, N. M. R. Peres, K. S. Novoselov and A. K. Geim, *Rev. Mod. Phys.*, 2009, **81**, 109-162.

[10] K. I. Bolotin, K. J. Sikes, Z. Jiang, M. Klima, G. Fudenberg, J. Hone, P. Kim and H. L. Stormer, *Solid State Commun.*, 2008, **146**, 351-355.

[11] A. K. Geim and K. S. Novoselov, *Nature Materials*, 2007, **6**, 183-191.

[12] S. Kim, S. W. Hwang, M.-K. Kim, D. Y. Shin, D. H. Shin, C. O. Kim, S. B. Yang, J. H. Park, E. Hwang, S.-H. Choi, G. Ko, S. Sim, C. Sone, H. J. Choi, S. Bae and B. H. Hong, *ACS Nano*, 2012, **6**, 8203-8208.

[13] L. Tang, R. Ji, X. Cao, J. Lin, H. Jiang, X. Li, K. S. Teng, C. M. Luk, S. Zeng, J. Hao and S. P. Lau, *ACS Nano*, 2012, **6**, 5102-5110.

[14] S. H. Jin, D. H. Kim, G. H. Jun, S. H. Hong and S. Jeon, *ACS Nano*, 2013, **7**, 1239-1245.

[15] D. Pan, J. Zhang, Z. Li and M. Wu, *Advanced Materials*, 2010, **22**, 734-738.

[16] A. E. Naclerio and P. R. Kidambi, *Advanced Materials*, 2023, **35**, 2207374.

[17] R. T. Paine and C. K. Narula, *Chemical Reviews*, 1990, **90**, 73-91.

[18] L. F. Dobrzhinetskaya, R. Wirth, J. Yang, H. W. Green, I. D. Hutcheon, P. K. Weber and E. S. Grew, *Am. Mineral.*, 2014, **99**, 764-772.

[19] N. Izyumskaya, D. O. Demchenko, S. Das, Ü. Özgür, V. Avrutin and H. Morkoç, *Advanced Electronic Materials*, 2017, **3**, 1600485.

[20] C. Frondel and U. B. Marvin, *Nature*, 1967, **214**, 587-589.

[21] W. Paszkowicz, J. B. Pelka, M. Knapp, T. Szyszko and S. Podsiadlo, *Appl. Phys. A*, 2002, **75**, 431-435.

[22] G. Cassabois, P. Valvin and B. Gil, *Nature Photonics*, 2016, **10**, 262-266.

[23] W. J. Yu, W. M. Lau, S. P. Chan, Z. F. Liu and Q. Q. Zheng, *Physical Review B*, 2003, **67**, 014108.

[24] K. F. Mak and J. Shan, *Nature Photonics*, 2016, **10**, 216-226.

[25] Y. Wei, X. Tang, J. Shang, L. Ju and L. Kou, *International Journal of Smart and Nano Materials*, 2020, **11**, 247-264.

[26] K. F. Mak, C. Lee, J. Hone, J. Shan and T. F. Heinz, *Physical Review Letters*, 2010, **105**, 136805.

[27] S. Bertolazzi, D. Krasnozhon and A. Kis, *ACS Nano*, 2013, **7**, 3246-3252.

[28] J. Feldmann, G. Peter, E. O. Göbel, P. Dawson, K. Moore, C. Foxon and R. J. Elliott, *Physical Review Letters*, 1987, **59**, 2337-2340.

[29] Z. Guan, C.-S. Lian, S. Hu, S. Ni, J. Li and W. Duan, *The Journal of Physical Chemistry C*, 2017, **121**, 3654-3660.

[30] R. Cheng, D. Li, H. Zhou, C. Wang, A. Yin, S. Jiang, Y. Liu, Y. Chen, Y. Huang and X. Duan, *Nano Letters*, 2014, **14**, 5590-5597.

[31] L. Li, Y. Yu, G. J. Ye, Q. Ge, X. Ou, H. Wu, D. Feng, X. H. Chen and Y. Zhang, *Nature Nanotechnology*, 2014, **9**, 372-377.

[32] V. Tran, R. Soklaski, Y. Liang and L. Yang, *Physical Review B*, 2014, **89**, 235319.

[33] J. Lu, J. Yang, A. Carvalho, H. Liu, Y. Lu and C. H. Sow, *Acc. Chem. Res.*, 2016, **49**, 1806-1815.

[34] X. Hao, *Journal of Advanced Dielectrics*, 2013, **03**, 1330001.

[35] G. Chen, J. Zhao, S. Li and L. Zhong, *Applied Physics Letters*, 2012, **100**, 222904.

[36] B. Chu, X. Zhou, K. Ren, B. Neese, M. Lin, Q. Wang, F. Bauer and Q. M. Zhang, *Science*, 2006, **313**, 334-336.

[37] Q. Hu, J. Bian, P. S. Zelenovskiy, Y. Tian, L. Jin, X. Wei, Z. Xu and V. Y. Shur, *Journal of Applied Physics*, 2018, **124**, 054101.

[38] H. Zhang, T. Wei, Q. Zhang, W. Ma, P. Fan, D. Salamon, S.-T. Zhang, B. Nan, H. Tan and Z.-G. Ye, *Journal of Materials Chemistry C*, 2020, **8**, 16648-16667.

[39] Z. Liu, T. Lu, J. Ye, G. Wang, X. Dong, R. Withers and Y. Liu, *Advanced Materials Technologies*, 2018, **3**, 1800111.

[40] J. Sun and Y. Li, *Journal*, 2023, **7**.

[41] H. Y. Zhou, X. N. Zhu, G. R. Ren and X. M. Chen, *J. Alloys Compd.*, 2016, **688**, 687-691.

[42] Z. Yao, Q. Luo, G. Zhang, H. Hao, M. Cao and H. Liu, *Journal of Materials Science: Materials in Electronics*, 2017, **28**, 11491-11499.

[43] L. Zhao, Q. Liu, J. Gao, S. Zhang and J.-F. Li, *Advanced Materials*, 2017, **29**, 1701824.

[44] Z. L. Wang, *Nano Today*, 2010, **5**, 540-552.

[45] K.-A. N. Duerloo, M. T. Ong and E. J. Reed, *The Journal of Physical Chemistry Letters*, 2012, **3**, 2871-2876.

[46] M. T. Ong, K.-A. N. Duerloo and E. J. Reed, *The Journal of Physical Chemistry C*, 2013, **117**, 3615-3620.

[47] B. Jaffe, R. S. Roth and S. Marzullo, *Journal of Applied Physics*, 1954, **25**, 809-810.

[48] Y. Saito, H. Takao, T. Tani, T. Nonoyama, K. Takatori, T. Homma, T. Nagaya and M. Nakamura, *Nature*, 2004, **432**, 84-87.

[49] P. Li, J. Zhai, B. Shen, S. Zhang, X. Li, F. Zhu and X. Zhang, *Advanced Materials*, 2018, **30**, 1705171.

[50] Y. Liu, Y. Chang, F. Li, B. Yang, Y. Sun, J. Wu, S. Zhang, R. Wang and W. Cao, *ACS Applied Materials & Interfaces*, 2017, **9**, 29863-29871.

[51] S. Chandratre and P. Sharma, *Applied Physics Letters*, 2012, **100**, 023114.

[52] M. T. Ong and E. J. Reed, *ACS Nano*, 2012, **6**, 1387-1394.

[53] M. Noor-A-Alam, H. J. Kim and Y.-H. Shin, *Physical Chemistry Chemical Physics*, 2014, **16**, 6575-6582.

[54] R. Fei, W. Li, J. Li and L. Yang, *Applied Physics Letters*, 2015, **107**, 173104.

[55] H. Yin, J. Gao, G.-P. Zheng, Y. Wang and Y. Ma, *The Journal of Physical Chemistry C*, 2017, **121**, 25576-25584.

[56] R. Gao and Y. Gao, physica status solidi (RRL) – Rapid Research Letters, 2017, **11**, 1600412.

[57] Y. Guo, S. Zhou, Y. Bai and J. Zhao, *Applied Physics Letters*, 2017, **110**, 163102.

[58] H.-J. Jia, H.-M. Mu, J.-P. Li, Y.-Z. Zhao, Y.-X. Wu and X.-C. Wang, *Physical Chemistry Chemical Physics*, 2018, **20**, 26288-26296.

[59] F. Xue, W. Hu, K.-C. Lee, L.-S. Lu, J. Zhang, H.-L. Tang, A. Han, W.-T. Hsu, S. Tu, W.-H. Chang, C.-H. Lien, J.-H. He, Z. Zhang, L.-J. Li and X. Zhang, *Advanced Functional Materials*, 2018, **28**, 1803738.

[60] H. Yin, G.-P. Zheng, Y. Wang and B. Yao, *Physical Chemistry Chemical Physics*, 2018, **20**, 19177-19187.

[61] K. Yasuda, X. Wang, K. Watanabe, T. Taniguchi and P. Jarillo-Herrero, *Science*, 2021, **372**, 1458-1462.

[62] M. Vizner Stern, Y. Waschitz, W. Cao, I. Nevo, K. Watanabe, T. Taniguchi, E. Sela, M. Urbakh, O. Hod and M. Ben Shalom, *Science*, 2021, **372**, 1462-1466.

[63] W. Zhang, A. Sun, X. Pan, Y. Han, X. Zhao, L. Yu, Z. Zuo and N. Suo, *Journal of Materials Science: Materials in Electronics*, 2019, **30**, 18729-18743.

[64] J. H. Van Vleck, *Rev. Mod. Phys.*, 1945, **17**, 27-47.

[65] W. Heisenberg, in *Original Scientific Papers Wissenschaftliche Originalarbeiten*, eds. W. Blum, H. Rechenberg and H.-P. Dürr, Springer Berlin Heidelberg, Berlin, Heidelberg, 1928, DOI: 10.1007/978-3-642-61659-4_35, pp. 580-597.

[66] L. Onsager, *Physical Review*, 1944, **65**, 117-149.

[67] N. D. Mermin and H. Wagner, *Physical Review Letters*, 1966, **17**, 1133-1136.

[68] S. Wei, X. Liao, C. Wang, J. Li, H. Zhang, Y.-J. Zeng, J. Linghu, H. Jin and Y. Wei, *2D Materials*, 2021, **8**, 012005.

[69] W.-B. Zhang, Q. Qu, P. Zhu and C.-H. Lam, *Journal of Materials Chemistry C*, 2015, **3**, 12457-12468.

[70] H. H. Kim, B. Yang, S. Li, S. Jiang, C. Jin, Z. Tao, G. Nichols, F. Sfigakis, S. Zhong, C. Li, S. Tian, D. G. Cory, G.-X. Miao, J. Shan, K. F. Mak, H. Lei, K. Sun, L.

Zhao and A. W. Tsen, *Proceedings of the National Academy of Sciences*, 2019, **116**, 11131-11136.

[71] Z. Zhang, J. Shang, C. Jiang, A. Rasmita, W. Gao and T. Yu, *Nano Letters*, 2019, **19**, 3138-3142.

[72] B. Huang, G. Clark, E. Navarro-Moratalla, D. R. Klein, R. Cheng, K. L. Seyler, D. Zhong, E. Schmidgall, M. A. McGuire, D. H. Cobden, W. Yao, D. Xiao, P. Jarillo-Herrero and X. Xu, *Nature*, 2017, **546**, 270-273.

[73] X. Li and J. Yang, *Journal of Materials Chemistry C*, 2014, **2**, 7071-7076.

[74] C. Gong, L. Li, Z. Li, H. Ji, A. Stern, Y. Xia, T. Cao, W. Bao, C. Wang, Y. Wang, Z. Q. Qiu, R. J. Cava, S. G. Louie, J. Xia and X. Zhang, *Nature*, 2017, **546**, 265-269.

[75] C. Xu, J. Feng, H. Xiang and L. Bellaiche, *npj Computational Materials*, 2018, **4**, 57.

[76] C. Tan, J. Lee, S.-G. Jung, T. Park, S. Albarakati, J. Partridge, M. R. Field, D. G. McCulloch, L. Wang and C. Lee, *Nature Communications*, 2018, **9**, 1554.

[77] H. L. Zhuang, P. R. C. Kent and R. G. Hennig, *Physical Review B*, 2016, **93**, 134407.

[78] Y. Deng, Y. Yu, Y. Song, J. Zhang, N. Z. Wang, Z. Sun, Y. Yi, Y. Z. Wu, S. Wu, J. Zhu, J. Wang, X. H. Chen and Y. Zhang, *Nature*, 2018, **563**, 94-99.

[79] Z. Fei, B. Huang, P. Malinowski, W. Wang, T. Song, J. Sanchez, W. Yao, D. Xiao, X. Zhu, A. F. May, W. Wu, D. H. Cobden, J.-H. Chu and X. Xu, *Nature Materials*, 2018, **17**, 778-782.

[80] P. A. Joy and S. Vasudevan, *Physical Review B*, 1992, **46**, 5425-5433.

[81] J.-U. Lee, S. Lee, J. H. Ryoo, S. Kang, T. Y. Kim, P. Kim, C.-H. Park, J.-G. Park and H. Cheong, *Nano Letters*, 2016, **16**, 7433-7438.

[82] X. Wang, K. Du, Y. Y. Fredrik Liu, P. Hu, J. Zhang, Q. Zhang, M. H. S. Owen, X. Lu, C. K. Gan, P. Sengupta, C. Kloc and Q. Xiong, *2D Materials*, 2016, **3**, 031009.

[83] Y. Ma, Y. Dai, M. Guo, C. Niu, Y. Zhu and B. Huang, *ACS Nano*, 2012, **6**, 1695-1701.

[84] H.-R. Fuh, B. Yan, S.-C. Wu, C. Felser and C.-R. Chang, *New Journal of Physics*, 2016, **18**, 113038.

[85] M. Bonilla, S. Kolekar, Y. Ma, H. C. Diaz, V. Kalappattil, R. Das, T. Eggers, H. R. Gutierrez, M.-H. Phan and M. Batzill, *Nature Nanotechnology*, 2018, **13**, 289-293.

[86] Y. L. Huang, W. Chen and A. T. S. Wee, *SmartMat*, 2021, **2**, 139-153.

[87] L. Seixas, A. S. Rodin, A. Carvalho and A. H. Castro Neto, *Physical Review Letters*, 2016, **116**, 206803.

[88] T. Cao, Z. Li and S. G. Louie, *Physical Review Letters*, 2015, **114**, 236602.

[89] C. Liu, B. Wang, G. Jia, P. Liu, H. Yin, S. Guan and Z. Cheng, *Applied Physics Letters*, 2021, **118**, 072902.

[90] N. Miao, B. Xu, N. C. Bristowe, J. Zhou and Z. Sun, *Journal of the American Chemical Society*, 2017, **139**, 11125-11131.

[91] Y. Wen, Z. Liu, Y. Zhang, C. Xia, B. Zhai, X. Zhang, G. Zhai, C. Shen, P. He, R. Cheng, L. Yin, Y. Yao, M. Getaye Sendeku, Z. Wang, X. Ye, C. Liu, C. Jiang, C. Shan, Y. Long and J. He, *Nano Letters*, 2020, **20**, 3130-3139.

[92] J.-J. Zhang, L. Lin, Y. Zhang, M. Wu, B. I. Yakobson and S. Dong, *Journal of the American Chemical Society*, 2018, **140**, 9768-9773.

[93] S.-H. Zhang and B.-G. Liu, *Journal of Materials Chemistry C*, 2018, **6**, 6792-6798.

[94] Y. Nie, M. Rahman, P. Liu, A. Sidike, Q. Xia and G.-h. Guo, *Physical Review B*, 2017, **96**, 075401.

[95] L. Zhang, Z. Yang, T. Gong, R. Pan, H. Wang, Z. Guo, H. Zhang and X. Fu, *Journal of Materials Chemistry A*, 2020, **8**, 8813-8830.

[96] R. Li, Y. Cheng and W. Huang, *Small*, 2018, **14**, 1802091.

[97] J. Zhou, Q. Wang, Q. Sun, X. S. Chen, Y. Kawazoe and P. Jena, *Nano Letters*, 2009, **9**, 3867-3870.

[98] R. Singh and G. Bester, *Physical Review B*, 2011, **84**, 155427.

[99] L. Zhang, J. Yu, M. Yang, Q. Xie, H. Peng and Z. Liu, *Nature Communications*, 2013, **4**, 1443.

[100] A.-Y. Lu, H. Zhu, J. Xiao, C.-P. Chuu, Y. Han, M.-H. Chiu, C.-C. Cheng, C.-W. Yang, K.-H. Wei, Y. Yang, Y. Wang, D. Sokaras, D. Nordlund, P. Yang, D. A. Muller, M.-Y. Chou, X. Zhang and L.-J. Li, *Nature Nanotechnology*, 2017, **12**, 744-749.

[101] Y. C. Cheng, Z. Y. Zhu, M. Tahir and U. Schwingenschlögl, *Europhys. Lett.*, 2013, **102**, 57001.

[102] L. Dong, J. Lou and V. B. Shenoy, *ACS Nano*, 2017, **11**, 8242-8248.

[103] Y. Bai, Q. Zhang, N. Xu, K. Deng and E. Kan, *Applied Surface Science*, 2019, **478**, 522-531.

[104] M. Born and K. Huang, *Am. J. Phys.*, 1955, **23**, 474-474.

[105] D. R. Hartree, Mathematical Proceedings of the Cambridge Philosophical Society, 2008, **24**, 89-110.

[106] V. Fock, *Z. Phys.*, 1930, **61**, 126-148.

[107] P. Hohenberg and W. Kohn, *Physical Review*, 1964, **136**, B864-B871.

[108] W. Kohn and L. J. Sham, *Physical Review*, 1965, **140**, A1133-A1138.

[109] W. Kohn, *Rev. Mod. Phys.*, 1999, **71**, 1253-1266.

[110] R. O. Jones and O. Gunnarsson, *Rev. Mod. Phys.*, 1989, **61**, 689-746.

[111] F. Herman, J. P. Van Dyke and I. B. Ortenburger, *Physical Review Letters*, 1969, **22**, 807-811.

[112] J. P. Perdew and K. Burke, *Int. J. Quantum Chem.*, 1996, **57**, 309-319.

[113] J. P. Perdew, K. Burke and M. Ernzerhof, *Physical Review Letters*, 1996, **77**, 3865-3868.

[114] S. Kohtani, J. Hiro, N. Yamamoto, A. Kudo, K. Tokumura and R. Nakagaki, *Catal. Commun.*, 2005, **6**, 185-189.

[115] P. M. W. Gill, B. G. Johnson, J. A. Pople and M. J. Frisch, *Chemical Physics Letters*, 1992, **197**, 499-505.

[116] A. V. Krukau, O. A. Vydrov, A. F. Izmaylov and G. E. Scuseria, *The Journal of Chemical Physics*, 2006, **125**, 224106.

[117] R. Hoffmann, *The Journal of Chemical Physics*, 1963, **39**, 1397-1412.

[118] G. Kresse and J. Furthmüller, *Physical Review B*, 1996, **54**, 11169-11186.

[119] G. Kresse and J. Furthmüller, *Computational Materials Science*, 1996, **6**, 15-50.

[120] Y. Wang, J. J. Wang, W. Y. Wang, Z. G. Mei, S. L. Shang, L. Q. Chen and Z. K. Liu, *J. Phys.: Condens. Matter*, 2010, **22**, 202201.

[121] M. Wu, H. Fu, L. Zhou, K. Yao and X. C. Zeng, *Nano Letters*, 2015, **15**, 3557-3562.

[122] C. Jin, F. Lin, K. Suenaga and S. Iijima, *Physical Review Letters*, 2009, **102**, 195505.

[123] L. Xu, J. Zeng, Q. Li, L. Xia, X. Luo, Z. Ma, B. Peng, S. X. Xiong, Z. Li, L.-L. Wang and Y. Lei, *Applied Surface Science*, 2021, **547**, 149207.

[124] D. Kong, H. Wang, J. J. Cha, M. Pasta, K. J. Koski, J. Yao and Y. Cui, *Nano Letters*, 2013, **13**, 1341-1347.

[125] J. Zeng, L. Xu, Y. Yang, X. Luo, H.-J. Li, S. X. Xiong and L.-L. Wang, *Physical Chemistry Chemical Physics*, 2021, **23**, 8318-8325.

[126] M. Jakhar, A. Kumar, P. K. Ahluwalia, K. Tankeshwar and R. Pandey, *Materials*, 2022, **15**.

[127] G. Z. S. Ling, S.-F. Ng and W.-J. Ong, *Advanced Functional Materials*, 2022, **n/a**, 2111875.

[128] Y. Wu, W. Sun, S. Liu, B. Wang, C. Liu, H. Yin and Z. Cheng, *Nanoscale*, 2021, **13**, 16564-16570.

[129] Z. Wu, W. Jie, Z. Yang and J. Hao, *Materials Today Nano*, 2020, **12**, 100092.

[130] K. Qian, R. Y. Tay, V. C. Nguyen, J. Wang, G. Cai, T. Chen, E. H. T. Teo and P. S. Lee, *Advanced Functional Materials*, 2016, **26**, 2176-2184.

[131] C.-w. Zhang, *Journal of Applied Physics*, 2012, **111**, 043702.

[132] Z. Galazka, *Semiconductor Science and Technology*, 2018, **33**, 113001.

[133] K. Iordanidou, M. Houssa, J. Kioseoglou, V. V. Afanas'ev, A. Stesmans and C. Persson, *ACS Applied Nano Materials*, 2018, **1**, 6656-6665.

[134] F. Li, X. Zhou, W. Feng, B. Fu and Y. Yao, *New Journal of Physics*, 2018, **20**, 043048.

[135] M. Houssa, K. Iordanidou, G. Pourtois, V. V. Afanas'ev and A. Stesmans, *AIP Advances*, 2018, **8**, 055010.

[136] Y. Wang, Q. Zhang, Q. Shen, Y. Cheng, U. Schwingenschlögl and W. Huang, *Journal of Materials Chemistry C*, 2017, **5**, 4520-4525.

[137] C.-W. Wu and D.-X. Yao, *Journal of Magnetism and Magnetic Materials*, 2019, **478**, 68-76.

[138] S. Jiang, H. Yin, J. Li, L. Liu, X. Shi, Y. Yan, C. Liu, G.-P. Zheng and P.-F. Liu, *physica status solidi (RRL) – Rapid Research Letters*, 2020, **14**, 2000321.

[139] M. N. Blonsky, H. L. Zhuang, A. K. Singh and R. G. Hennig, *ACS Nano*, 2015, **9**, 9885-9891.

[140] X. Shi, H. Yin, S. Jiang, W. Chen, G.-P. Zheng, F. Ren, B. Wang, G. Zhao and B. Liu, *Physical Chemistry Chemical Physics*, 2021, **23**, 3637-3645.

[141] S.-D. Guo, X.-S. Guo, Z.-Y. Liu and Y.-N. Quan, *Journal of Applied Physics*, 2020, **127**, 064302.

[142] H. J. Monkhorst and J. D. Pack, *Physical Review B*, 1976, **13**, 5188-5192.

[143] J. Heyd, G. E. Scuseria and M. Ernzerhof, *The Journal of Chemical Physics*, 2003, **118**, 8207-8215.

[144] A. Togo and I. Tanaka, *Scripta Materialia*, 2015, **108**, 1-5.

[145] G. J. Martyna, M. L. Klein and M. Tuckerman, *The Journal of Chemical Physics*, 1992, **97**, 2635-2643.

[146] X. Wu, D. Vanderbilt and D. R. Hamann, *Physical Review B*, 2005, **72**, 035105.

[147] S. Grimme, J. Antony, S. Ehrlich and H. Krieg, *The Journal of Chemical Physics*, 2010, **132**, 154104.

[148] A. H. A.-M. H. C. R. Hebd, *Seances Acad. Sci.* , 1963, **256**, 3477.

[149] B. Siegel, *Inorganica Chimica Acta Reviews*, 1968, **2**, 137-146.

[150] S. M. Whittingha, *Intercalation chemistry*, Elsevier, 2012.

[151] F. M. Brewer, P. L. Goggin and G. S. Reddy, *Journal of Inorganic and Nuclear Chemistry*, 1966, **28**, 361-364.

[152] W. Zhou, S. Guo, S. Zhang, Z. Zhu, X. Song, T. Niu, K. Zhang, X. Liu, Y. Zou and H. Zeng, *Nanoscale*, 2018, **10**, 3350-3355.

[153] I. Vurgaftman and J. R. Meyer, *Journal of Applied Physics*, 2003, **94**, 3675-3696.

[154] J. He, P. Lyu and P. Nachtigall, *Catalysis Today*, 2020, **340**, 178-182.

[155] S. Jiang, J. Li, W. Chen, H. Yin, G.-P. Zheng and Y. Wang, *Nanoscale*, 2020, **12**, 5888-5897.

[156] M. Li, Y. Dai, W. Wei and B. Huang, *Physical Chemistry Chemical Physics*, 2018, **20**, 9221-9227.

[157] H. Lang, S. Zhang and Z. Liu, *Physical Review B*, 2016, **94**, 235306.

[158] S. Bruzzone and G. Fiori, *Applied Physics Letters*, 2011, **99**, 222108.

[159] B. Radisavljevic, A. Radenovic, J. Brivio, V. Giacometti and A. Kis, *Nature Nanotechnology*, 2011, **6**, 147-150.

[160] Y. Le Page and P. Saxe, *Physical Review B*, 2001, **63**, 174103.

[161] S. Zhao, Z. Li and J. Yang, *Journal of the American Chemical Society*, 2014, **136**, 13313-13318.

[162] C. Lee, X. Wei, W. Kysar Jeffrey and J. Hone, *Science*, 2008, **321**, 385-388.

[163] S. Bertolazzi, J. Brivio and A. Kis, *ACS Nano*, 2011, **5**, 9703-9709.

[164] H. Şahin, S. Cahangirov, M. Topsakal, E. Bekaroglu, E. Akturk, R. T. Senger and S. Ciraci, *Physical Review B*, 2009, **80**, 155453.

[165] V. Litvinenko, Geomechanics and Geodynamics of Rock Masses: Proceedings of the 2018 European Rock Mechanics Symposium (1st ed.). CRC Press. , 2018.

[166] H. Sun, S. Mukherjee and C. V. Singh, *Physical Chemistry Chemical Physics*, 2016, **18**, 26736-26742.

[167] I. Kaplan-Ashiri, S. R. Cohen, K. Gartsman, R. Rosentsveig, V. Ivanovskaya, T. Heine, G. Seifert, H. D. Wagner and R. Tenne, *Materials Science Forum*, 2005, **475-479**, 4097-4102.

[168] R. Meng, M. Houssa, K. Iordanidou, G. Pourtois, V. Afanasiev and A. Stesmans, *Journal of Applied Physics*, 2020, **128**, 034304.

[169] C. Hua, F. Sheng, Q. Hu, Z.-A. Xu, Y. Lu and Y. Zheng, *The Journal of Physical Chemistry Letters*, 2018, **9**, 6695-6701.

[170] Y. Wang and Y. Ding, *Journal of Materials Chemistry C*, 2018, **6**, 2245-2251.

[171] H. Xiang, B. Xu, Y. Xia, J. Yin and Z. Liu, *Scientific Reports*, 2016, **6**, 39218.

[172] I. A. Verzhbitskiy, H. Kurebayashi, H. Cheng, J. Zhou, S. Khan, Y. P. Feng and G. Eda, *Nature Electronics*, 2020, **3**, 460-465.

[173] J. He, Y. Chen, Z. Wang, M. Yang, T. Yang, L. Shen, X. Xu, Y. Jiang, J. Chai, L. M. Wong, S. Wang, Y. P. Feng and J. Zhou, *Journal of Materials Chemistry C*, 2022, DOI: 10.1039/D2TC00564F.

[174] E. C. Stoner and R. Whiddington, Proceedings of the Royal Society of London. Series A - Mathematical and Physical Sciences, 1936, **154**, 656-678.

[175] O. V. Yazyev and L. Helm, *Physical Review B*, 2007, **75**, 125408.

[176] H. Peng, H. J. Xiang, S.-H. Wei, S.-S. Li, J.-B. Xia and J. Li, *Physical Review Letters*, 2009, **102**, 017201.

[177] G. Stollhoff, A. M. Oleś and V. Heine, *Physical Review B*, 1990, **41**, 7028-7041.

[178] N. D. Mermin, *Physical Review*, 1965, **137**, A1441-A1443.

[179] B. Fu, W. Feng, X. Zhou and Y. Yao, *2D Materials*, 2017, **4**, 025107.

[180] K. Zhao, Y. Guo, Y. Shen, Q. Wang, Y. Kawazoe and P. Jena, *The Journal of Physical Chemistry Letters*, 2020, **11**, 3501-3506.

[181] W. Sun, Y. Shen, Y. Guo, Y. Chen and Q. Wang, *Applied Surface Science*, 2021, **554**, 149499.

[182] M. J. Varjovi, M. E. Kilic and E. Durgun, *Physical Review Materials*, 2022, **6**, 034004.

[183] P. Khanchaitit, K. Han, M. R. Gadinski, Q. Li and Q. Wang, *Nature Communications*, 2013, **4**, 2845.

[184] Q. Li, F. Liu, T. Yang, M. R. Gadinski, G. Zhang, L.-Q. Chen and Q. Wang, *Proceedings of the National Academy of Sciences*, 2016, **113**, 9995-10000.

[185] K. Yao, S. Chen, M. Rahimabady, M. S. Mirshekarloo, S. Yu, F. E. H. Tay, T. Sritharan and L. Lu, *IEEE Transactions on Ultrasonics, Ferroelectrics, and Frequency Control*, 2011, **58**, 1968-1974.

[186] L. Wu, X. Wang and L. Li, *RSC Advances*, 2016, **6**, 14273-14282.

[187] Z. Shen, X. Wang, B. Luo and L. Li, *Journal of Materials Chemistry A*, 2015, **3**, 18146-18153.

[188] Q. Yuan, F. Yao, Y. Wang, R. Ma and H. Wang, *Journal of Materials Chemistry C*, 2017, **5**, 9552-9558.

[189] Y. Li, N. Sun, X. Li, J. Du, L. Chen, H. Gao, X. Hao and M. Cao, *Acta Mater.*, 2018, **146**, 202-210.

[190] D. k. Kwon and M. H. Lee, IEEE Transactions on Ultrasonics, Ferroelectrics, and Frequency Control, 2012, **59**, 1894-1899.

[191] N. Ortega, A. Kumar, J. F. Scott, D. B. Chrisey, M. Tomazawa, S. Kumari, D. G. B. Diestra and R. S. Katiyar, *J. Phys.: Condens. Matter*, 2012, **24**, 445901.

[192] J. Kim, S. Saremi, M. Acharya, G. Velarde, E. Parsonnet, P. Donahue, A. Qualls, D. Garcia and L. W. Martin, *Science*, 2020, **369**, 81-84.

[193] Z. Chafi and A. Souici, *Mater. Sci. Semicond. Process.*, 2021, **123**, 105564.

[194] T. Das and S. Datta, *Nanoscale Advances*, 2020, **2**, 1090-1104.

[195] A. Laturia, M. L. Van de Put and W. G. Vandenberghe, *npj 2D Materials and Applications*, 2018, **2**, 6.

[196] J. McPherson, J. Kim, A. Shanware, H. Mogul and J. Rodriguez, 2002.

[197] S. Jiang, H. Yin and G.-P. Zheng, *Nanoscale*, 2022, **14**, 11369-11377.

[198] G. Kresse and D. Joubert, *Physical Review B*, 1999, **59**, 1758-1775.

[199] P. E. Blöchl, *Physical Review B*, 1994, **50**, 17953-17979.

[200] Z. Zhang, X. Liu, B. I. Yakobson and W. Guo, *Journal of the American Chemical Society*, 2012, **134**, 19326-19329.

[201] S. Cahangirov, M. Topsakal, E. Aktürk, H. Şahin and S. Ciraci, *Physical Review Letters*, 2009, **102**, 236804.

[202] V. V. Kulish and W. Huang, *Journal of Materials Chemistry C*, 2017, **5**, 8734-8741.

[203] W. Yu, C.-Y. Niu, Z. Zhu, X. Wang and W.-B. Zhang, *Journal of Materials Chemistry C*, 2016, **4**, 6581-6587.

[204] H. Zheng, X.-B. Li, N.-K. Chen, S.-Y. Xie, W. Q. Tian, Y. Chen, H. Xia, S. B. Zhang and H.-B. Sun, *Physical Review B*, 2015, **92**, 115307.

[205] Y. Yan, W. Xiong, S. Li, K. Zhao, X. Wang, J. Su, X. Song, X. Li, S. Zhang, H. Yang, X. Liu, L. Jiang, T. Zhai, C. Xia, J. Li and Z. Wei, *Advanced Optical Materials*, 2019, **7**, 1900622.

[206] Y. Liao, Z. Zhang, Z. Gao, Q. Qian and M. Hua, *ACS Applied Materials & Interfaces*, 2020, **12**, 30659-30669.

[207] R. C. Andrew, R. E. Mapasha, A. M. Ukpong and N. Chetty, *Physical Review B*, 2012, **85**, 125428.

[208] E. Cadelano, P. L. Palla, S. Giordano and L. Colombo, *Physical Review B*, 2010, **82**, 235414.

[209] A. Castellanos-Gomez, M. Poot, G. A. Steele, H. S. J. van der Zant, N. Agraït and G. Rubio-Bollinger, *Advanced Materials*, 2012, **24**, 772-775.

[210] T. Su, C. H. Lee, S.-D. Guo, G. Wang, W.-L. Ong, L. Cao, W. Zhao, S. A. Yang and Y. S. Ang, *Materials Today Physics*, 2023, **31**, 101001.

[211] X. Li, J. Qiu, X. Chen, F. Zhang, Z. Chen and J. Yu, *Mater. Lett.*, 2022, **325**, 132867.

[212] P. Wang, H. Liu, Y. Zong, H. Wen, J.-B. Xia and H.-B. Wu, *ACS Applied Materials & Interfaces*, 2021, **13**, 34178-34187.

[213] S. A. Wolf, D. D. Awschalom, R. A. Buhrman, J. M. Daughton, S. von Molnár, M. L. Roukes, A. Y. Chtchelkanova and D. M. Treger, *Science*, 2001, **294**, 1488-1495.

[214] L. Webster and J.-A. Yan, *Physical Review B*, 2018, **98**, 144411.

[215] C. Ataca, H. Şahin and S. Ciraci, *The Journal of Physical Chemistry C*, 2012, **116**, 8983-8999.

[216] C. Si, J. Zhou and Z. Sun, *ACS Applied Materials & Interfaces*, 2015, **7**, 17510-17515.

[217] J. He, P. Lyu, L. Z. Sun, Á. Morales García and P. Nachtigall, *Journal of Materials Chemistry C*, 2016, **4**, 6500-6509.

[218] H. L. Zhuang, Y. Xie, P. R. C. Kent and P. Ganesh, *Physical Review B*, 2015, **92**, 035407.

[219] B. Wang, Q. Wu, Y. Zhang, Y. Guo, X. Zhang, Q. Zhou, S. Dong and J. Wang, *Nanoscale Horizons*, 2018, **3**, 551-555.

[220] B. Wang, X. Zhang, Y. Zhang, S. Yuan, Y. Guo, S. Dong and J. Wang, *Materials Horizons*, 2020, **7**, 1623-1630.

[221] Y. Guo, Y. Zhang, S. Yuan, B. Wang and J. Wang, *Nanoscale*, 2018, **10**, 18036-18042.

[222] C. Wang, X. Zhou, L. Zhou, N.-H. Tong, Z.-Y. Lu and W. Ji, *Science Bulletin*, 2019, **64**, 293-300.

[223] X. Cai, T. Song, N. P. Wilson, G. Clark, M. He, X. Zhang, T. Taniguchi, K. Watanabe, W. Yao, D. Xiao, M. A. McGuire, D. H. Cobden and X. Xu, *Nano Letters*, 2019, **19**, 3993-3998.

[224] H. H. Kim, B. Yang, S. Li, S. Jiang, C. Jin, Z. Tao, G. Nichols, F. Sfigakis, S. Zhong, C. Li, S. Tian, D. G. Cory, G.-X. Miao, J. Shan, K. F. Mak, H. Lei, K. Sun, L. Zhao and A. W. Tsen, *Proceedings of the National Academy of Sciences*, 2019, **116**, 11131.

[225] R. Shidpour and M. Manteghian, *Nanoscale*, 2010, **2**, 1429-1435.

[226] Y. C. Cheng, Z. Y. Zhu, W. B. Mi, Z. B. Guo and U. Schwingenschlögl, *Physical Review B*, 2013, **87**, 100401.

[227] R. Xu, B. Liu, X. Zou and H.-M. Cheng, *ACS Applied Materials & Interfaces*, 2017, **9**, 38796-38801.

[228] H. Kumar, N. C. Frey, L. Dong, B. Anasori, Y. Gogotsi and V. B. Shenoy, *ACS Nano*, 2017, **11**, 7648-7655.

[229] S. Gong, W. Wan, S. Guan, B. Tai, C. Liu, B. Fu, S. A. Yang and Y. Yao, *Journal of Materials Chemistry C*, 2017, **5**, 8424-8430.

[230] S. Demirci, N. Avazlı, E. Durgun and S. Cahangirov, *Physical Review B*, 2017, **95**, 115409.

[231] L. Guan and J. Tao, *Physical Review Applied*, 2017, **8**, 064019.

[232] J. Zhang, S. Jia, I. Kholmanov, L. Dong, D. Er, W. Chen, H. Guo, Z. Jin, V. B. Shenoy, L. Shi and J. Lou, *ACS Nano*, 2017, **11**, 8192-8198.

[233] D. Wu, Z. Zhuo, H. Lv and X. Wu, *The Journal of Physical Chemistry Letters*, 2021, **12**, 2905-2911.

[234] S.-S. Guan, S.-S. Ke, F.-F. Yu, H.-X. Deng, Y. Guo and H.-F. Lü, *Applied Surface Science*, 2019, **496**, 143692.

[235] M.-Y. Liu, L. Gong, Y. He and C. Cao, *Physical Review B*, 2021, **104**, 035409.

[236] W. Chen, X. Hou, X. Shi and H. Pan, *ACS Applied Materials & Interfaces*, 2018, **10**, 35289-35295.

[237] G. Kresse and J. Hafner, *Physical Review B*, 1993, **47**, 558-561.

[238] G. Kresse and J. Hafner, *Physical Review B*, 1994, **49**, 14251-14269.

[239] J. P. Perdew, K. Burke and M. Ernzerhof, *Physical Review Letters*, 1997, **78**, 1396-1396.

[240] S. L. Dudarev, G. A. Botton, S. Y. Savrasov, C. J. Humphreys and A. P. Sutton, *Physical Review B*, 1998, **57**, 1505-1509.

[241] I. Solovyev, N. Hamada and K. Terakura, *Physical Review B*, 1996, **53**, 7158-7170.

[242] B. J. Morgan and G. W. Watson, *Surf Sci.*, 2007, **601**, 5034-5041.

[243] Y. Yamazaki, K. Mori, Y. Kuwahara, H. Kobayashi and H. Yamashita, *ACS Applied Materials & Interfaces*, 2021, **13**, 48669-48678.

[244] B. J. Morgan and G. W. Watson, *The Journal of Physical Chemistry C*, 2009, **113**, 7322-7328.

[245] K. Dartigeas, L. Benoist, D. Gonbeau, G. Pfister-Guillouzo, G. Ouvrard and A. Levasseur, *J. Electron. Spectrosc. Relat. Phenom.*, 1997, **83**, 45-58.

[246] W. G. Stirling, B. Dorner, J. D. N. Cheeke and J. Revelli, *Solid State Commun.*, 1976, **18**, 931-933.

[247] Y.-W. Son, M. L. Cohen and S. G. Louie, *Nature*, 2006, **444**, 347-349.

[248] E. V. Castro, N. M. R. Peres, T. Stauber and N. A. P. Silva, *Physical Review Letters*, 2008, **100**, 186803.

[249] C. Liu, S. Guan, H. Yin, W. Wan, Y. Wang and Y. Zhang, *Applied Physics Letters*, 2019, **115**, 252904.

[250] E. C. Stoner, Proceedings of the Royal Society of London. Series A. Mathematical and Physical Sciences, 1939, **169**, 339-371.

[251] P. Liu, G. Zhang, Y. Yan, G. Jia, C. Liu, B. Wang and H. Yin, *Applied Physics Letters*, 2021, **119**, 102403.

[252] T. Liu, X. Zhang, M. Xia, H. Yu, N. Peng, C. Jiang, M. Shui, Y. Xie, T.-F. Yi and J. Shu, *Nano Energy*, 2020, **67**, 104295.

[253] J. Qiao, X. Kong, Z.-X. Hu, F. Yang and W. Ji, *Nature Communications*, 2014, **5**, 4475.

[254] N. Lu, Z. Zhuo, Y. Wang, H. Guo, W. Fa, X. Wu and X. C. Zeng, *The Journal of Physical Chemistry Letters*, 2018, **9**, 6568-6575.

[255] R. Peng, Y. Ma, S. Zhang, B. Huang, L. Kou and Y. Dai, *Materials Horizons*, 2020, **7**, 504-510.

[256] Z. Lei, J. M. Lee, G. Singh, C. I. Sathish, X. Chu, A. a. H. Al-Muhtaseb, A. Vinu and J. Yi, *Energy Storage Materials*, 2021, **36**, 514-550.

[257] I. Galanakis, P. Mavropoulos and P. H. Dederichs, *Journal of Physics D: Applied Physics*, 2006, **39**, 765-775.

[258] J. H. Park, E. Vescovo, H. J. Kim, C. Kwon, R. Ramesh and T. Venkatesan, *Nature*, 1998, **392**, 794-796.

[259] M. Ziese, *Rep. Prog. Phys.*, 2002, **65**, 143-249.

[260] Y. Tong, Y. Guo, K. Mu, H. Shan, J. Dai, Y. Liu, Z. Sun, A. Zhao, X. C. Zeng, C. Wu and Y. Xie, *Advanced Materials*, 2017, **29**, 1703123.

[261] L. Song, L. Zhang, Y. Guan, H. Zhao, X. Xu, J. Lu, C. Yan and J. Cai, *Materials Research Express*, 2019, **6**, 075911.

[262] B. Özdamar, G. Özbal, M. N. Çınar, K. Sevim, G. Kurt, B. Kaya and H. Sevinçli, *Physical Review B*, 2018, **98**, 045431.

[263] F. Mouhat and F.-X. Coudert, *Physical Review B*, 2014, **90**, 224104.

[264] L.-C. Zhang, G. Qin, W.-Z. Fang, H.-J. Cui, Q.-R. Zheng, Q.-B. Yan and G. Su, *Scientific Reports*, 2016, **6**, 19830.

[265] W. Li and J. Li, *Nano Research*, 2015, **8**, 3796-3802.

[266] J. F. Nye, Physical Properties of Crystals: Their Representation by *Tensors and Matrices*, Oxford University Press: New York, 1985.

[267] S.-D. Guo, X.-S. Guo, X.-X. Cai, W.-Q. Mu and W.-C. Ren, *Journal of Applied Physics*, 2021, **129**, 214301.

[268] J. W. Yeh, S. K. Chen, S. J. Lin, J. Y. Gan, T. S. Chin, T. T. Shun, C. H. Tsau and S. Y. Chang, *Adv. Eng. Mater.*, 2004, **6**, 299-303.

[269] Y. Yao, Z. Huang, P. Xie, S. D. Lacey, R. J. Jacob, H. Xie, F. Chen, A. Nie, T. Pu, M. Rehwoldt, D. Yu, M. R. Zachariah, C. Wang, R. Shahbazian-Yassar, J. Li and L. Hu, *Science*, 2018, **359**, 1489-1494.

[270] P. Koželj, S. Vrtnik, A. Jelen, S. Jazbec, Z. Jagličić, S. Maiti, M. Feuerbacher, W. Steurer and J. Dolinšek, *Physical Review Letters*, 2014, **113**, 107001.

[271] Y.-F. Kao, S.-K. Chen, J.-H. Sheu, J.-T. Lin, W.-E. Lin, J.-W. Yeh, S.-J. Lin, T.-H. Liou and C.-W. Wang, *Int. J. Hydrogen Energy*, 2010, **35**, 9046-9059.

[272] Y. Jien-Wei, *Ann. Chim. Sci. Mat*, 2006, **31**, 633-648.

[273] G. Anand, A. P. Wynn, C. M. Handley and C. L. Freeman, *Acta Mater.*, 2018, **146**, 119-125.

[274] T. J. Harrington, J. Gild, P. Sarker, C. Toher, C. M. Rost, O. F. Dippo, C. McElfresh, K. Kaufmann, E. Marin, L. Borowski, P. E. Hopkins, J. Luo, S. Curtarolo, D. W. Brenner and K. S. Vecchio, *Acta Mater.*, 2019, **166**, 271-280.

[275] Y. Zhang, W.-M. Guo, Z.-B. Jiang, Q.-Q. Zhu, S.-K. Sun, Y. You, K. Plucknett and H.-T. Lin, *Scripta Materialia*, 2019, **164**, 135-139.

[276] J. Gild, J. Braun, K. Kaufmann, E. Marin, T. Harrington, P. Hopkins, K. Vecchio and J. Luo, *Journal of Materiomics*, 2019, **5**, 337-343.

[277] T. Jin, X. Sang, R. R. Unocic, R. T. Kinch, X. Liu, J. Hu, H. Liu and S. Dai, *Advanced Materials*, 2018, **30**, 1707512.

[278] X. Yan, L. Constantin, Y. Lu, J.-F. Silvain, M. Nastasi and B. Cui, *Journal of the American Ceramic Society*, 2018, **101**, 4486-4491.

[279] D. Bérardan, S. Franger, D. Dragoe, A. K. Meena and N. Dragoe, *physica status solidi (RRL) – Rapid Research Letters*, 2016, **10**, 328-333.

[280] C. Zhao, F. Ding, Y. Lu, L. Chen and Y.-S. Hu, *Angewandte Chemie International Edition*, 2020, **59**, 264-269.

[281] J. Cavin, A. Ahmadiparidari, L. Majidi, A. S. Thind, S. N. Misal, A. Prajapati, Z. Hemmat, S. Rastegar, A. Beukelman, M. R. Singh, K. A. Unocic, A. Salehi-Khojin and R. Mishra, *Advanced Materials*, 2021, **33**, 2100347.

[282] Q. H. Wang, K. Kalantar-Zadeh, A. Kis, J. N. Coleman and M. S. Strano, *Nature Nanotechnology*, 2012, **7**, 699-712.

[283] S. Z. Butler, S. M. Hollen, L. Cao, Y. Cui, J. A. Gupta, H. R. Gutiérrez, T. F. Heinz, S. S. Hong, J. Huang, A. F. Ismach, E. Johnston-Halperin, M. Kuno, V. V. Plashnitsa, R. D. Robinson, R. S. Ruoff, S. Salahuddin, J. Shan, L. Shi, M. G. Spencer, M. Terrones, W. Windl and J. E. Goldberger, *ACS Nano*, 2013, **7**, 2898-2926.

[284] H. J. Conley, B. Wang, J. I. Ziegler, R. F. Haglund, Jr., S. T. Pantelides and K. I. Bolotin, *Nano Letters*, 2013, **13**, 3626-3630.

[285] A. A. Tedstone, D. J. Lewis and P. O'Brien, *Chemistry of Materials*, 2016, **28**, 1965-1974.

[286] J. Qu, A. Elgendy, R. Cai, M. A. Buckingham, A. A. Papaderakis, H. de Latour, K. Hazeldine, G. F. S. Whitehead, F. Alam, C. T. Smith, D. J. Binks, A. Walton, J. M.

Skelton, R. A. W. Dryfe, S. J. Haigh and D. J. Lewis, *Advanced Science*, 2023, **10**, 2204488.

[287] T. X. Nguyen, Y.-H. Su, C.-C. Lin and J.-M. Ting, *Advanced Functional Materials*, 2021, **31**, 2106229.

[288] L. Lin, K. Wang, A. Sarkar, C. Njel, G. Karkera, Q. Wang, R. Azmi, M. Fichtner, H. Hahn, S. Schweidler and B. Breitung, *Advanced Energy Materials*, 2022, **12**, 2103090.

[289] H. Fu, Y. Jiang, M. Zhang, Z. Zhong, Z. Liang, S. Wang, Y. Du and C. Yan, *Chemical Society Reviews*, 2024, **53**, 2211-2247.

[290] A. van de Walle, P. Tiwary, M. de Jong, D. L. Olmsted, M. Asta, A. Dick, D. Shin, Y. Wang, L. Q. Chen and Z. K. Liu, *Calphad*, 2013, **42**, 13-18.

[291] A. van de Walle, *Calphad*, 2009, **33**, 266-278.

[292] S.-Y. Liu, S. Zhang, S. Liu, D.-J. Li, Y. Li and S. Wang, *J. Eur. Ceram. Soc.*, 2021, **41**, 6267-6274.

[293] S.-Y. Liu, C. Liu, S. Zhang, S. Liu, D.-J. Li, Y. Li and S. Wang, *Journal of Applied Physics*, 2022, **131**, 075105.

[294] A. Deshpande, C. Ratsch, C. V. Ciobanu and S. Kodambaka, *Journal of Applied Physics*, 2022, **131**, 234302.

[295] S.-C. Dai, Z.-C. Xie and Y.-J. Wang, *Int. J. Plast.*, 2022, **149**, 103155.

[296] S. Manna, G. L. Brennecka, V. Stevanović and C. V. Ciobanu, *Journal of Applied Physics*, 2017, **122**, 105101.

[297] B. P. Burton, A. van de Walle and U. Kattner, *Journal of Applied Physics*, 2006, **100**, 113528.

[298] Z. Hemmat, J. Cavin, A. Ahmadiparidari, A. Ruckel, S. Rastegar, S. N. Misal, L. Majidi, K. Kumar, S. Wang, J. Guo, R. Dawood, F. Lagunas, P. Parajuli, A. T. Ngo, L.

A. Curtiss, S. B. Cho, J. Cabana, R. F. Klie, R. Mishra and A. Salehi-Khojin, *Advanced Materials*, 2020, **32**, 1907041.

[299] H. Zaid, K. Tanaka, M. Liao, M. S. Goorsky, S. Kodambaka and H. Kindlund, *Nano Letters*, 2021, **21**, 577-582.

[300] T. Ying, T. Yu, Y.-S. Shiah, C. Li, J. Li, Y. Qi and H. Hosono, *Journal of the American Chemical Society*, 2021, **143**, 7042-7049.

[301] K. Tanaka, H. Zaid, T. Aoki, A. Deshpande, K. Hojo, C. V. Ciobanu and S. Kodambaka, *Nano Letters*, 2024, **24**, 493-500.

[302] S. Saha, T. P. Sinha and A. Mookerjee, *Phys. Rev. B*, 2000, **62**, 8828-8834.

[303] H. Yuan, Z. Li and J. Yang, *Journal of Materials Chemistry C*, 2018, **6**, 9055-9059.

[304] C. Lee, X. Wei, J. W. Kysar and J. Hone, *Science*, 2008, **321**, 385-388.